Title
Estimating the spatial and temporal distribution of snow in mountainous terrain

Author
Musselman, Keith Newton

Publication Date
2012

Peer reviewed|Thesis/dissertation

UNIVERSITY OF CALIFORNIA

Los Angeles

Estimating the spatial and temporal distribution of snow in mountainous terrain

A dissertation submitted in partial satisfaction of the requirements for the degree of

Doctor of Philosophy in Civil Engineering

By

Keith Newton Musselman

2012

ABSTRACT OF THE DISSERTATION

Estimating the spatial and temporal distribution of
snow in mountainous terrain

by

Keith Newton Musselman

Doctor of Philosophy in Civil Engineering

University of California, Los Angeles, 2012

Professor Steven Adam Margulis, co-Chair

Professor Noah P. Molotch, co-Chair

In-situ measurements and numerical models were used to quantify and improve understanding of the processes governing snowpack dynamics in mountainous terrain. Three studies were conducted in Sequoia National Park in the southern Sierra Nevada, California. The first two studies evaluated and simulated the variability of observed melt rates at the point-scale in a mixed conifer forest. The third study evaluated the accuracy of a distributed snow model run over 1800 km^2; a 3600 m elevation gradient that includes ecosystems ranging from semi-arid grasslands to massive sequoia stands to alpine tundra. In the first study, a network of 24 automated snow depth sensors and repeated monthly snow density surveys in a conifer forest were used to measure snow ablation rates for three years. A model was developed to estimate the direct beam solar radiation beneath the forest canopy from upward-looking hemispherical photos and above-canopy measurements. Sub-canopy solar beam irradiance and the bulk canopy metric

sky view factor explained the most (58% and 87%, respectively) of the observed ablation rates in years with the least and most cloud cover, respectively; no single metric could explain > 41% of the melt rate variability for all years. In the second study, the time-varying photo-derived direct beam canopy transmissivity and the sky view factor canopy parameter were incorporated into a one-dimensional physically based snowmelt model. Compared to a bulk parameterization of canopy radiative transfer, when the model was modified to accept the time-varying canopy transmissivity, errors in the simulated snow disappearance date were reduced by one week and errors in the timing of soil water fluxes were reduced by 11 days, on average. In the third study, a distributed land surface model was used to simulate snow depth and SWE dynamics for three years. The model was evaluated against data from regional automated SWE measurement stations, repeated catchment-scale depth and density surveys, and airborne LiDAR snow depth data. In general, the model accurately simulated the seasonal maximum snow depth and SWE at lower and middle elevation forested areas. The model tended to overestimate SWE at upper elevations where no precipitation measurements were available. The SWE errors could largely be explained ($R^2 > 0.80$, $p<0.01$) by distance of the SWE measurement from the nearest precipitation gauge. The results suggest that precipitation uncertainty is a critical limitation on snow model accuracy. Finally, an analysis of seasonal and inter-annual snowmelt patterns highlighted distinct melt differences between lower, middle, and upper elevations. Snowmelt was generally most frequent (70% - 95% of the snow-covered season) at the lower elevations where snow cover was ephemeral and seasonal mean melt rates computed on days when melt was simulated were generally low (< 3 mm day^{-1}). At upper elevations, melt occurred during less than 65% of the snow-covered period, it occurred later in the season, and mean melt rates were

the highest of the region (> 6 mm day^{-1}). Middle elevations remained continuously snow covered throughout the winter and early spring, were prone to frequent but intermittent melt, and provided the most sustained period of seasonal mean snowmelt (~ 5 mm day^{-1}). The melt dynamics (e.g. timing and melt rate) unique to these middle elevations may be critical to the local forest ecosystem. Furthermore, the three years evaluated in this study indicate a marked sensitivity of this elevation range to seasonal meteorology, suggesting that it could be highly sensitive to future changes in climate.

The dissertation of Keith Newton Musselman is approved.

William W. Yeh

Terri S. Hogue

Alexander Dean Hall

Noah P. Molotch, Committee co-Chair

Steven Adam Margulis, Committee co-Chair

University of California, Los Angeles

2012

DEDICATION

This thesis is dedicated to my parents who taught me to work hard, set lofty goals and who instilled in me an interest in science, nature and adventure.

"… except in the case of some rarely gifted nature
there will never be a good man who has not
from his childhood been used to play amid
things of beauty and make of them a joy and a study."

- PLATO, *Republic*, Jowett translation

And to my wonderful fiancée whose unfaltering support and willingness to 'give Los Angeles a chance' made this dissertation possible.

TABLE OF CONTENTS

LIST OF FIGURES

LIST OF TABLES

ACKNOWLEDGMENTS

I thank my co-advisors Steve Margulis and Noah Molotch for their instruction and guidance while at UCLA. It was an honor and a pleasure to learn from them. I owe gratitude to my committee members Professors Terri Hogue, Alex Hall, and William Yeh. Bart Forman provided great inspiration, friendship and conversation. Ernesto Trujillo kept me awake with strong coffee, deepened my respect for mathematics, and motivated me to unplug on occasional weekends. The Margulis and Hogue research groups at UCLA provided great support both academically and socially. Those who sacrificed personal days in sunny California to conduct snow surveys in Sequoia National Park helped make this thesis possible. The cast list is long but I appreciate each of you. Particularly, I'd like to thank Scott Roberts for all of his work in the field. Many thanks are owed to Peter Kirchner who invested years in the Marble Fork area installing and maintaining the sensor network and conducting surveys. Roger Bales and the Sierra Nevada Research Institute helped to fund the field study and gave valuable feedback on Chapter 2. Michael Lehning graciously provided the snow and land surface model used in the study as well as support and compelling feedback on Chapter 3. Mathias Bavay provided tireless support and guided me through the inner mechanics of the SNOWPACK and Alpine3D models.

VITA

2003	B. S., Geology University of Vermont, Burlington, VT
2006	M. S., Hydrology University of Arizona, Tucson, AZ
2007-2012	Graduate student researcher University of California, Los Angeles
2008-2010	NASA Earth System Science Fellowship recipient
2010-2012	Visiting graduate student Institute of Arctic and Alpine Research, Boulder, CO
2011	Outstanding Student Poster Award recipient 2011 Eastern Snow Conference, Montreal, Quebec, Canada
2012	Ph.D., Civil Engineering UCLA, Los Angeles, CA

PUBLICATIONS

Musselman, K.N., N.P. Molotch, S.A. Margulis, P.B. Kirchner, and R.C. Bales (2012). Influence of canopy structure and direct beam solar irradiance on snowmelt rates in a mixed conifer forest, *Agricultural and Forest Meteorology*, Vol. 161, pp. 46-56, ISSN 0168-1923, 10.1016/j.agrformet.2012.03.011.

Huang, C., S.A. Margulis, M.T. Durand, and K.N. Musselman (2012). Assessment of snow grain-size model and stratigraphy representation impacts on snow radiance assimilation: Forward Modeling Evaluation, *IEEE Transactions on Geoscience and Remote Sensing*. PP(99) , 1-14.

Musselman, K.N., N.P. Molotch, S.A. Margulis, M. Lehning, and D. Gustafsson (in press). Improved snowmelt simulations with a big-leaf canopy model forced with photo-derived direct beam canopy transmissivity. Accepted for publication in *Water Resources Research*.

López-Moreno, J.I., S. Fassnacht, J.H. Heath, K.N. Musselman, J. Revuelta, J. Latron, E. Morán, and T. Jonas (in review). Spatial variability of snow density over complex alpine terrain: implications for estimating snow water equivalent. Submitted to *Advances in Water Resources*.

Perrot, D.O., N.P. Molotch, K.N. Musselman, E.T. Pugh (in review). Modeling the effects of the mountain pine beetle on snowmelt in a subalpine forest. Submitted to *Ecohydrology*.

FIRST-AUTHOR PRESENTATIONS

Musselman, K.N., N.P. Molotch, and S.A. Margulis (December 2008). Spatial, seasonal and inter-annual variability of snow accumulation control mechanisms in two neighboring alpine and sub-alpine catchments in California's seasonally snow-covered southern Sierra Nevada, paper presented at the 2008 AGU Fall Meeting, San Francisco, CA.

Musselman, K.N., N.P. Molotch, S.A. Margulis, P.B. Kirchner, and R.C. Bales (December 2009). A mechanistic approach for estimating snowpack dynamics in a conifer forest, paper presented at the 2009 AGU Fall Meeting, San Francisco, CA.

Musselman, K.N., N.P. Molotch, and S.A. Margulis (June 2010). A physically-based approach to improving estimates of snow states and fluxes in a conifer forest of Sequoia National Park, paper presented at the 2010 Eastern Snow Conference Annual Meeting, Hancock, MA.

Musselman, K.N., N.P. Molotch, S.A. Margulis, M. Lehning, P.B. Kirchner, and R.C. Bales (December 2010). Simulating plot-scale variability of snowpack states in conifer forests using hemispherical photography and a process based one-dimensional snow model, paper presented at the 2010 AGU Fall Meeting, San Francisco, CA.

Musselman, K.N., N.P. Molotch, and S.A. Margulis (June 2011). The use of detailed forest structure to explain plot scale snowmelt patterns in a conifer forest: improving physically based model representation of sub-canopy hydrometeorology, paper presented at the 2011 Eastern Snow Conference Annual Meeting, Montreal, Quebec, Canada.

Musselman, K.N., N.P. Molotch, S.A. Margulis, and M. Lehning (December 2011). Inter-annual snow accumulation and melt patterns in a sub-alpine mixed conifer forest: results from a physically based snow model, paper presented at the 2011 AGU Fall Meeting, San Francisco, CA.

Chapter 1. Introduction

1.1 Snow as a water resource

The importance of reliable water resources is notable in regions where supply is limited, demand is increasing, and the ability of management systems to adequately adapt to future changes in the hydrologic system is uncertain. Like many semi-arid regions worldwide, California relies upon runoff that originates as mountain snow to sustain its agricultural industry and a growing population. Conservative estimates indicate that greater than 50% of developed water in the state is derived from snowmelt, and the small fraction not used by agriculture supports municipal demand. In 2007, California's agricultural sector reported a net cash income of $75 billion (CDFA, 2009) and the state's population exceeded 38 million (CDF, 2009), emphasizing the fiscal and societal relevance of the snow-dominated hydrological regime. Much of the reason for these staggering numbers is California's geographically varied climate. The climate is characterized by a winter-dominated seasonality of annual precipitation (Tonnessen, 1991) and its geographic variability is a result of diverse topography owed largely to its prominent mountain range, the Sierra Nevada. The range's height, perpendicular orientation to prevailing synoptic winds, and proximity to the Pacific Ocean produce upper elevation annual precipitation totals that range from four to six times greater than those measured in valley locations (Daly et al., 1994; NOAA, 1985). At elevations above 1800 m, more than 75% of that annual precipitation falls in the form of snow (Stephenson, 1988) and temperatures maintain winter snow coverage until the spring warmth initiates melt and the relatively slow release of stored water. In this regard, snowmelt provides the predominant annual input to ecosystems,

aquifers, rivers and, ultimately, to downstream agricultural and metropolitan users through vast networks of reservoirs and aqueducts. Thus, mountain snowpack represents a critical component of California's water resource infrastructure in that it affords reliable water during otherwise arid summers when demand is highest.

The sustainability of the state's water resources is fundamentally reliant upon accumulated winter precipitation and spring snowmelt in mountainous areas. At the same time, these processes can cause disastrous floods. Continuous and accurate monitoring of precipitation and snowmelt dynamics is required to mitigate such risk and inform resource management decisions. Currently, this information is gathered from remote weather stations and manual snow surveys at specific locations. The data are compared to historical trends to estimate flood hazard and make water supply forecasts (LADWP, 2012). *Mote et al.* (2006) suggest that present and future variations in climate require more robust models that are less reliant upon historical records. Many regional and global scale climate and hydrological models have ad hoc treatment of the physics governing snowpack development and depletion (Marks et al., 2001; Pomeroy et al., 1998a), although recent efforts to improve regional climate model representation of snow are commended (e.g. Barlage et al., 2010; Livneh et al., 2010; Niu et al., 2011). Realistic hydrologic predictions in mountainous areas require explicit model representation of the meteorology as well as the effects of local terrain and forest cover that engender variability in snowpack dynamics (Shamir and Georgakakos, 2005) and ultimately govern the timing and magnitude of seasonal runoff.

1.2 The variability of snow properties

Many physical processes are known to influence the variability of snow cover. For example, precipitation itself is highly variable and is generally enhanced at higher elevations (Seyfried and Wilcox, 1995) and in orographically favored regions (Elliot and Shaffer, 1962). Snow redistribution by wind can significantly add to snow cover heterogeneity (e.g. Trujillo et al., 2007). This variability is further compounded by snow ablation (i.e. melt and sublimation) patterns. Snow ablation patterns are mutually determined by spatial (e.g. terrain and vegetation) or both temporal and spatial (e.g. temperature, radiation, wind, etc.) factors. The spatial variability of snow water equivalent (SWE) in mountainous regions is therefore an integration of dynamic meteorological processes (Marks et al., 2003) and interactions with physiography (i.e. terrain and vegetation) that form and affect a snowpack over the duration of its existence. For example, in mid-latitude regions (e.g. the Sierra Nevada, California), solar radiation comprises more than 70% of the net snowpack energy balance (Aguado, 1985; Marks et al., 1992). As a result, snowmelt patterns largely reflect the heterogeneous distribution of surface shortwave irradiance. Spatiotemporal patterns of solar irradiance are determined by solar elevation, local and regional terrain, cloud cover, and particularly, forest vegetation.

It is estimated that ~ 19% of Northern Hemisphere snow cover overlaps forest vegetation (Rutter et al., 2009) and that fraction is likely closer to 60% in many mountainous regions where the majority of snow water resources accumulate. Forested environments exhibit high snow cover heterogeneity over short distances as a result of vegetation interactions with incident above-canopy atmospheric fluxes that form complex mosaics of net precipitation and energy at the sub-canopy surface (Musselman et al., 2012). The physical mechanisms in forested

environments that control gradients in snow interception, sublimation and throughfall (e.g. Hedstrom and Pomeroy, 1998; Koivusalo and Kokkonen, 2002; Lundberg et al., 1998; Storck et al., 2002), shortwave (e.g. Ellis and Pomeroy, 2007; Hardy et al., 2004; Pomeroy and Dion, 1996) and longwave (e.g. Essery et al., 2008b; Pomeroy et al., 2009) radiation, and the local advection of momentum, heat and moisture fluxes (e.g. Liston, 1995; Price and Dunne, 1976) are well documented. Spatial snowmelt patterns beneath the canopy are dictated by forest architecture and resulting sub-canopy energy gradients. The forest canopy structure and particularly the fraction of canopy coverage, also known as the canopy 'closure', can vary at many scales (Hopkinson and Chasmer, 2009) (Figure 1.1), thus impacting the variability of snowmelt rates. For example, *Musselman et al.* (2012) and *Talbot et al.* (2006) showed that patterns of sub-canopy shortwave irradiance explain ~ 60% of the variability in snowmelt rates. *Pomeroy et al.* (2009) documented a strong positive relationship between the attenuation of shortwave radiation by canopy elements and locally enhanced longwave irradiance at the snow surface. The results imply that spatial patterns of sub-canopy long- and short-wave irradiance are not strictly independent, further complicating snowmelt patterns in forested areas.

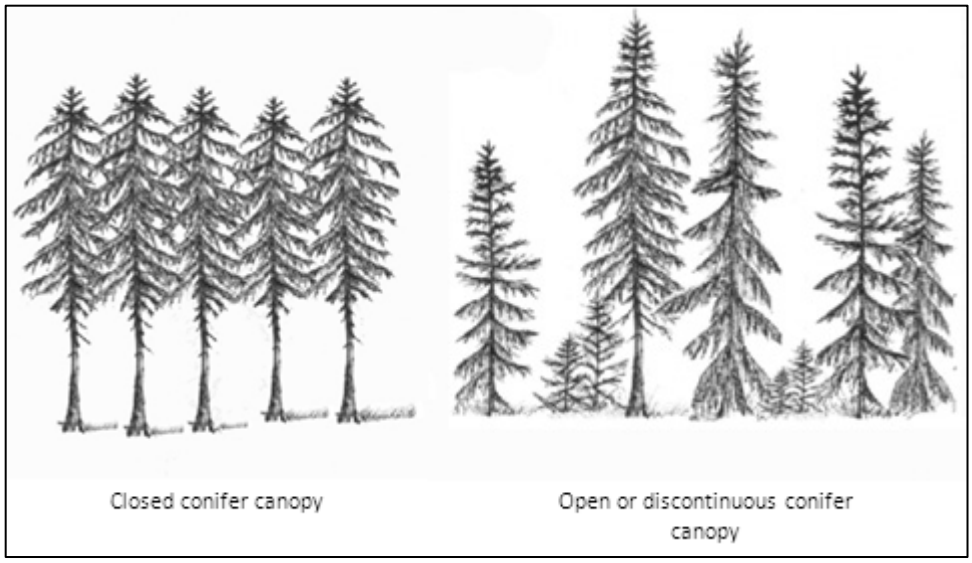

Figure 1.1. Illustrative schematic of different degrees of forest canopy closure. Modified from *Hopkinson and Chasmer* (2009).

The processes discussed above determine the variability in the timing of melt onset and snowmelt duration and ultimately the distribution of soil moisture (Bales et al., 2011; Molotch et al., 2009), infiltration, groundwater recharge, and streamflow (Seyfried and Wilcox, 1995). In this context, complex hydrometeorological processes govern the formation, storage, and release of water resources (Lehning et al., 2006) in mountainous environments. Such processes have extensive regional and global impacts, yet remain some of the greatest uncertainties in numerical land surface schemes and hydrological models (Marks et al., 2003), emphasizing the need for continued research.

1.3 Methods of characterizing snow water resources

1.3.1 Measurement techniques

Since the 1930's, snow water resources in the United States have been monitored by federal, state, and private cooperative snow surveys and often directed by the U.S. Department of

Agriculture's Natural Resources Conservation Service (NRCS, 2012b). The program and others like it have evolved to include extensive automated networks of remote stations that collect snow properties and related climate data (NRCS, 2012a). However, these observations must be extrapolated across variable terrain and forest cover to estimate the catchment-scale SWE distribution. Remote sensing techniques have great utility for characterizing snow properties over large areas, but continue to face limitations in forested regions and particularly in steep, forested terrain.

Direct measurements are useful to gain a better understanding of the mechanisms discussed above, including interactions with soil moisture and vegetation response. In this regard, heavily instrumented research sites have been developed to monitor the spatial and temporal relationships between snow accumulation and melt patterns, the distribution of soil temperature and moisture, and vegetation structure (e.g. Bales et al., 2011; Molotch et al., 2009; Musselman et al., 2008; Musselman et al., 2012; Vivoni et al., 2008) (Figure 1.2).

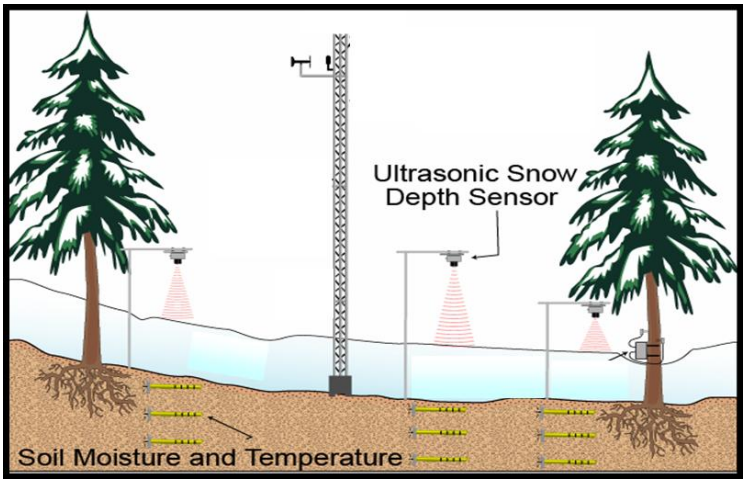

Figure 1.2. Schematic example of the instrumentation used in this study to monitor plot-scale hydrometeorology. Modified from Molotch et al. (2009).

For an exhaustive review of the measurement methods the reader is referred to the literature cited

above. The measurements represent tools with which to build understanding of the underlying processes, as well as to evaluate numerical models at a variety of scales.

1.3.2 Modeling methods

A half-century of thorough inquiry has established numerical representation of the effects of wind (e.g. Schmidt, 1982), topography (e.g. Meiman, 1968), and vegetation (e.g. Golding and Swanson, 1978) on snow distribution. However, the complex relationships between these variables and their high variability in time and space and at different scales continue to challenge snow model predictive skill (Jost et al., 2007). Despite these challenges, the need for accurate predictions of snow water resources has prompted the development of operational numerical snow models for a range of applications (Essery and Etchevers, 2004) including hydrological forecasting (e.g. Anderson, 1986), weather prediction (e.g. Niu et al., 2011), avalanche forecasting (e.g. Lehning et al., 1998), climate modeling (e.g. Bonan, 1998), and retrieval of snow characteristics by remote sensing (e.g. Mätzler and Wiesmann, 1999).

Snow models differ in their degree of process representation (Tarboton et al., 2000) depending on the intended application (Essery and Etchevers, 2004). Snow models generally fall into two categories: temperature index models and energy balance models (Hock, 2003). Temperature index models use empirical relationships between local air temperature and snowmelt to estimate snow depletion (Ohmura, 2001). However, these models are limited in their application because they do not explicitly address the physical snowpack dynamics and energy fluxes necessary to accurately predict small-scale spatial heterogeneity, changes in climate, or snowmelt beyond the range of model calibration. Energy balance snow models, on the other hand, are designed to simulate all energy fluxes into and out of a snowpack and are

used to predict snowmelt as a result of the computed net internal energy. These process-based models have been shown to yield improved local SWE estimates over temperature index methods (Walter et al., 2005). Even within a general snow model category, models differ in their representation of snowpack stratigraphy and vary from single layer (e.g. Essery, 1998; Schlosser et al., 1997), to three-layer (e.g. Sun and Xue, 2001), to detailed multilayer (e.g. Brun et al., 1992; Jordan, 1991; Lehning et al., 1998) snowpack representations. Detailed knowledge of the internal snowpack structure is critical for radiative transfer applications in remote sensing (Wiesmann and Mätzler, 1999) and avalanche forecasts (Lehning et al., 1999) and has shown utility in hydrological and climate research applications (Bavay et al., 2009), presumably due to the correlation between snow material structure and surface – atmosphere interactions.

For purposes of runoff estimation, simple melt models such as temperature index approaches and simplified, parameterized energy balance snow models have shown utility when judiciously calibrated to the specific basins to which they are applied. However, such heavily parameterized models often mask individual surface process interactions through an implicit treatment of the natural physics at the expense of numerical simplicity.

1.3.2.1 Physically based models

Through the use of more detailed models, it is possible to quantify and improve understanding of these process interactions and their individual impacts on catchment hydrology and snow cover distribution (Lehning et al., 2006). Process-based snow models also offer the opportunity to benefit from the increased availability and performance of satellite remote sensing techniques to validate individual model states or improve state estimates through data assimilation (Durand et al., 2008b; Lehning et al., 2006; Schmugge et al., 2002). Recent

advances have increased the predictive accuracy and physical representation of basin SWE yield, runoff, snow stratigraphy and surface characteristics, soil moisture distribution, stream chemistry, and ecological processes. One of the most detailed process-based land surface models with a particular emphasis on snow processes in complex terrain is the Alpine3D model suite (Lehning et al., 2006). Various components of this model suite, including the one-dimensional snow model SNOWPACK, are used in this thesis. Model details are provided in subsequent sections.

1.3.2.2 Model treatment of forest vegetation cover

Numerical modeling is the only feasible method of representing SWE beneath a forest canopy over large areas due to the small number of forested observation systems and limitations of remote sensing in forested regions (Rutter et al., 2009). The main challenge in canopy model development is the accurate representation of the upper boundary conditions of the snow (or bare soil) beneath the canopy. In addition to accounting for the influence of the canopy on radiative and turbulent heat fluxes at the snow/soil surface, physically-based models must explicitly treat interception and throughfall of precipitation, the sublimation and evaporation of intercepted precipitation, and the canopy albedo adjusted for the effect of intercepted snow. Even with high process-level detail, models require conceptual representation of otherwise complex, three-dimensional canopy structure. Empirical relationships between measured states and fluxes and bulk canopy structure metrics are then used to predict canopy processes. Model representations of these forest canopy metrics differ, which complicates attempts to quantify canopy model uncertainty (Essery et al., 2009).

An inter-comparison study of 33 snowmelt models by *Rutter et al.* (2009) found that

model errors were greater at forested sites than open sites. In addition, individual models showed inconsistent performance between different forested sites and particularly between paired forested and open sites in the same year. These model inconsistencies, observed under optimal point-scale conditions, are further compounded when models are distributed to the catchment-scale.

Model treatment of canopy interception of precipitation and the attenuation of momentum and heat fluxes are well established and beyond the scope of this study. Rather, the strong correlation documented between sub-canopy snowmelt rates and shortwave irradiance (e.g. Ellis et al., 2010; Hardy et al., 2004; Musselman et al., 2008; Musselman et al., 2012; Talbot et al., 2006) makes a compelling case for the evaluation of canopy radiative transfer (RT) techniques. Canopy models vary in their representation of RT from simple bulk approximations to complex treatments of the effects of individual canopy elements on attenuation, reflection and transmission of radiation. The more complex methods require detailed canopy structure parameters (e.g. Li et al., 1995; Ni et al., 1997). In practice, however, models that are physically realistic but employ only those parameters that are routinely available may be preferable (Nijssen and Lettenmaier, 1999). Many of the simpler or larger-scale models employ a one-dimensional "big-leaf" canopy representation. This canopy model design is used in this study and is described in detail in Chapter 3 and Appendix A.

Physically based snowmelt models are well suited to evaluate the complex linkages between meteorology, forest cover, snow accumulation and melt, and the basin-scale water balance (e.g. Lehning et al., 2006; Pomeroy et al., 2007). The ability of a physically based snow – canopy model to simulate these processes is limited, in part, by the difficulty of obtaining

detailed canopy structure information (Tribbeck et al., 2004). Additionally, the error associated with validating simulated snowmelt rates under different canopy conditions is large (Nijssen and Lettenmaier, 1999). For example, issues of scale arise when a canopy model commonly parameterized by bulk canopy metrics (e.g. area-averaged leaf area index or canopy density) is used to estimate heterogeneities in sub-canopy hydrometeorological processes as measured at a few point-scale locations. This study evaluates many of these scale issues by making use of the direct, automated measurements made at intensive research sites (Figure 1.2).

1.4 Motivation for improving snowmelt model estimates in forested environments

The significant hydrologic contribution from seasonally snow covered forested elevations of the Sierra Nevada emphasizes the need for numerical models to accurately represent these complex mass and energy fluxes. Yet model skill has been shown to be most limited in forested areas (Rutter et al., 2009). Furthermore, the lower elevation of forested regions relative to alpine areas makes forests particularly sensitive to climate change. These regions are at risk of a hydrologic transition from a snow-dominated regime characterized by a single spring melt pulse to one that experiences temporally discontinuous snow coverage and is dominated by synoptic-driven runoff events (Beniston, 2003). A discernible science gap has been identified that limits accurate representation of the Sierra's current and future hydrologic regime and the role of snow in these sub-alpine systems. Additionally, forest fire, insect kills, and climate change impact forest distribution and alter soil moisture and catchment water yield (e.g. Kurz et al., 2008; Pomeroy et al., 2012; Tague et al., 2009). Although the net effect of such changes on snow

distribution remains unclear, it is certain that forest – snow processes are likely to become more, rather than less, important in the future (Rutter et al., 2009).

The growing need and reduced accuracy of models to predict water resources in forested environments motivates the current research. This work evaluates the distribution of snow in forested and alpine terrain using a multi-scale measurement approach that includes 1) in-situ observation of snow and soil moisture dynamics over multiple years, 2) high-resolution canopy and terrain metrics associated with each observation, 3) an evaluation of the ability of a physically based one-dimensional snow model to simulate the observed snow and soil moisture dynamics, 4) the use of a distributed land surface model to examine scale relationships as evaluated against a unique suite of point-scale and distributed observations. The overarching science questions addressed in this thesis are thus: *What are the limitations of physically based models to simulate observed snowmelt variability in forested regions? How could the models be improved? And how do model limitations observed at the plot-scale impact larger-scale estimates of snow water resources in mountainous terrain?*

1.5 Organization of the thesis

In Chapter 2, the relationships between measured sub-canopy snowmelt and canopy metrics are evaluated for three years of observation. In Chapter 3, the accuracy of the point-scale snow – canopy model to predict sub-canopy snow cover dynamics is examined. A modification of the canopy model structure is introduced that permits the model to explicitly account for location-specific, time-variant solar direct beam canopy transmissivity. Chapters 2 and 3 address the questions: *how do sub-canopy snowpack processes vary in time and space and do the*

relationships observed during a single year hold over multiple water years? And *what level of canopy structure detail is necessary to simulate the observed dynamics?* Chapter 3 provides a description of a typical big-leaf canopy model and a summary of the model used in this study is provided in Appendix A. In Chapter 4, the distributed land surface model Alpine3D is introduced and run for three water years over a large domain. The domain encompasses a multi-scale measurement campaign that included high-resolution LiDAR, MODIS satellite data, repeated catchment-scale snow surveys, and point-scale observations of SWE, depth, and soil moisture. In Chapter 5, the major findings are summarized and directions for future research are discussed.

Chapter 2. Influence of canopy structure and direct beam solar irradiance on snowmelt rates in a mixed conifer forest

The heterogeneous arrangement of tree boles, branches, needles and understory together with micrometeorology and terrain dictate the physical processes summarized in Chapter 1 and ultimately govern the hydrology and ecology of many seasonally snow-covered forested catchments. Relative to open areas, a general dichotomy in forest - snow processes has been identified in which conifer canopy cover reduces the total annual meltwater available to runoff and/or infiltration through interception losses (Essery et al., 2003; Hedstrom and Pomeroy, 1998), while sub-canopy snow ablation processes determine the duration of snow cover and meltwater inputs (Link and Marks, 1999; Liston, 1995). The structure of vegetation combined with seasonal variations in solar elevation and cloud cover largely governs snow ablation patterns by determining the forest radiation regime (Baldocchi et al., 1984; López-Moreno and

Stähli, 2008; Stähli et al., 2009). Whether forests become snow-free before or after nearby clearings is found to be a function of latitude, forest structure, climate and seasonal meteorology (Faria et al., 2000; Molotch et al., 2011; Rutter et al., 2009; Schleppi, 2011; Sicart et al., 2004).

Shade from solar radiation provided by forest cover has been shown to explain more than 60% of the variability in snowmelt rates between different stands of the same tree species (Talbot et al., 2006). As a result, the date of snow disappearance at the forested plot scale (i.e. 40 x 40 m) can vary by as much as one month (Molotch et al., 2009) greatly impacting the magnitude of peak flows, the partition of meltwater to infiltration or runoff (Pomeroy et al., 2001) as well as seasonal soil moisture dynamics (Bales et al., 2011). The results imply that sub-canopy hydrometeorological surface fluxes and related states are well correlated with canopy cover 'upstream' of the prevailing flux paths. For example, the solar irradiance at a given sub-canopy location is most influenced by canopy configuration in the sky direction defined by the solar coordinates. Provided detailed canopy structure information, a consideration of the prevailing energy flux trajectories through a forest canopy may inform the derivation of optimal canopy metrics to improve energy flux parameterizations in canopy models.

Numerous empirical studies report correlations between snow properties and general descriptors of sub-canopy position relative to tree crowns such as 'open', 'edge', and 'under' categorizations (e.g. Musselman et al., 2008; Veatch et al., 2009). Others have compared snow depth or snow water equivalent (SWE) measured in canopy gaps of various sizes to that measured beneath the canopy (e.g. Golding and Swanson, 1986; Pomeroy et al., 2002). The results of these studies generally lack a pathway to predictive applications beyond the physiographic, climate, and weather conditions under which they were developed. A more

detailed collection of canopy structure data in plot-scale studies permits an explicit evaluation of processes that influence snow ablation. In this regard, the objective of this study is to identify impacts of forest canopy structure and subsequent differences in direct beam solar irradiance on measured snow ablation. Two science questions are addressed: 1) *Do canopy metrics derived from hemispherical photos explain observed spatial variability in snow ablation rates?* and 2) *Do optimal canopy metrics exist (either bulk or detailed descriptors) that can be used to explain observed variability in snow ablation rates?*

Section 2.1 describes the measurement and evaluation methods utilized in both Chapters 2 and 3, including a description of the study area and the hydrometeorological dataset. The results are reported and discussed in Section 2.3. Finally, a summary of conclusions of Chapter 2 is presented in Section 2.4.

2.1 Data and methods

Three years of seasonal SWE ablation as measured by a network of 24 ultrasonic snow depth sensors and manual snow density surveys were compared to: 1) photo-derived estimates of cumulative sub-canopy direct beam solar irradiance during the period of observed ablation; and 2) sky view factor (SVF_θ) computed over the full hemispherical range of zenith angles at one-degree increments. The direct beam irradiance, derived from detailed canopy transmissivity and above-canopy measurements, was used in explicit recognition that direct beam solar irradiance contributes significantly to the spatial variability of the sub-canopy energy budget. The canopy metric SVF_θ was used in implicit recognition that the majority of above-canopy diffuse, longwave, and turbulent fluxes enters the canopy from all sky directions above the effective

horizon, and may also hold information relevant to the estimation of terrestrial longwave fluxes. The analyses cover a range of elevation, slope, aspect and canopy configuration and three snow seasons (i.e. water years 2008 - 2010).

2.1.1 Study area

The study was conducted in the Wolverton basin, located in Sequoia National Park on the western slope of the southern Sierra Nevada, California, U.S.A. (36.59ºN, 118.717ºW) (Figure 2.1). The Wolverton basin is a 7.22 km^2, snowmelt-dominated, forested watershed. Elevation ranges from 2192 m to 3075 m asl. Conifer forest stands include red fir (*Abies magnifica*), white fir (*Abies concolor*), Jeffrey pine (*Pinus jeffreyi*) and Lodgepole pine (*Pinus contorta* subsp. *murrayana)*.

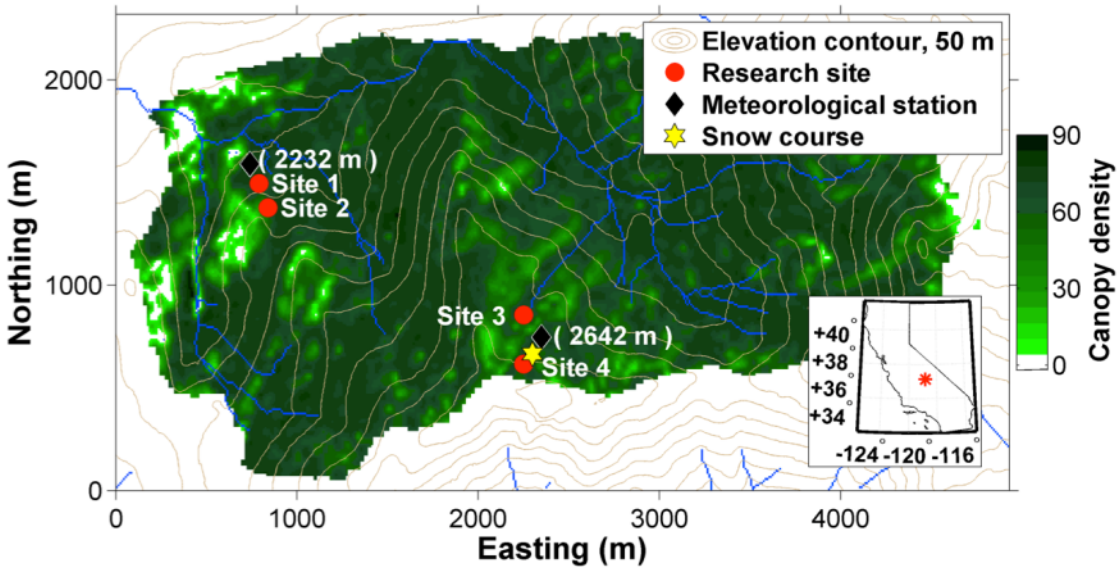

Figure 2.1. The Wolverton basin in Sequoia National Park, California. Locations of the four instrumented research sites and two meteorological stations (elevation in meters a.s.l) are indicated.

The forest is predominantly mature red fir, ranging in height from 20 - 50 m. The average canopy density is 65% and ranges from 0% in small clearings to 75% on steeper terrain with nearly continuous canopy coverage as determined from the National Land Cover Database (NLCD, 2001) (Homer et al., 2004) (Figure 2.1). A monthly snow course has been conducted since 1925 by the California Cooperative Snow Survey (CCSS) at elevation 2622 m asl. The average April 1st SWE for the historic record is 932 mm. The average wind velocity measured during winter and spring at the upper elevation (2642 m asl) meteorological station (Figure 2.1) for the three years of the study was 0.52 m s^{-1}, and the maximum daily wind velocity exceeded 3 m s^{-1} on only three occasions, indicating relatively little wind influence on local snow processes. In 2006, four extensively instrumented sets of sensor nodes (i.e. sites) were installed in the basin with locations stratified to represent the basin's range of aspect, elevation, and canopy cover (Table 1).

Table 2.1. Instrument site terrain and canopy statistics. The mean, maximum, and minimum values represent site variability sampled at locations of the six ultrasonic snow depth sensors.

	Elevation (meters)	Aspect, degrees from north			Slope, degrees			Canopy openness* 1-[canopy density] NLCD, 2001	$SVF_{90°}$		
		mean	max.	min.	mean	max.	min.		mean	max.	min.
Site 1	2253	5	-	-	22	-	-	0.26	0.19	0.25	0.16
Site 2	2300	78.6	160	5	14.2	15	10	0.42	0.21	0.23	0.17
Site 3	2620	79	95	40	7.3	10	0	0.57	0.29	0.40	0.21
Site 4	2665	10	-	-	12.6	20	8	0.44	0.25	0.27	0.21

* Canopy openness was determined from Landsat-derived NLCD, 2001 canopy density. Site values represent the average canopy openness as sampled at the location of the six snow depth sensors at each site.

2.1.2 Hydrometeorological measurements

Six ultrasonic snow depth sensors (Judd Communications) were installed at four locations representing different elevations, aspects, and forest canopy characteristics (Table 1) following *Molotch et al.,* (2009). The manufacturer specifies a senor range of 0.5 m to 10 m and

an accuracy of 1 cm or 0.4% of the target distance. Sensors at each site were separated by 8 - 55 m within the ~ 40 x 40 m site footprint. Snow depth observations were recorded hourly and processed to remove outliers and fill gaps following *Lehning et al.*, (2002a) (Figure 2.2). Snow density data were obtained from five, six and four snow density surveys conducted in 2008, 2009 and 2010, respectively (Figure 2.2). Snow density measurements at the four sites were obtained from approximately monthly (January - May) snow pits and CCSS snow course measurements. Snow pit density measurements made with 1000 cm^3 cutters were assumed to be representative of the plot-scale mean snow density. CCSS snow course density data represent the average of equally spaced Federal snow tube measurements made along multiple linear transects in close proximity to Sites 3 and 4 (Figure 2.1). In cases where both snow pit and CCSS measurements were conducted within one week of each other, only the snow pit density measurements were used to maintain consistency and site representativeness. For each year, the timing of maximum SWE was determined by multiplying surveyed site-specific density values by sensor snow depth values corresponding to the respective survey dates. The survey date that yielded the highest sensor SWE at all sites was prescribed as the date of maximum annual SWE. Given an estimate of maximum SWE at each depth sensor location for each year of the study, an index of the seasonal SWE ablation rate was then computed as the maximum SWE at a given sensor divided by the number of days from maximum SWE until snow disappearance as recorded by the same sensor. The approach yielded an ensemble of seasonal SWE ablation indices corresponding to different canopy configurations, elevations, aspects, and slopes of the individual snow depth sensor locations.

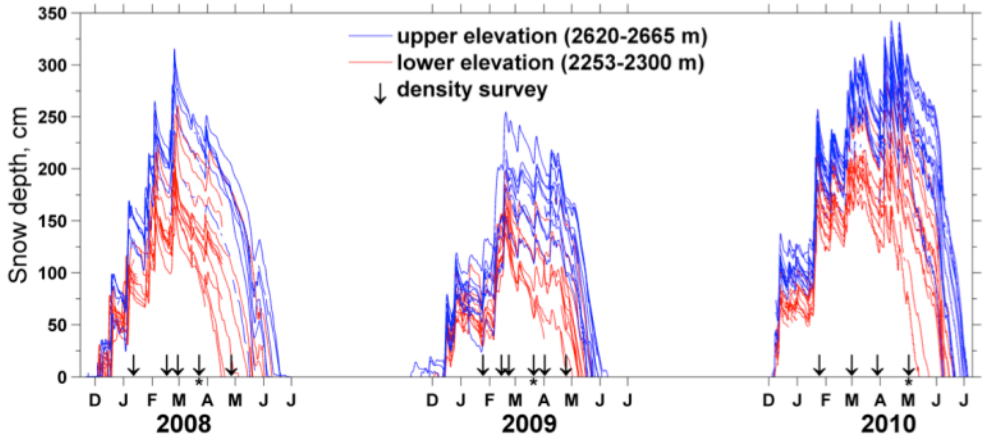

Figure 2.2. Hourly snow depth recorded by 24 ultrasonic sensors at two lower (sites 1 and 2) and two upper (sites 3 and 4) research sites and neighboring meteorological stations for three years. Dates of 15 snow density surveys (↓ symbols) and the survey dates determined to coincide with the timing of annual maximum SWE (* symbols) are indicated.

Obtaining manual snow density measurements on the date of maximum SWE is complicated by weather and schedule constraints and slight differences in terrain and forest cover that may cause spatial heterogeneity in the timing of maximum SWE. Two assumptions were made in regard to maximum SWE accumulation. First, the timing of maximum SWE was assumed to be uniform across sensor locations in a given year; that is, the date (not the magnitude) of maximum SWE was assumed to be spatially invariant. This assumption was necessary because SWE was not explicitly measured at each sensor location, but estimated only when density observations were available. Second, it was assumed that, for each year, one of the monthly density surveys captured the snow density at the time of maximum SWE. This assumption was necessary because density measurements were made at monthly repeat intervals.

Measurements of hourly, global incident solar radiation ($R_{s\downarrow}$) unobstructed by surrounding forest canopy were not available in the forested Wolverton basin. Instead, $R_{s\downarrow}$ for the three years of the study were obtained from a meteorological station located above timberline at

Topaz Lake in the Tokopah basin; 8 km ENE of the study site at 3220 m asl. The data were assumed to be representative of above-canopy $R_{s\downarrow}$ at the locations of the four sites. A four-day deployment of a Kipp and Zonen pyranometer in the Wolverton basin indicated cumulative differences with the Topaz Lake data of less than 4%. A three-year comparison of $R_{s\downarrow}$ measured at Topaz Lake and a station operated by the National Park Service 6 km WSW of the study site yielded a correlation coefficient of 0.93. Based on these two independent evaluations the use of Topaz Lake $R_{s\downarrow}$ measurements to represent above-canopy $R_{s\downarrow}$ in Wolverton is justified.

2.1.3 Hemispherical photography acquisition and analysis

An upward-looking hemispherical photograph was taken directly beneath each of the 24 depth sensors using a Nikon D700 digital single lens reflex camera (Nikon Corporation, Japan) with a Sigma 8 mm F3.5 EX DG Circular Fisheye Lens (Sigma Corporation, Japan). The camera was mounted on a tripod and photographs were taken at a height of 1.5 meters, roughly consistent with the seasonal average snow depth at the study sites. A bubble level fitted to the lens cap ensured horizontal camera orientation and a compass was used to orient the top of the camera to true north following methods of *Frazer et al.* (2000) (Figure 2.3a). The scientific image processing software Gap Light Analyzer (GLA) Version 2.0 (Frazer et al., 1999) was used to register and classify each digital hemispherical image following recommended methods of *Frazer et al.* (1999) and *Hardy et al.* (2004). The GLA image analysis created an image consisting solely of black and white pixels (Figure 2.3b).

To characterize canopy structural parameters from a pre-processed hemispherical photo, an automated image analysis model was developed. The model first determines the image center and assigns Cartesian coordinates to each pixel, in number of pixels, with nadir specified as the

central datum. The Cartesian coordinates are converted to a polar system such that each pixel is assigned a zenith angle (0 to $\pi/2$ radians) and an azimuth angle (0 to 2π radians) according to its position on the projected hemisphere. The coordinate system is defined such that an azimuth angle of 0 radians and a zenith angle of $\pi/2$ radians refer to the circular exposure's topmost central pixel and the azimuth angle increases in a counter-clockwise fashion consistent with the orientation of an inverted plan view compass rose. The quality of the exposure's circular extent (~ 2000 x 2000 pixels) permits high-resolution analysis. Radial projection errors are inherent to image acquisition. A five-piece polynomial was applied that adequately approximates the radial projection error provided by the lens manufacturer (Sigma Corporation, personal communication). Other sources of uncertainty associated with hemispherical photography include geo-reference errors and the subjectivity of RGB threshold specification.

2.1.4 Photo-derived canopy metrics

Sky view factor (SVF_θ) was computed from binary hemispherical images as the weighted canopy openness over all azimuth angles (φ) from a specified zenith angle (θ) to nadir. The metric has been successfully used in the study of forest light environments (e.g. Hardy et al., 2004), longwave radiation (e.g. Essery et al., 2008b) and sub-canopy snow dynamics (e.g. López-Moreno and Latron, 2008). When computed over a single hemispherical region defined by θ, SVF_θ is a bulk, 0-D representation of canopy openness over a select concentric area of the projected hemisphere. When computed over a range of θ angles from 1° to 90°, SVF_θ becomes a one-dimensional array that describes the change in canopy openness as more of the surrounding forest is considered. Figures 3c,d provide examples of SVF_θ computed at one-degree zenith angle increments over the field of view of a hemispherical photograph. In the example, SVF_θ is equal

to one nearest nadir, decreases slightly as a result of the overhead snow depth sensor until an angle of ~ 12° is reached, beyond which canopy elements begin to enter the field of view and SVF_θ decreases more significantly (Figures 3c,d). In this way, SVF_θ was computed for each hemispherical photo taken at depth sensor locations at one-degree intervals of θ from 1° to 90°.

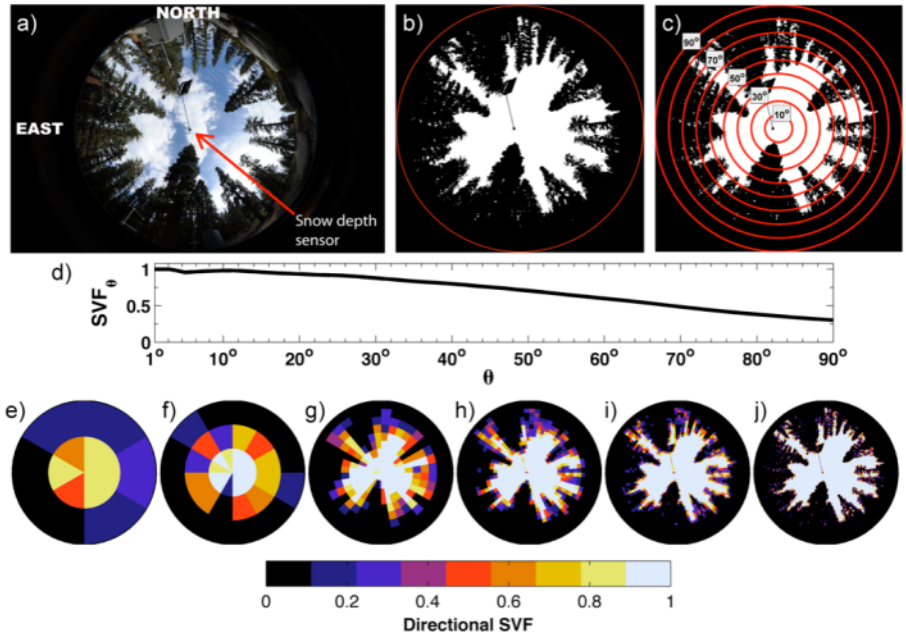

Figure 2.3. Processing and analysis steps of a hemispherical canopy photograph including a) a georeferenced digital hemispherical color photo (with location of the site 3, snow depth sensor #3 indicated), b) binary pixel representation of the color photo with the circular exposure outlined, c) photo with concentric circles defined by zenith angle, θ, d) the resulting sky view factor (SVF_θ) determined by integrating fractional canopy openness from specified zenith angles at 1° increments (1° - 90°) to nadir (0°) and e)-j) examples of the hemispherical photo aggregated into discrete sky regions to determine directional SVF at e) 12 sky regions or ~ 53º, f) 36 sky regions or 30º, g) 324 sky regions or 10º, h) 1296 sky regions or 5º, i) 3600 sky regions or 3º, and j) 32,400 sky regions or 1º angular resolutions.

2.1.4.1 Sky view factor

The explicit consideration of canopy openness as it might influence the direct beam solar flux entering the forest canopy in a specified trajectory is not achievable with bulk SVF_θ measurements. When computed over individual φ and θ ranges, however, SVF_θ gains a directional component (*directional SVF*) and becomes a two-dimensional (2-D) array that

describes the hemispherical distribution of canopy openness relative to a photo location at any angular resolution of interest. Pre-processed hemispherical images were divided into circumferential and radial solid angles, or sky regions, specified by angular increments $\delta\theta_i$, and $\delta\varphi_j$. The total count and fraction of sky / non-sky pixels in each sky region were computed and binned in matrices of size $\left[\frac{2\pi}{\delta\varphi_j}, \frac{\pi/2}{\delta\theta_i}\right]$, representing weighting schemes and *directional SVF*, respectively. Figures 3e-j illustrate examples of *directional SVF* computed over a specified range of φ and θ discretizations. An example in Figure 2.3e shows the projected hemisphere divided into six φ and two θ bands for a total of 12 sky regions at an angular resolution of 60° (φ) and 45° (θ). In this study, the estimated total uncertainty in radial pixel position was one-degree. For this reason, a one-degree hemispherical angular resolution was chosen, representing 360 azimuth and 90 zenith discretizations or a total of 32,400 sky regions (Figure 2.3j).

2.1.4.2 Directional sky view factor

The explicit consideration of canopy openness as it might influence the direct beam solar flux entering the forest canopy in a specified trajectory is not achievable with bulk SVF_θ measurements. When computed over individual φ and θ ranges, however, SVF_θ gains a directional component (*directional SVF*) and becomes a two-dimensional (2-D) array that describes the hemispherical distribution of canopy openness relative to a photo location at any angular resolution of interest. Pre-processed hemispherical images were divided into circumferential and radial solid angles, or sky regions, specified by angular increments $\delta\theta_i$, and $\delta\varphi_j$. The total count and fraction of sky / non-sky pixels in each sky region were computed and

binned in matrices of size $\left[\frac{2\pi}{\delta\varphi_j}, \frac{\pi/2}{\delta\theta_i}\right]$, representing weighting schemes and *directional SVF*, respectively. Figures 3e-j illustrate examples of *directional SVF* computed over a specified range of φ and θ discretizations. An example in Figure 2.3e shows the projected hemisphere divided into six φ and two θ bands for a total of 12 sky regions at an angular resolution of 60° (φ) and 45° (θ). In this study, the estimated total uncertainty in radial pixel position was one-degree. For this reason, a one-degree hemispherical angular resolution was chosen, representing 360 azimuth and 90 zenith discretizations or a total of 32,400 sky regions (Figure 2.3j).

2.1.5 Canopy radiative transfer model

Directional SVF has been used extensively to estimate solar canopy transmissivity (e.g. Becker et al., 1989; Frazer et al., 2000; Hardy et al., 2004; Sicart et al., 2004). In this study, the sky coordinates of the sun were used to 'sample' the *directional SVF* from the sky region encompassing the sun's position. The sun's position in the sky at one-minute resolution was computed for the three years of the study following methods of *Reda and Andreas* (2004), with an uncertainty of ± 0.0003º. A one-minute time scale was chosen to adequately capture the relative velocity (~ 0.25º per minute) of the sun's location on the projected hemispherical plane. Hourly measurements of above-canopy $R_{s\downarrow}$ were linearly resampled to one-minute estimates and used to estimate sub-canopy fluxes at the locations of hemispherical photos. Combined with one-degree resolution *directional SVF*, the one-minute time step captures the intermittent nature of sun flecks tracking on the forest floor and the resulting high temporal variability of the forest light environment. Differences in the physics of canopy attenuation / transmission of direct ($R_{s\downarrow dir}$) and diffuse ($R_{s\downarrow dif}$) solar radiation require these two components to be treated

independently. The $R_{s\downarrow dir}$ and $R_{s\downarrow dif}$ fluxes were partitioned from the above-canopy global shortwave measurements using the all-sky solar partition model presented in *Allen et al.,* (2006) as an empirical function of atmospheric transmissivity. The model provided one-minute estimates of above-canopy $R_{s\downarrow dir}$ and $R_{s\downarrow dif}$.

In this study, direct beam canopy transmissivity (*DBT*) is defined as the probability that the solar beam will pass through forest cover unimpeded by canopy elements at a given time and as determined at the location and height of a hemispherical photograph. *Directional SVF* sampled from sky regions corresponding to the track of the sun provided a high-resolution estimate of *DBT*. The model does not account for scattering of attenuated direct beam radiation. At every photo / depth sensor location, *directional SVF* and the trajectory of the sun in the sky were used to compute *DBT* for every minute of every day for the three water years of interest.

The one-minute detailed *DBT* was multiplied by the one-minute above-canopy $R_{s\downarrow dir}$ to estimate sub-canopy $R_{s\downarrow dir}$ on a horizontal plane. The direct beam irradiance estimated at the location of individual depth sensors was then projected on the local slope according to *Oke* (1988). The cumulative slope-projected direct beam irradiance calculated over the same time frame used to compute sensor-specific seasonal SWE ablation rates was used to test the correlation between the observed SWE ablation and estimated sub-canopy $R_{s\downarrow dir}$.

To evaluate the model's predictive accuracy of sub-canopy $R_{s\downarrow dir}$, canopy transmission of the above-canopy diffuse component was also estimated and the sub-canopy $R_{s\downarrow dir}$ and $R_{s\downarrow dif}$ fluxes were combined to represent the horizontal, sub-canopy global shortwave radiation. Estimates of sub-canopy $R_{s\downarrow}$ were then compared to pyranometer data. Unlike the source of the direct beam, which was treated as a point on the projected hemisphere, diffuse radiation may be

transmitted from all sky regions. The anisotropic sky distribution of diffuse radiation was treated with a simple cosine approximation such that more weight was applied to the near-nadir sky regions (i.e. lower zenith angles) and less toward the horizon. Diffuse solar irradiance entering the canopy is absorbed, reflected, or transmitted. The fraction of unimpeded diffuse irradiance was determined by the *directional SVF* of each sky region. Reflection of the fraction of diffuse light incident on canopy elements (i.e. *1 - directional SVF*) was approximated using an estimated canopy albedo and a Beer's-type exponential reduction as a function of effective leaf area index (*LAI'*). Photo-derived *LAI'* was computed following the gap fraction methods of *Norman and Campbell*, (1989) and accounting for a sloped surface as *Schleppi et al.,* (2007). The average *LAI'* from the 24 photos was 2.72 m^2 m^{-2} and the values ranged from 1.20 to 4.88 m^2 m^{-2}. The sub-canopy $R_{s\downarrow dif}$ issuing from any sky direction was estimated as:

$$R_{s\downarrow sub\_dif_{i,j}} = R_{s\downarrow dif} \cos\theta_i \left(1 - SVF_{i,j}\right)\left(1 - \alpha_c\right)\exp\left(-k \cdot LAI'\right) \qquad (1)$$

where k (-) is an extinction parameter typically between 0.4-0.8 and specified as 0.7, α_c is the conifer canopy albedo specified as 0.125, and $SVF_{i,j}$ is the *directional SVF* in the sky region defined by zenith angle i and azimuth angle j. An additional weighting scheme was necessary to account for the hemispherical effect of upper sky regions (i.e. solid angles) having less area than those nearer the horizon. Each sky region was assigned a weight defined as the pixel count for that region normalized by the total hemispherical pixel count. The weighted irradiance effectively permits all sky regions to contribute equally to the surface irradiance, computed as the summation of hemispherical weighted irradiance.

Model validation was conducted in two experiments. In the first experiment, upward-looking photographs were taken as close as possible to three mast-mounted pyranometers 3.5 m

above the forest floor. The pyranometers logged data for eight days at one-minute resolution. In the second validation experiment, a total of nine leveled Kipp and Zonen pyranometers were deployed on the snow surface for three days in radial transects centered on a cluster of 40 m trees near Site 3. The sensors were programed to log at five-minute intervals of ten-second integrated measurements. An additional, identically programed pyranometer located in a large clearing ~ 0.5 km WSW of Site 1 provided 'above-canopy' radiation.

2.1.6 Regression analyses

Linear regression analyses were conducted on the relationships between measured seasonal SWE ablation rates at the 24 locations for three years and: 1) estimates of cumulative sub-canopy direct beam solar irradiance during the period of observed ablation; and 2) SVF_θ computed over the full hemispherical range of zenith angles at one-degree increments. The coefficient of determination (R^2), slope, intercepts and statistical significance (p-value) were evaluated.

2.2 Results

2.2.1 Hydrometeorological observations

Hourly time series of snow depth measured by the 24 ultrasonic sensors for water years 2008, 2009, and 2010 show that accumulation and depletion rates varied between upper (Sites 3 and 4; 2620 m - 2665 m asl) and lower (Sites 1 and 2; 2253 m - 2300 m asl) elevations, between sites at similar elevations, and between sensor locations at individual sites (Figure 2.2). On average, the 12 sensors at the two lower elevation sites recorded seasonal maximum snow depths

of 203 cm, 154 cm, and 199 cm for the three years, respectively, while the 12 sensors at the two upper elevation sites recorded average maximum depths of 278 cm, 194 cm, and 307 cm for the same years. The lower elevation sites accumulated 73%, 79%, and 65% of the average maximum snow depth at the upper elevation research sites for 2008, 2009, and 2010, respectively. Maximum snow depth was recorded on 26 February, 2008; 19 February, 2009; and 21 April, 2010 and the dates did not vary by elevation. Snow density data (not shown) from each of the three years exhibited a seasonal increase with the springtime maximum snowpack densities between 450 kg m^{-3} and ~500 kg m^{-3}. The timing of seasonal maximum SWE was estimated to coincide with density surveys conducted on 23 March, 2008; 21 March, 2009; and 2 May, 2010 (Figure 2.2, Table 2). Average maximum annual SWE for lower and upper elevation sites, respectively, was 519 mm and 955 mm in 2008; 263 mm and 576 mm in 2009; and 817 mm and 1330 mm in 2010. The melt season duration, defined as the number of days between peak SWE and snow disappearance, was found to vary significantly by site, year, and lower (sites 1 and 2) and upper (sites 3 and 4) elevations (Table 2).

Table 2.2. Melt-season metrics.

	Date of	***Mean Snow disappearance date***				***Melt season duration, days*** *[min., mean, max.]*			
Year	***Peak SWE***	*Site 1*	*Site 2*	*Site 3*	*Site 4*	*Site 1*	*Site 2*	*Site 3*	*Site 4*
2008	Mar. 23	May 24	May 2	May 29	Jun. 14	[57, 62, 70]	[25, 40, 57]	[56, 70, 83]	[76, 84, 88]
2009	Mar. 21	May 10	May 3	May 25	May 30	[41, 50, 57]	[29, 43, 53]	[58, 66, 79]	[64, 70, 75]
2010	May 2	Jun. 13	May 30	Jun. 18	Jul. 1	[39, 43, 49]	[11, 29, 39]	[37, 47, 64]	[56, 61, 64]

2.2.2 Direct beam canopy transmissivity (DBT)

The *DBT* at the location of snow depth sensor #3, site #3 is illustrated in Figures 4a,b. In

the example, *directional SVF* is sampled along the solar disk trajectory (Figure 2.4a) at one-minute resolution between the hours of 4:00 and 20:00 PST for every day between the winter and summer solstices (Figure 2.4b). The daily (i.e. when the sun is above the horizon) mean *DBT* for this location (Figure 2.4c) has a seasonal minimum of 0.05 on 11 January, a seasonal maximum of 0.48 on 29 April, and the seasonal average of the mean daily *DBT* is 0.29. However, the high variability of the one-minute *DBT* is not well represented by the seasonal evolution of the daily mean as indicated by the near-zero median and 45th and 55th percentiles for much of the year (Figure 2.4c). The distribution of minutes when direct sunlight passes unimpeded through the canopy (i.e. $DBT = 1$) is heavily skewed toward solar noon (at the daily scale) and the summer solstice (at the seasonal or annual scale), but that general trend is dependent on location and surrounding forest structure.

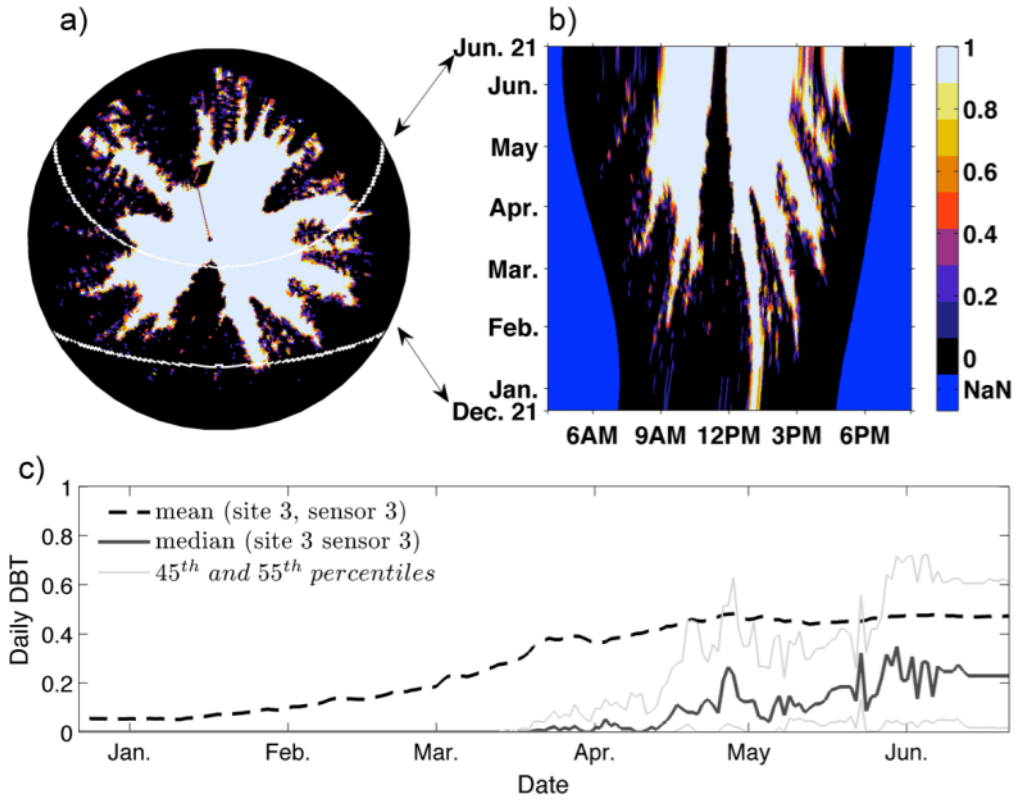

Figure 2.4. Directional SVF at one-degree angular resolution at the same depth sensor location as in Figure 2.3 showing a) the projected solar disk trajectory on the winter (lower) and summer (upper) solstices, b) directional SVF sampled along the sun track (i.e. direct beam canopy transmissivity, DBT) at one-minute (x-axis) resolution for every day (y-axis) between the solstices, and c) the seasonal variability including the mean, median, and the 45th and 55th percentiles of the daily mean DBT at the same location.

For example, the spatial variability of the seasonal distribution of daytime *DBT* computed between the solstices as in Figure 2.4b but at all 24 photo / snow depth sensor locations is illustrated in Figure 2.5a. The mean of the daily average *DBT* at all sensor locations varies from 0.044 to 0.32 between the winter and summer solstices, respectively (Figure 2.5b). The 24-sensor mean of the photo-derived *DBT* (0.19) is only slightly less than the photo-derived 24-sensor mean SVF_{90° (0.24; Table 1) - a surprising result given that SVF_{90° contains information about a much larger portion of the projected hemisphere than the angular swath defined by the solar

coordinates. However, particularly at time scales greater than one hour, the mean *DBT* does not correspond to sub-canopy potential direct beam irradiance without consideration of the highly variable nature of above-canopy solar radiation. In the analyses to follow, the photo-derived *DBT* was used to explicitly estimate sub-canopy direct beam solar irradiance in an effort to capture the highly dynamic nature of the sub-canopy shortwave environment.

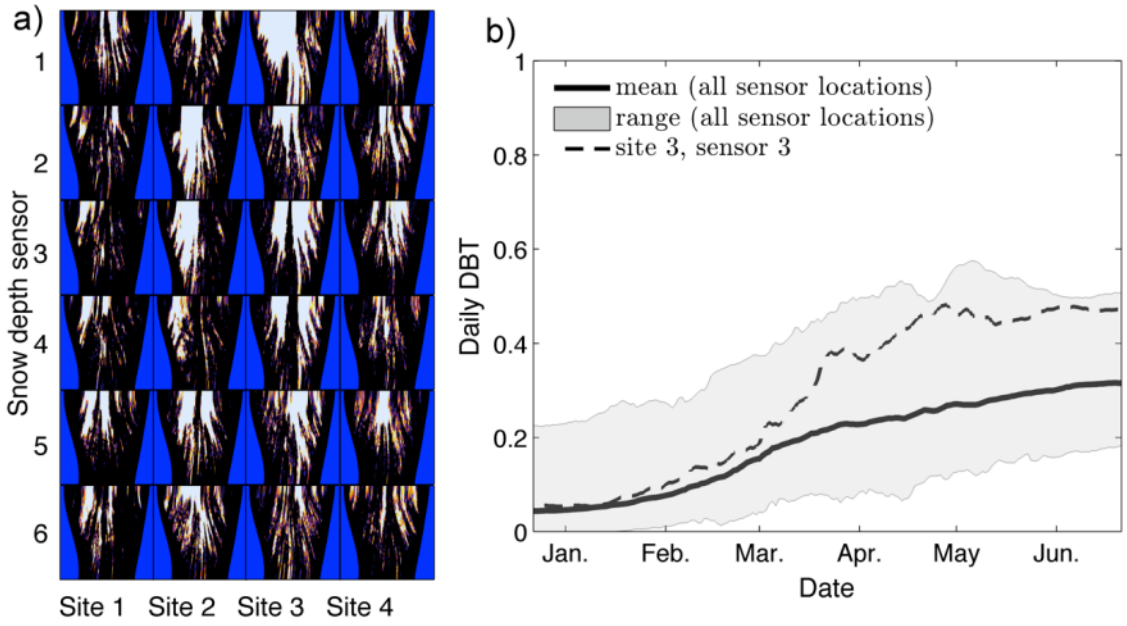

Figure 2.5. Direct beam canopy transmissivity (DBT) between the winter and summer solstices a) for all daylight hours as shown in Figure 2.4 but at the locations of all 24 snow depth sensors, and b) as the sensor network mean (solid line) and range (shading) of the daily average at all sensor locations and relative to the site 3, sensor 3 mean DBT (dashed line) shown in Figure 2.4.

2.2.3 Above-canopy radiation

Hourly measured above-canopy $R_{S\downarrow}$ data for the three years are shown in Figure 2.6; the darker horizontal bands indicate cloud cover (Figure 2.6). A daily clearness index, K_τ (Liu and Jordan, 1960) (Equation 2), was computed for the period between the spring equinox and summer solstice of each year as

$$K_\tau = \frac{R_{S\downarrow}}{R_{S\downarrow,\,TOA}} \qquad (2)$$

where $R_{S\downarrow,\,TOA}$ is the estimated horizontal solar flux received at the top of the atmosphere per unit area per hour, computed as *Allen et al.* (2006). Low (high) K_τ values represent low (high) radiation typically associated with cloudy (clear) sky conditions. However, no definitive thresholds exist by which to classify sky conditions based on K_τ (Okogbue et al., 2009). The threshold used to identify cloudy conditions varies by study from $K_\tau \leq 0.15$ (Okogbue et al., 2009) to $K_\tau \leq 0.35$ (Kuye and Jagtap, 1992). For this study, daily average K_τ was rarely less than 0.15 (Figure 2.6). As a result, a threshold of $K_\tau \leq 0.35$ was specified to estimate cloudy conditions. Based on this K_τ threshold, 4, 23, and 8 days were categorized as cloudy in 2008, 2009, and 2010, respectively (Figure 2.6).

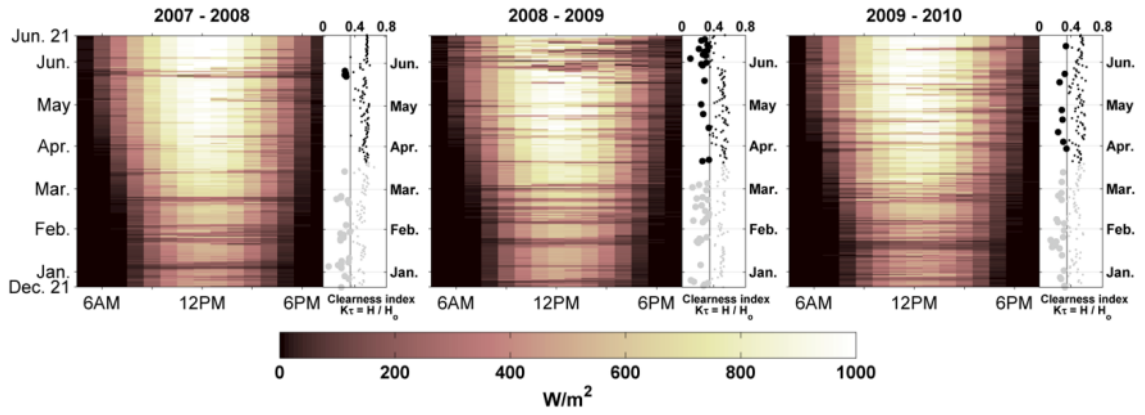

Figure 2.6. Hourly global shortwave $R_{s\downarrow}$ radiation measured at the Topaz Lake meteorological station between the winter and summer solstices of water years 2008, 2009, and 2010. Daily clearness indices (K_τ) for each year are shown in the vertical scatter plots. Darkened data points indicate days after the spring equinox for each year. Circles (● symbols) indicate days when $K_\tau \leq 0.35$ (i.e. 'cloudy'); the vertical black line indicates this cloudy / clear sky threshold.

2.2.4 Sub-canopy direct beam irradiance

An evaluation of the one-minute sub-canopy $R_{s\downarrow dir}$ at a single snow depth sensor location reveals the control of canopy structure on the transmission of the solar beam (Figure 2.7). Periods of cloud cover are identifiable in the time series of the simulated sub-canopy direct beam flux; note the rapid transitions from red to blue in the vertical line graph in Figure 2.7, indicating a shift in radiation dominance from the direct to diffuse light. Changes in daily average shortwave canopy transmission associated with temporally discontinuous cloud cover occur when clouds block the sun precisely when the direct beam would otherwise be transmitted through the canopy at a given location (Figure 2.7; note changes in the vertical line graph during cloudy (blue) periods).

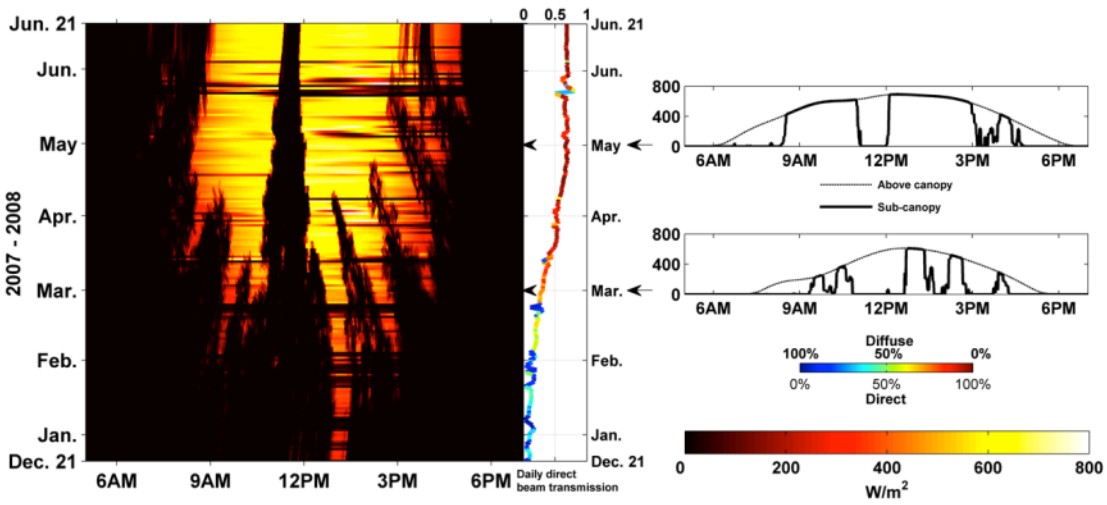

Figure 2.7. Modeled sub-canopy $R_{s\downarrow dir}$ for 21 December, 2007 – 21 June, 2008 (left) at the same photo location shown in Figure 2.4. The mean daily fraction of modeled sub-canopy to above-canopy direct beam irradiance (i.e. daily direct beam canopy transmission) is indicated by the vertical line graph and the daily fraction of total direct / diffuse irradiance is indicated by the line color. Diurnal examples of above-canopy (thin line) and sub-canopy (bold line) direct $R_{s\downarrow}$ for 1 March and 1 May, 2008 are included at right.

Diurnal cross-sections of the sub-canopy direct beam irradiance on 1 March (lower) and 1 May (upper), 2008 illustrate the variability in sub-canopy solar beam irradiance relative to the above-canopy flux and general increase over the two-month period (Figure 2.7; insets on right). The canopy transmission of the direct beam is therefore highly dynamic as a combined result of cloud cover and forest canopy structure coincident with the sky track of the sun (e.g. Figure 2.4). The average daily probability (in percent likelihood) of *DBT* plotted in Figure 2.5b was 12% and 37% in winter (21 December, 2007 - 21 March, 2008) and spring (21 March - 21 June, 2008), respectively, while for the same two seasons the direct beam comprised 46% and 75%, respectively, of the total global sub-canopy solar irradiance. The results suggest that even in winter, despite the relatively low daily average probability of solar beam canopy transmittance, the direct beam still represented much of the sub-canopy solar irradiance.

The first validation of simulated $R_{s\downarrow dir}$ conducted for eight days and evaluated against

data from three pyranometers yielded an average linear Pearson's correlation coefficient of 0.58 and a positive model bias of 9.9% was noted. The second validation experiment run at nine pyranometer locations for three days yielded an average correlation coefficient computed for the sub-canopy sensors and model estimates of 0.70 and a positive model bias of 7.1% was observed. Various error sources of the model and measurement designs likely contributed to the observed error and bias. Spatial offsets of as much as a few meters between the camera lens and pyranometer positions likely resulted in much of the observed error at the relatively high temporal resolution of the measurements and model estimates. The spatial offset between sensors and photographs effectively caused a temporal lag in the intermittent irradiance, reducing the correlation coefficient. The positive model bias could be attributed to a combination of error in the partition of above-canopy global radiation to direct and diffuse, hemispherical photo acquisition and analysis, and pyranometer measurement error at the base station (representing above-canopy) and/or the sub-canopy sensors. The potential influences of the various uncertainties on analyses and results are presented in the Discussion.

2.2.5 Regression analyses

The mean ablation rates for the continuously operational snow depth sensors were -11.7 mm day^{-1}, -7.2 mm day^{-1}, and -23.2 mm day^{-1} in 2008, 2009, and 2010, respectively (Figure 2.8). The mean cumulative sub-canopy direct beam irradiance from the date of maximum accumulation to the mean date of snow disappearance for the three years at the location of the continuously recording sensors was 365 MJ m^{-2} (23 March - 29 May, 2008), 274 MJ m^{-2} (21 March - 19 May, 2009), and 304 MJ m^{-2} (2 May - 17 June, 2010) (Figure 2.8). A total of 15, 12, and 19 sensors recorded SWE ablation rates in 2008, 2009, and 2010, respectively, and are used

in the following regression analyses.

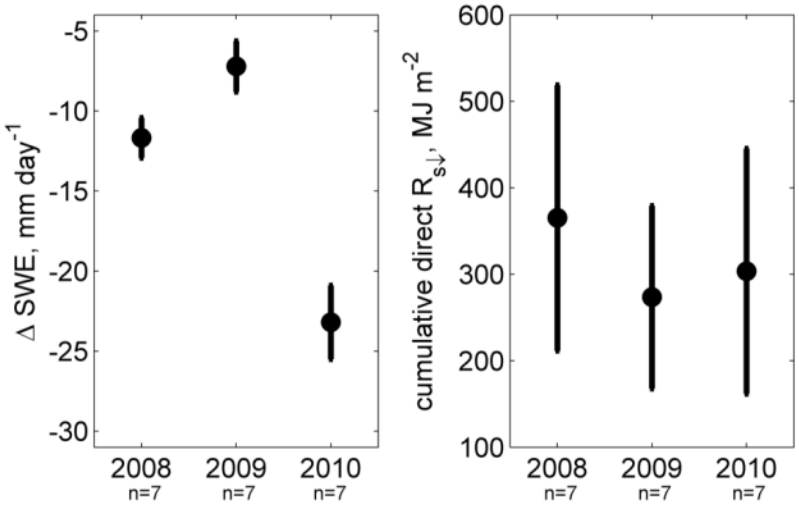

Figure 2.8. Mean (● symbol) and standard deviation (error bars) of measured seasonal SWE ablation rates (left) and modeled cumulative melt season sub-canopy direct beam irradiance (right) for years 2008, 2009, and 2010. For consistent inter-annual comparison, only data from seven continuously operational sensor locations are shown.

Generally, (negative) linear relationships were observed between seasonal SWE ablation (i.e. $\Delta SWE;$ with negative values indicating ablation) and modeled cumulative incident $R_{s\downarrow dir}$ (Figure 2.9). The estimated cumulative direct beam irradiance explained 58%, 29%, and 23% of the variation in seasonal SWE ablation in 2008, 2009, and 2010, respectively. The linear relationship of the 2009 data was not statistically significant at the 5% level. Years with greater sub-canopy direct beam irradiance exhibited a stronger relationship between ablation rates and direct beam irradiance. Sky view factor exhibits the same general (negative) linear relationship with SWE ablation, but the slope and statistical significance of that relationship is dependent on the specified range of zenith angles used to compute SVF_θ. The sensitivity of the observed relationships between ablation rates and SVF_θ were evaluated for sensitivity to seasonal inter-annual differences in cloud cover for three years of record.

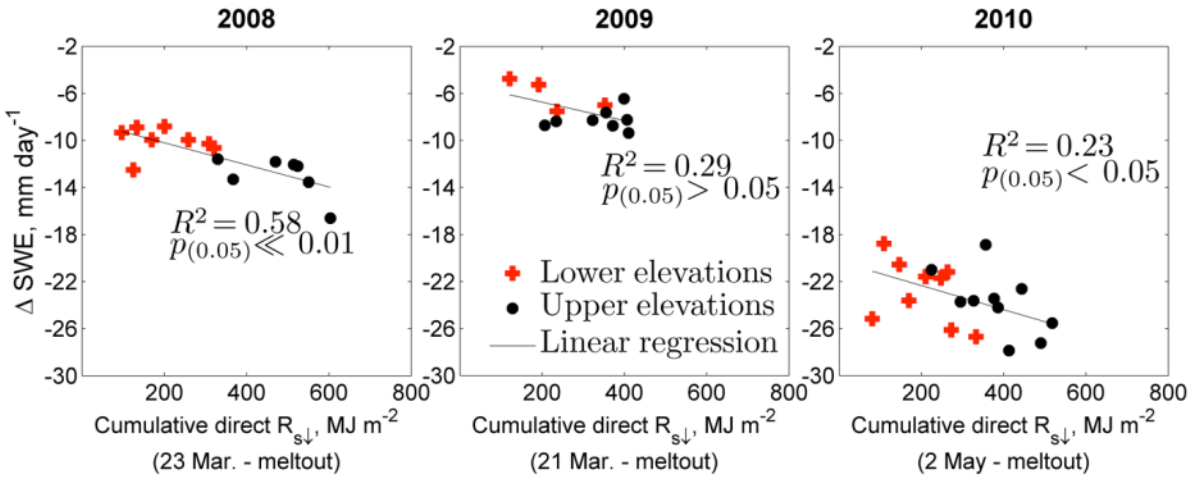

Figure 2.9. Linear regression trends between spring SWE ablation rate measured at snow depth sensor locations and corresponding modeled cumulative seasonal sub-canopy shortwave irradiance for years 2008 (n=15), 2009 (n=12), and 2010 (n=19).

Figure 2.10 shows the coefficient of determination of the linear regression analyses conducted on the SWE ablation rates observed for each of the three years and SVF_θ computed over successively larger sky regions. The optimal zenith angle used to compute SVF_θ that resulted in the strongest correlation with ablation rates varied for each of the three years: 90° in 2009, the cloudiest season, and 45° (2010) and 66° (2008); years with less cloud cover and more direct beam irradiance (Figure 2.10). The SVF_θ at these optimal zenith angles explained 41%, 87%, and 48% of the observed seasonal SWE ablation for the respective three years (Figure 2.11).

2.3 Discussion

At least four factors likely contributed to the variability of observed SWE ablation rates. First and most importantly, cumulative sub-canopy direct beam irradiance was largely governed by the spatial arrangement of forest vegetation in the sky direction of the sun's path. Second,

seasonal ablation rates are limited, in part, by the availability of incident solar irradiance, which varies seasonally with solar elevation. Hence, reduced ablation rates were observed at lower elevations (Figure 2.9) where snowmelt commences earlier in the year when solar elevations are lower. At upper elevations snowmelt continues later into the year (Figure 2.2) when solar elevations are higher, resulting in greater seasonal ablation rates (Figure 2.9). Third, snow ablation rates are governed by seasonal meteorology. Years with greater sub-canopy direct beam irradiance (and less cloud cover) exhibited a stronger relationship between seasonal ablation rates and direct beam irradiance (Figure 2.9). While $R_{s\downarrow dir}$ explained nearly 60% of the observed variability in SWE ablation for the most cloud-free ablation season, the remaining unexplained variability for this year and for years with more cloud cover highlights the role of other energy sources known to drive plot-scale snowmelt variability. Finally, the timing of the melt season, defined by the period of time between peak SWE and snow disappearance, dictates the availability of incident solar radiation and thus strongly influences the SWE ablation rates. For example, the year with the latest peak SWE date (May 2, 2010) and latest mean snow disappearance date exhibited the shortest melt season duration (see Table 2). In contrast, 2008 was the clearest melt season on record but, with a peak SWE date of March 23, recorded the longest melt season duration of the three years despite recording only ~ 74% of the 2010 peak SWE. Other inter-annual meteorological differences during the melt season such as air temperature, snowfall, humidity, wind, cloud cover and rain-on-snow events would also be expected to result in inter-annual differences in seasonal SWE ablation rates.

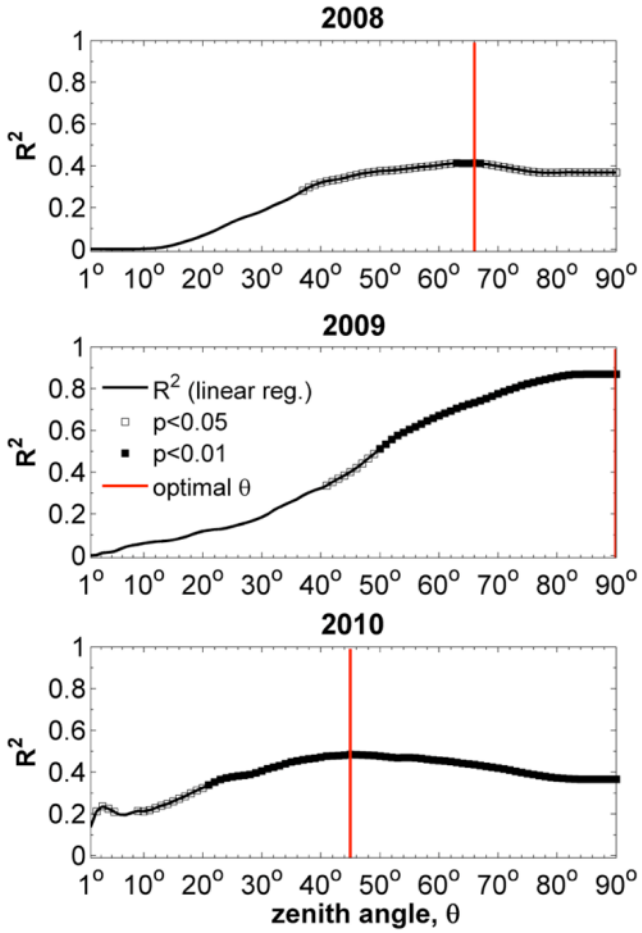

Figure 2.10. Coefficient of determination and p-values from linear regression between seasonal SWE ablation (ΔSWE) measured at operational depth sensors for water years 2008, 2009, and 2010, and sky view factor (SVF_θ) at corresponding sensor locations computed by integrating canopy openness from specified zenith angles (1° - 90°) to nadir (0°). For each year, the vertical red line indicates the zenith angle that maximizes R^2 and minimizes the p-value.

Numerous sources of uncertainty could potentially complicate the statistical relationships between seasonal SWE ablation rates and the metrics direct beam irradiance and SVF_θ. How these error sources influence the interpreted results depend on the type and degree of uncertainty and the methods available to minimize the errors. For example, the geo-reference errors in hemispherical photos can be minimized by following documented methods (e.g. Frazer et al., 1999; Hardy et al., 2004). Such errors would be expected to be small and relatively random in nature. Conversely, errors associated with the use of radiation measurements made in an alpine

area 8 km from the study site to represent above-canopy radiation at lower elevations may have greater implications on the results. For example, a three-year comparison of $R_{s\downarrow}$ measured at Topaz Lake and a station 340 m lower in elevation than the study area yielded a correlation coefficient of 0.93. Despite the relatively high long-term correlation, the correlation was lower during cloudy periods, indicating that the alpine region experienced more cloud cover than the lower elevations.

The use of these data to represent above-canopy global solar radiation at the lower elevations could introduce a negative bias in the radiation data, particularly during cloudy periods. This bias could potentially influence inter-annual comparisons and interpretations of the results. A bias would be expected to manifest largely during the cloudiest season (e.g. 2009) and would decrease the significance of the linear regression between ablation rates and direct beam solar irradiance for this year. A simple test for this radiative bias would be to examine the zenith angle that resulted in the best linear fit between seasonal SWE ablation rates and SVF_{θ}. A negative radiation bias (i.e. simulating cloudy conditions when it is actually clear) would cause a decrease in the 'optimal' zenith angle, similar to what is observed during years with less cloud cover (e.g. 2008 and 2010). The optimal zenith angle of 90° during the 2009 melt season suggests that this potential radiation bias was negligible (i.e. measured cloud cover in the alpine similarly impacted the Wolverton basin).

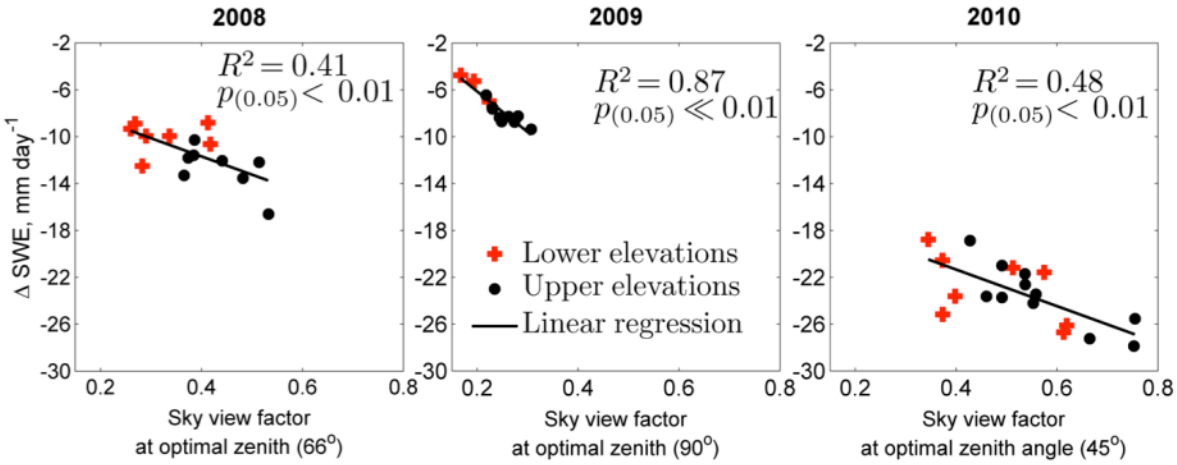

Figure 2.11. Linear regression trends between seasonal SWE ablation rates shown in Figure 2.9 and the corresponding measured SVF_θ at the optimal zenith angles for years 2008 (n=15), 2009 (n=12), and 2010 (n=19) as indicated by the red lines in Figure 2.10.

The strength of the statistical relationship between sky view (a measure of canopy openness) and observed ablation was found to be sensitive to the concentric area of the hemispherical sky view used to evaluate SVF_θ. The findings support results of *López-Moreno and Latron* (2008), in which a sensitivity between SWE, time of year, and the specified range of zenith angles used to compute SVF_θ was documented. Evaluation of the zenith angle that when used to compute SVF_θ explains the most variability in ablation rates across all snow depth sensor locations may provide insight into the source of the governing energy fluxes. For example, the high optimal zenith angle of 90° predicted during the cloudiest melt season suggests the dominance of energy sources derived from all hemispherical directions, including diffuse radiation and atmospheric and terrestrial longwave radiation known to be dominant energy fluxes during cloudy conditions. The reduced optimal zenith angles for years with less cloud cover and / or a later melt season imply a stronger influence of the solar direct beam with respect to the sub-canopy energy balance. For example, the daytime average and average daily maximum solar zenith angles during the melt season were 53° and 25° in 2008 (March 23 – May 22) and were

50° and 16° in 2010 (May 2 – June 16). The zenith angle at which SVF_θ explained the most variability in ablation rates of 45° in 2010 (8 cloudy days and late melt season) is close to the 50° daily average solar zenith angle for this melt season. In 2008 (four cloudy days and early melt season), the optimal SVF_θ zenith angle of 66° is nearer to the horizon than the 53° daily average solar zenith angle. The differences suggest that the variability of ablation rates during the earlier melt season (i.e. 2008) may be less impacted by direct beam solar irradiance than the melt season that occurred later (i.e. 2010) despite the latter season experiencing more cloud cover. The results indicate that the ability of the individual metrics to explain observed variability in SWE ablation rates is related to seasonal meteorology (i.e. both cloud cover and timing and duration of the melt season). Combined, the two metrics studied here (sub-canopy direct beam irradiance and SVF_θ) may be used to explain much of the observed plot-scale variability in SWE ablation at the finer time scales relevant to snow and hydrological model applications.

Land surface and hydrological models typically use spatially aggregated (i.e. bulk) representations of complex, three-dimensional (3-D) canopy structure to represent the numerous mechanisms known to cause spatiotemporal variability in SWE. Satellite-derived estimates of canopy density and *LAI'* are two bulk forest metrics commonly used to scale above-canopy fluxes to the sub-canopy surface. Despite well-documented relationships between sub-canopy fluxes and areal-averaged *LAI'* and canopy density, these bulk metrics often lack the level of detail necessary to fully explain sub-canopy snow dynamics (Varhola et al., 2010b). *Essery et al.* (2008b) suggest that a more explicit characterization of canopy structure is needed to resolve the distribution of sub-canopy energetics and snow cover depletion. Detailed atmosphere - canopy radiative transfer models have proven accurate in the simulation of forest light environments for

the estimation of photosynthesis and carbon sequestration (Kobayashi and Iwabuchi, 2008), but the distributed application of such techniques is generally limited by computational expense and data requirements. An effective compromise in detailed canopy representation may split the difference between bulk forest metrics such as *LAI'* or canopy density and 3-D canopy structure data required by multispectral radiative transfer models.

The metrics SVF_θ and direct beam irradiance could be combined with other variables such as canopy parameters, slope, aspect or elevation to further explain variability of observed ablation rates. However, the relationships and metrics explored in this study have more global implications for the improvement of land surface and hydrologic models in snow-covered forests. For example, direct beam canopy transmissivity could be incorporated as a time-variant model input rather than using bulk LAI' and extinction parameter values in a Beer's-type exponential reduction of above-canopy direct beam solar radiation. Similarly, SVF_θ determined at optimal zenith angles defining sky / canopy regions that most influence particular energy fluxes could be used to simulate energy fluxes that are more omnidirectional than the solar direct beam. For example, SVF_θ determined from hemispherical photographs could be used to estimate sub-canopy longwave irradiance during cloudy periods. However, during clear sky conditions the added contribution of longwave radiation by sunlit canopy elements (e.g. Pomeroy et al., 2009) introduces a third dimension to the problem that cannot be fully addressed with a single two-dimensional photograph. Increasingly available light detection and ranging (LiDAR) data provide a means to obtain these and other canopy structure metrics for future basin-scale hydrological applications.

Terrestrial LiDAR techniques have been used to estimate *directional SVF* (e.g. Côté et

al., 2009; Danson et al., 2007) but, like hemispherical photography, the technique is limited in its application at hydrologically relevant scales (i.e. catchment level). Toward bridging this scale gap, airborne scanning LiDAR systems offer an innovative alternative (van Leeuwen and Nieuwenhuis, 2010; Varhola et al., 2010a) to other indirect methods in that they capture the general spatial arrangement and structure of vegetation over large areas. Work by *Essery et al.* (2008a) to derive a viewshed of surrounding forest vegetation from an orthophoto and LiDAR data shows promise for subsequent distributed applications of the current work. Future efforts will explore the utility of detailed canopy metrics to improve the representation of surface - atmosphere interactions in physically based snow, hydrological, and ecological models, including extending the presented methods to estimate the sub-canopy thermal radiative environment. Efforts will include the use of LiDAR data to map the most physically meaningful, detailed canopy metrics over large areas for distributed model application.

2.4 Conclusions

Sub-canopy cumulative seasonal direct beam solar irradiance derived from above-canopy measurements and hemispherical photography explained the most variability in snow ablation rates during the least cloudy melt season (58%, $p_{(0.05)}<<0.01$; 2008; 4 cloudy days, 365 MJ m^{-2} direct irradiance), less for the snowmelt season with intermediate cloud cover (23%, $p_{(0.05)}<0.05$; 2010; 8 cloudy days, 304 MJ m^{-2} direct irradiance), and the least during the cloudiest melt season of the study (29%, $p_{(0.05)}> 0.05$; 2009; 23 cloudy days, 274 MJ m^{-2} direct irradiance). Conversely, sky view factor (SVF_θ) explained the most variability in snow ablation rates under cloudier conditions (i.e. 87% in 2009, $p_{(0.05)}<<0.01$) and the relationships between SVF_θ and ablation rates

were stronger when developed over the entire hemisphere (i.e. SVF_{90°). Combined, the two metrics studied here (sub-canopy direct beam irradiance and SVF_θ) may be used to explain much of the observed plot-scale variability in SWE ablation at finer time scales relevant to physically based snow and hydrological model applications.

Chapter 3. Improved snowmelt simulations with a canopy model forced with photo-derived direct beam canopy transmissivity

This study evaluates snowmelt estimates from a canopy model coupled to a finite-element snowmelt model. Three years of sub-canopy snow observations from 24 locations spanning a range of terrain and forest structure provide the basis for the evaluation. The methods examine whether model skill is gained from an increased level of detail in the canopy structure information provided to the canopy module, with a focus on the treatment of direct beam canopy transmissivity. The following questions are addressed: (1) 'How do various methods of obtaining bulk canopy metrics affect snowmelt model accuracy?' and (2) 'Does an explicit treatment of direct beam canopy transmissivity improve snowmelt model accuracy?'

The next section describes the background and motivating questions. Section 3.2 provides additional details of the study area, instrumentation, canopy structure and the regional hydrometeorological data as they differ from those presented in Chapter 2. Section 3.3 presents the snow model details as well as the simulation methodology. Results, discussion and conclusions are described in Sections 3.4, 3.5, and 3.6, respectively. A summary of the canopy

model is provided in Appendix A.

3.1 Background

Canopy models vary in their representation of radiative transfer (RT) from simple bulk approximations to complex treatments of the effects of individual canopy elements on attenuation, reflection and transmission of radiation. Many of the simpler models employ a one-dimensional "big-leaf" canopy representation, which is most applicable over flat, homogeneous terrain (Baldocchi et al., 1987). In big-leaf models, canopy RT is treated with a two-stream approximation (Dickinson, 1983) and above-canopy radiation is attenuated by a two-parameter application of the Beer-Lambert law (Monsi and Saeki, 1953), which assumes the exponential reduction of radiation through a homogeneous medium (Shugart, 1984). The application of the Beer-Lambert law to above-canopy radiation is generally inadequate to resolve sub-canopy irradiance at sub-daily time scales, largely as a result of discontinuous canopy gaps (Reifsnyder et al., 1971). Exponential attenuation has, however, been shown to adequately estimate the net sub-canopy irradiance over longer periods (e.g. Larsen and Kershaw, 1996; Reifsnyder et al., 1971) provided that the parameters are derived from field measurements (Bréda, 2003). Separate exponential attenuation coefficients for diffuse and direct radiation has been shown to partially explain time-varying canopy transmission as a consequence of snow interception and cloud cover (Stähli et al., 2009). In big-leaf models, canopy gaps are accounted for with a canopy openness fraction and the remaining fraction of vegetation is assumed to be randomly distributed (Nijssen and Lettenmaier, 1999). The assumptions inherent to canopy RT models parameterized with bulk canopy metrics make them difficult to apply to point-scale locations beneath a

discontinuous forest canopy.

Semi-empirical studies conducted with physically realistic snowmelt models have reported that canopy height and stand density, two common bulk forest metrics, exert first-order control on sub-canopy cumulative shortwave irradiance and simulated snowmelt rates (e.g. Davis et al., 1997). More recent studies have used airborne scanning light detection and ranging (LiDAR) to represent the spatial arrangement of forest canopies (e.g. Essery et al., 2008a; van Leeuwen and Nieuwenhuis, 2010; Varhola et al., 2010a). As high-resolution vegetation data become more available, the use of detailed canopy metrics to improve snowmelt model representation of snow - atmosphere interactions must be explored.

As mentioned in Chapter 1, physically based snowmelt models are well suited to evaluate the complex linkages between meteorology, forest cover, snow accumulation and melt, and the basin-scale water balance (e.g. Lehning et al., 2006; Pomeroy et al., 2007). The ability of a physically based snow – canopy model to simulate these processes is limited, in part, by the difficulty of obtaining detailed canopy structure information (Tribbeck et al., 2004). Additionally, the error associated with validating simulated snowmelt rates with in-situ measurements is large (Nijssen and Lettenmaier, 1999). This is particularly true when canopy models are parameterized by bulk canopy metrics. This study demonstrates many of these limitations resulting from scale issues.

Plot-scale variability in the timing of melt onset and snowmelt duration influences the distribution of soil moisture (Bales et al., 2011; Molotch et al., 2009), infiltration, groundwater recharge, and streamflow (Seyfried and Wilcox, 1995). Detailed simulations of plot-scale variability could improve the representation of sub-grid variability in modeled

hydrometeorological states and fluxes (e.g. Claussen, 1991; Luce et al., 1999) and help to resolve related scaling issues (e.g. Blöschl, 1999). Improved simulations of snow processes at the plot-scale could also inform the representativeness of satellite-derived snow covered area (SCA) to actual sub-canopy SCA (e.g. Hall et al., 1998; Klein et al., 1998; Molotch and Margulis, 2008).

More detailed canopy representation in model structure and/or model parameterization may improve the accuracy of physical snowmelt models. For example, upward-looking hemispherical photography is an inexpensive method of estimating forest canopy structure and the likelihood that direct beam solar radiation is transmitted through the canopy (Hardy et al., 2004). *Hardy et al.* (2004) improved simulated snowmelt rates using a photo-derived seasonal mean canopy transmissivity value compared to simulations with a bulk (i.e. Beer-Lambert type) reduction of above-canopy solar radiation. However, diurnal and seasonal variability in solar magnitude and the timing of the sun's track across discontinuous canopy gaps limit the utility of seasonal mean transmissivity estimates. A measure of direct beam canopy transmissivity at a temporal resolution that adequately captures the diurnal and seasonal variability of sub-canopy shortwave irradiance may improve snowmelt simulations. To our knowledge, no study has applied direct beam canopy transmissivity as a time-variant input to a physically based snow model.

3.2 Experimental design and methods

The one-dimensional soil – snow – vegetation model SNOWPACK (Bartelt and Lehning, 2002; Lehning et al., 2002a; Lehning et al., 2002b) was forced with observations of above-canopy meteorology to simulate sub-canopy snowpack dynamics. The model was initialized at

locations of 24 ultrasonic snow depth sensors for water years 2008, 2009 and 2010; a total of 72 sensor-years. For each sensor-year, three distinct scenarios were evaluated for their effect on model accuracy. The three scenarios specified different levels of canopy structure detail to the big-leaf canopy module: **(i) Scenario *N*** is the nominal scenario designed to represent a modeling case where no ground-based observations of canopy structure are available, necessitating the use of gridded satellite data or a land surface look-up table; this approach is commonly applied in distributed modeling studies (e.g. Wigmosta et al., 1994). The SNOWPACK canopy model parameters *canopy openness* and *effective leaf area index* (LAI') were derived from satellite data at 30 m resolution and estimated from literature-based sources, respectively, as described in Section 2.2. The canopy parameters were chosen to be as representative as possible of the canopy conditions at snow depth sensor locations where models were initialized. **(ii) Scenario *NP*** is the 'nominal-photo' case in which upward-looking hemispherical canopy photos were taken at snow depth sensor locations where models were initialized. The photos were used to derive the SNOWPACK canopy model parameters *canopy openness* and LAI' (see Section 2.2); this approach is common in point-scale modeling studies (e.g. Rutter et al., 2009) and is expected to yield more accurate estimates of these bulk parameters compared to Scenario *N*; and **(iii) Scenario NP_{DBT}** builds upon the level of photo-derived canopy structure detail provided in the *NP* scenario with a modification to the structure of the canopy model that permits an explicit, time-variant treatment of solar direct beam canopy transmissivity (DBT) derived from the same photos (rather than a bulk representation) as described in Section 2.3. Three years of data from repeated snow surveys and a network of sub-canopy snow depth and soil moisture sensors were used to evaluate model performance.

3.2.1 Site description, instrumentation and hydrometeorology

Work was conducted in the 7.22 km^2 Wolverton basin of Sequoia National Park on the western slope of the southern Sierra Nevada, CA, U.S.A. (36.59ºN, 118.717ºW) (Figure 3.1). *Musselman et al.* (2012) provides a description of the basin and the four instrumented sites stratified across the basin's range of elevation, aspect, and canopy cover (Figure 3.1, Tables 1-2).

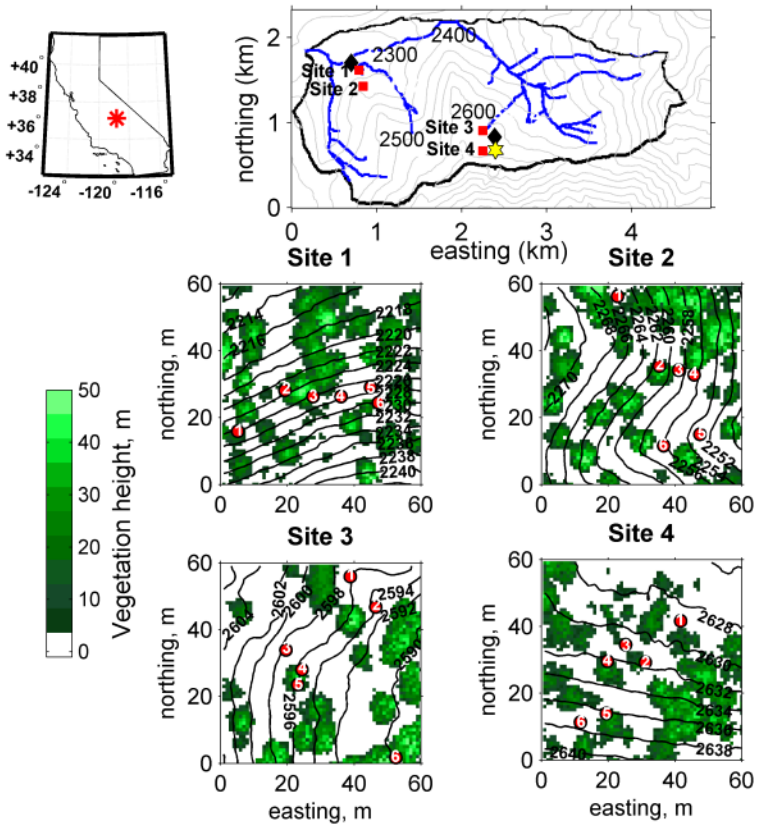

Figure 3.1. The Wolverton basin and its four instrumented research sites (red squares) in the southern Sierra Nevada, CA (top). The location of two meteorological towers (black diamonds) and an upper elevation snow course (yellow asterisk) are indicated. Elevation contours and lidar-derived vegetation heights within 60 m x 60 m domains centered on each of the four sites are included. Red circles and reference numbers mark the locations of the six ultrasonic snow depth sensors at each site.

At each site, six ultrasonic snow depth sensors (Judd Communications) recorded hourly snow depth (Figure 3.2). The data were processed to remove outliers and fill gaps following *Lehning et al.* (2002a). Volumetric soil water content (VWC; Campbell Scientific CS 616

sensors) and soil temperature sensors (T-107 sensors) were installed horizontally in the soil column beneath three of the six snow depth sensors at each site, for a total of 12 instrumented soil profiles. Only VWC data from -10 cm soil depths were used in this study as the primary interest was in meltwater leaving the base of the snowpack (Figure 3.2). The presented VWC data were uncalibrated and as such were only used to evaluate the timing of meltwater pulses in the soil. At each site, hourly soil temperature data were obtained at -10 cm, -30 cm, and -60 cm soil depths beneath three of the six snow depth sensors. Spatial averages of the three soil profiles provided hourly estimates of the site-specific soil temperature profile, which was assumed to be representative of the soil temperature beneath all six snow depth sensors at the respective sites.

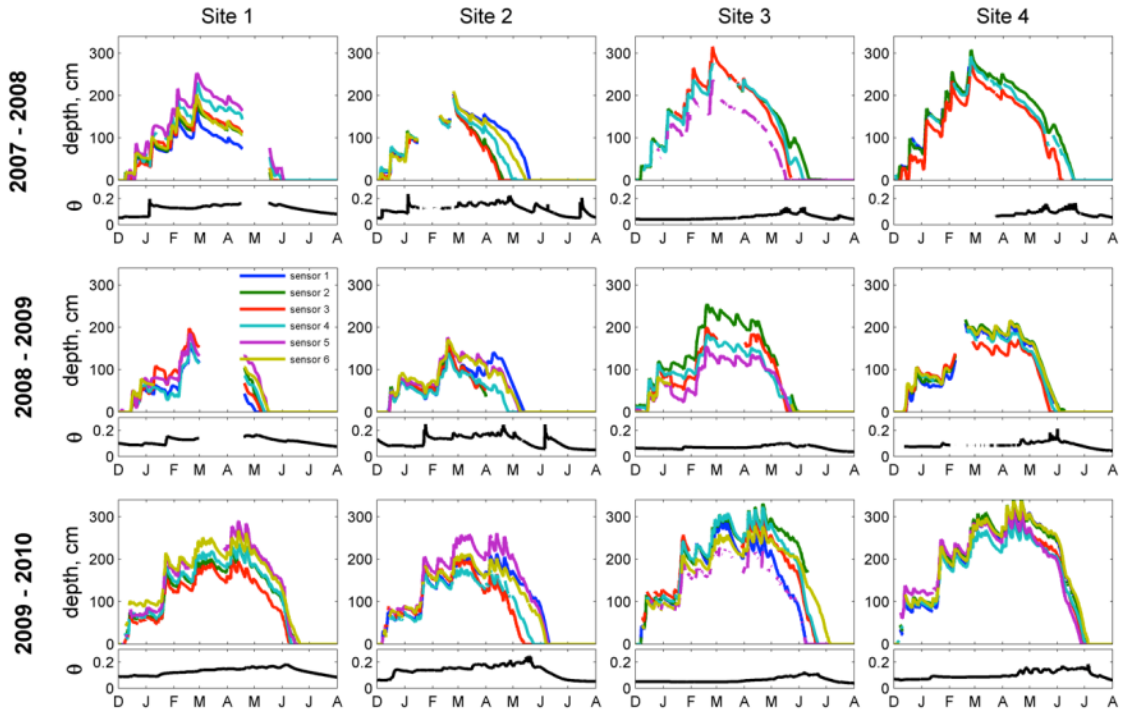

Figure 3.2. Observations of snow depth (colored lines) from six ultrasonic depth sensors and volumetric soil water content (black line) measured at a soil depth of -10 cm at each of the four research sites for water years 2008, 2009, and 2010.

Table 3.1. Terrain variables provided to the models initialized at locations of the six ultrasonic snow depth sensors at each of the four research sites.

	SITE 1						SITE 2					
Sensor:	1	2	3	4	5	6	1	2	3	4	5	6
Elevation*, m	2253	"	"	"	"	"	2300	"	"	"	"	"
Aspect, degrees from north	355	355	355	355	355	355	45	120	120	120	80	60
Slope, degrees	22	22	22	22	22	22	10	15	15	15	15	15

	SITE 3						SITE 4					
Sensor:	1	2	3	4	5	6	1	2	3	4	5	6
Elevation*, m	2620	"	"	"	"	"	2665	"	"	"	"	"
Aspect, degrees from north	40	70	95	95	95	NA	10	10	10	10	10	10
Slope, degrees	10	10	10	8	6	0	8	10	10	10	12	17

Table 3.2. Canopy variables provided to the models initialized at locations of the six ultrasonic snow depth sensors at each of the four research sites.

	SITE 1						**SITE 2**					
Sensor:	**1**	**2**	**3**	**4**	**5**	**6**	**1**	**2**	**3**	**4**	**5**	**6**
Canopy openness* (%)	24	26	26	26	26	26	34	34	45	45	48	48
LAI ' $m^2 m^{-2}$	3.9	2.87	2.91	2.2	1.06	1.14	4.1	1.44	1.68	2.46	1.44	2.03
SVF_{65° (%)	28	27	26	29	43	42	34	39	37	29	41	39

	SITE 3						**SITE 4**					
Sensor:	**1**	**2**	**3**	**4**	**5**	**6**	**1**	**2**	**3**	**4**	**5**	**6**
Canopy openness* (%)	71	71	63	63	36	36	80	42	33	42	33	34
LAI ' $m^2 m^{-2}$	3.43	2.63	1.24	1.53	2.13	3.28	2.22	2.28	2.16	2.42	2.3	1.9
SVF_{65° (%)	64	52	54	49	37	35	42	45	38	39	36	41

* Canopy openness was determined from Landsat-derived NLCD, 2001 canopy density.
** Sky view factor (SVF) was determined from hemispherical canopy photos as the weighted average of all photo pixels from 65° zenith to nadir (0° zenith) (i.e. SVF_{65°).

Two seven-meter meteorological towers, each located near Sites 1 and 2 at 2232 m above sea level (asl) and Sites 3 and 4 at 2642 m asl, provided hourly observations of air temperature (Figure 3.3a), relative humidity (Figure 3.3b), and wind speed (Figure 3.3c) at an average sensor height of six meters. The towers are located in large canopy gaps and the collected data were assumed to be representative of above-canopy conditions (Figure 3.1).

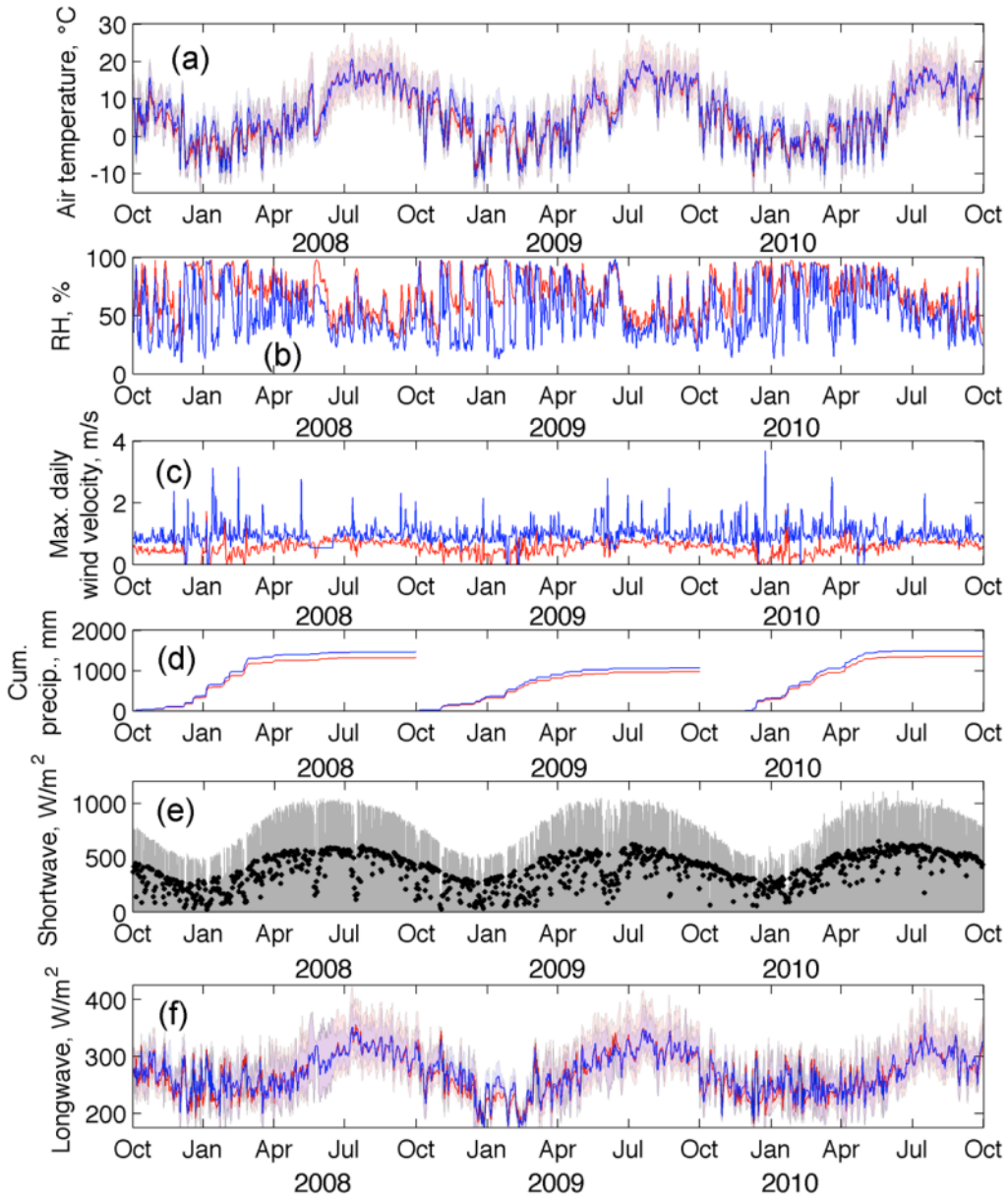

Figure 3.3. Meteorological variables representing conditions at the lower (red) and upper (blue) elevation research sites including: (a) daily mean (line) and range (shading) of air temperature, (b) daily mean relative humidity, (c) maximum daily wind velocity, (d) cumulative annual precipitation for each water year (1 October to 30 September), (e) hourly (gray) and daytime mean (points) shortwave radiation from the Topaz Lake meteorological station, and (f) daily mean (line) and range (shading) of longwave radiation.

Snow density data were obtained from monthly snow pit measurements made at the instrument sites and approximately monthly California Cooperative Snow Survey (CCSS) measurements (Table 3). Snow pit density measurements, made in duplicate profiles with 1000

cm^3 cutters, were assumed representative of the site-average snow density. CCSS snow course density data represent the average of Federal snow tube measurements made along multiple transects near Sites 3 and 4 (Figure 3.1). Observations from four (2008), six (2009) and four (2010) snow density surveys were used to estimate the SWE at individual snow depth sensors on each survey date (Table 3). The SWE at each sensor location was obtained using the site-average density and the sensor-specific depth. Surveys conducted before and after the date of maximum annual SWE were considered to represent the accumulation- and melt-seasons, respectively (see Table 3).

Precipitation was recorded at two additional meteorological stations. The Lower Kaweah station (36.56611ºN, 118.7778ºW, 1890 m asl), operated by the National Park Service, includes a shielded, heated tipping bucket precipitation gauge. The station is located five km SW of the Wolverton basin and ~ 340 m lower in elevation. The Giant Forest station (36.562ºN, 118.765ºW, 2027 m asl), operated by the US Army Corps of Engineers, includes a shielded storage precipitation gauge. The Giant Forest gauge is located 4.6 km SSW of the Wolverton basin and ~ 205 m lower in elevation. Data from the two precipitation gauges were merged in an effort to fill data gaps. Catch efficiency of precipitation gauges depends on the gauge and shield design, the wind speed, and the precipitation type (rain or snow) (Groisman and Easterling, 1994). The catch efficiency of the two gauges is assumed to be equal and is specified according to *Groisman and Easterling* (1994) as 0.95 for rain and 0.4 for snow, which is near the lower end of the reported efficiency range but higher than used in other studies (e.g. Pierce et al., 2008). Air temperature is used as a simple proxy for precipitation type such that a catch efficiency of 0.4 is used at temperatures ≤ 1°C and 0.95 is specified at temperatures > 1°C. The corrected gauge

measurements are then scaled to the respective elevations of the four Wolverton basin research sites with seasonally dependent orographic precipitation adjustment factors derived in *Thornton et al.* (1997) as presented in *Liston and Elder* (2006a). Cumulative precipitation data for the three water years (Oct. 1 – Sep. 30, 2008 - 2010) at the two meteorological stations are shown in Figure 3d.

Table 3.3. Dates, locations, and results of snow density surveys in the Wolverton basin for three snow seasons. Average snow densities at lower (Sites 1 and 2) and upper (Sites 3 and 4) elevations are used with the snow depth sensor measurements on the day of each survey to estimate SWE (mean and standard deviation) at each site. Shading indicates survey dates considered to represent the melt-season.

Survey Date	Survey Location(s)	Density, kg m^{-3}		SWE: site mean ± st. dev., mm			
		Lower elevations	Upper elevations	Site 1	Site 2	Site 3	Site 4
12 Jan., 2008	Sites 1,3,4	336	361	319±69$^{(6)}$	320±10$^{(5)}$	521±45$^{(3)}$	523±48$^{(4)}$
17 Feb., 2008	Sites 1,3	349	381	469±88$^{(6)}$	460±15$^{(5)}$	744±117$^{(3)}$	755±52$^{(4)}$
23 Mar., 2008	Sites 1,3	391	441	560±129$^{(6)}$	470±92$^{(5)}$	931±142$^{(4)}$	988±83$^{(3)}$
27 Apr., 2008	Sites 1,2,3	443	440	$^{(0)}$	168±208$^{(5)}$	674±158$^{(4)}$	792±83$^{(3)}$
25 Jan., 2009	CCS	330*	330	187±75$^{(4)}$	161±26$^{(6)}$	261±110$^{(4)}$	286±25$^{(4)}$
14 Feb., 2009	Sites 1,2,3	254	271	334±49$^{(4)}$	290±31$^{(6)}$	405±108$^{(4)}$	$^{(0)}$
22 Feb., 2009	CCS	360*	360	553±64$^{(4)}$	481±58$^{(6)}$	651±156$^{(4)}$	701±20$^{(4)}$
21 Mar., 2009	Sites 1,3	314	354	$^{(0)}$	263±83$^{(6)}$	550±173$^{(3)}$	592±63$^{(5)}$
2 Apr., 2009	CCS	440*	440	$^{(0)}$	395±105$^{(4)}$	669±159$^{(4)}$	747±84$^{(5)}$
25 Apr., 2009	Sites 1,3	425	411	291±144$^{(6)}$	213±158$^{(4)}$	509±123$^{(4)}$	652±50$^{(5)}$
25 Jan., 2010	CCS	270*	270	462±62$^{(5)}$	456±43$^{(5)}$	572±59$^{(6)}$	582±34$^{(5)}$
1 Mar., 2010	CCS	340*	340	672±96$^{(4)}$	673±94$^{(5)}$	873±99$^{(5)}$	916±48$^{(5)}$
29 Mar., 2010	CCS	450*	450	832±131$^{(5)}$	697±134$^{(5)}$	969±128$^{(6)}$	1092±71$^{(5)}$
2 May, 2010	CCS	500*	500	948±151$^{(5)}$	687±257$^{(5)}$	1253±156$^{(5)}$	1395±108$^{(6)}$

CCS: California Cooperative Snow Survey location (near Sites 3 and 4)
*: Density only measured at upper elevations and assumed representative of lower elevation sites.
$^{(\#)}$: Number of operational snow depth sensors at a given site on the day of a snow density survey.

While the two Wolverton meteorological stations were located in forest clearings, measurements of incoming shortwave ($R_{S\downarrow}$) and longwave ($R_{L\downarrow}$) radiation were affected by tall vegetation surrounding the stations. Instead, $R_{S\downarrow}$ data used in this study were measured at a

station 8 km ENE of the Wolverton basin at Topaz Lake (3220 m asl), which is located above timberline and is minimally shadowed by local terrain. In a previous study, the $R_{S\downarrow}$ data from Topaz Lake were found to adequately represent the regional above-canopy shortwave field (see Musselman et al., 2012) and were used without correction in the current study to represent $R_{S\downarrow}$ in the Wolverton basin (Figure 3e). $R_{L\downarrow}$ data were obtained from the Emerald Lake meteorological station, located five km ENE of the Wolverton basin at elevation 2816 m asl. The temperature dependence of $R_{L\downarrow}$ and differences in temperature between the Wolverton study sites and Emerald Lake must be considered. Therefore, the incoming atmospheric longwave radiation expected under clear sky conditions ($R_{L\downarrow_{clear}}$) was estimated for each of the Emerald Lake and the two Wolverton meteorological stations. The fluxes were estimated from local air temperature and relative humidity measurements as in *Satterlund et al.* (1979). The enhancement of longwave radiation by cloud cover was accounted for by computing the maximum of the hourly measured and clear-sky estimated fluxes at Emerald Lake. The fractional increase between hourly $R_{L\downarrow}$ and $R_{L\downarrow_{clear}}$ is represented as:

$$f_L = \max\left(1, \frac{R_{L\downarrow}}{R_{L\downarrow_{clear}}}\right) \qquad (1)$$

The time-variant fraction f_L was used to adjust the hourly clear-sky estimates computed from measurements made at the two meteorological stations in the Wolverton basin, $R_{L\downarrow_{clear,Wolv}}$, as:

$$R_{L\downarrow_{Wolv}} = f_L R_{L\downarrow_{clear,Wolv}} \qquad (2)$$

The hourly $R_{L\downarrow_{Wolv}}$ data for the lower and upper elevation Wolverton meteorological stations are

assumed to be representative of above-canopy longwave fluxes at Sites 1 and 2, and Sites 3 and 4, respectively (Figures 1 and 3f).

3.2.2 Canopy structure metrics

Two levels of canopy structure detail are presented. The first, used in Scenario *N*, is a coarse approximation of canopy openness and effective leaf area index (LAI') obtained from remote sensing and literature, respectively, with no in-situ canopy structure knowledge. Remotely sensed bulk canopy openness, defined as (*1 – canopy density*), was obtained from the National Land Cover Database (NLCD, 2001), which is a 30 m resolution product of Landsat Enhanced Thematic Mapper (ETM+) satellite data (Homer et al., 2004). The coarse approximation of LAI' was specified as a constant value for all point locations in the basin and was estimated from direct measurements of one-sided leaf surface area made in the greater Wolverton region by *Spanner et al.* (1990). However, direct LAI measurements are typically 25% to 50% higher than those obtained by indirect optical methods (see thorough review by Bréda, 2003 and references therein) such as hemispherical photography or the LAI-2000 Plant Canopy Analyzer (Li-COR, Nebraska, USA). Strictly, optical methods measure the plant area index, which is a more accurate metric of how all canopy elements, including wood area, combine to influence RT. The differences between the values provided by direct and indirect methods are a product of non-random clumping of canopy elements at a variety of scales as well as the ratio of woody area to leaf area; all metrics that vary significantly within a single stand and are typically estimated with a high degree of uncertainty (Bréda, 2003). The average direct measurement of LAI reported by *Spanner et al.* (1990) of ~ 7.5 m^2 m^{-2} was simply reduced by 30% to 5.25 m^2 m^{-2} to be consistent with the indirect hemispherical photo measurement technique described below (hereafter, the

optical estimate of effective leaf area index is referred to as LAI' to be consistent with the literature).

The second and more detailed level of canopy structure, used in Scenarios *NP* and NP_{DBT}, was measured in-situ by upward-looking hemispherical photographs taken directly beneath each of the 24 snow depth sensors. Figure 4a provides an example of a hemispherical photo taken at Site 3 beneath depth sensor 1. Readers are referred to *Musselman et al.* (2012) for a description of the photo acquisition and processing. LAI' was estimated from photos following *Norman and Campbell* (1989) and accounting for a sloped surface as *Schleppi et al.* (2007) to range from 1.20 to 4.88 m^2 m^{-2} with an average of 2.72 m^2 m^{-2} (Table 2). An estimation of canopy openness in all azimuth directions as viewed by a hemispherical photo requires a zenith angle (θ) be specified to compute the sky view factor (SVF_θ) as the hemispherical weighted sum of the fraction of sky pixels to total pixels from the specified zenith angle to nadir (Figure 4c). As terrain tended to enter the images at θ values greater than ~ 70°, a zenith angle of 65° was chosen to compute SVF_θ from all photos. It should be noted that when iteratively computed at one-degree θ angles from 1° to 90° for nearly 90 photos taken at the field site, in no case did SVF_θ *increase* when computed with θ angles greater than 65° (not shown). Canopy openness at 24 snow depth sensor locations was obtained by computing SVF_θ from a zenith angle of 65° to nadir (see Table 2).

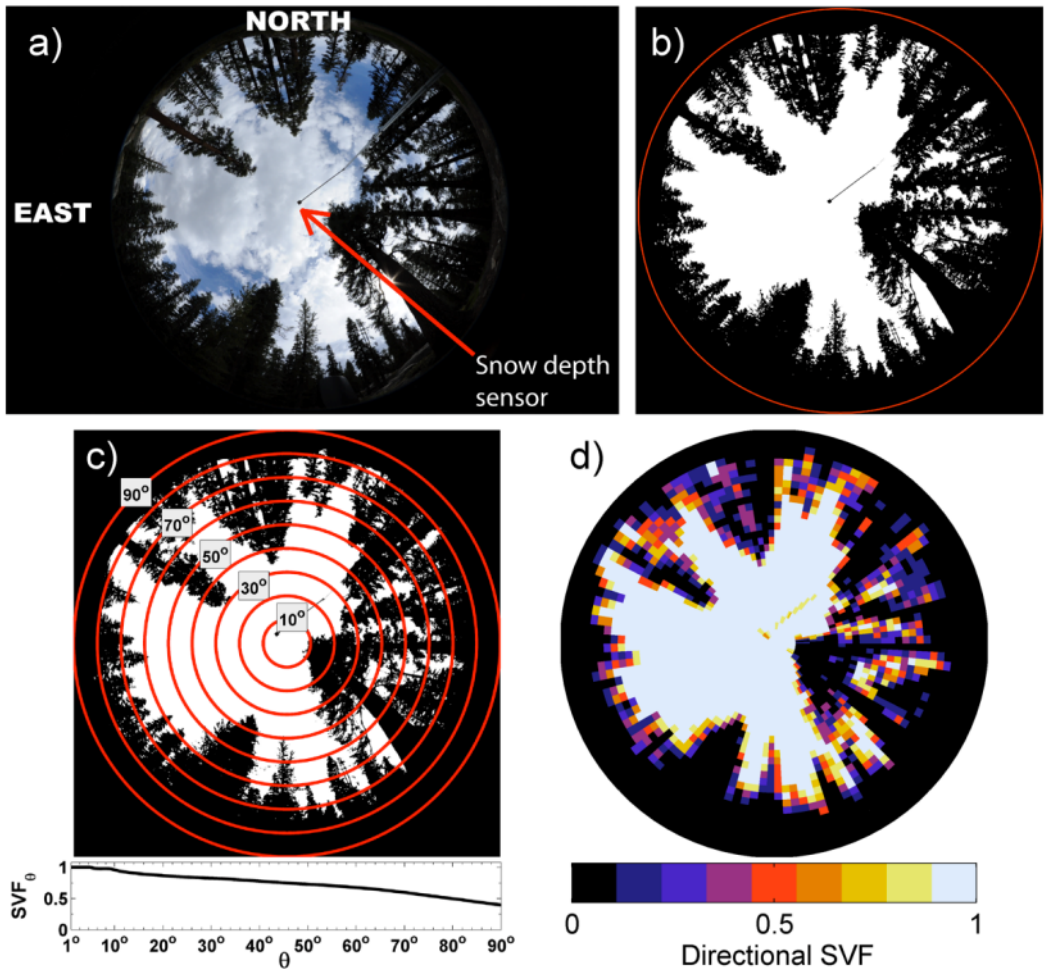

Figure 3.4. Example of a hemispherical canopy photo taken beneath snow depth sensor 1 at site 3. The (a) raw, georeferenced color photo is (b) processed to produce a binary representation of sky and non-sky elements, and analyzed to evaluate canopy openness metrics (c) SVF_θ across the full range of zenith angles at one-degree increments and (d) *directional SVF* at 3° angular resolution, or a discretization of 120 azimuth and 30 zenith solid angles.

3.2.3 Direct beam canopy transmissivity

An explicit evaluation of the probability of solar beam transmission through the forest canopy at a given time and at the location of a hemispherical photograph required that photos be analyzed in discrete solid angles, or sky regions, specified by both azimuth and zenith angular increments. Hemispherical images taken at each of the 24 depth sensor locations were divided

into 120 azimuth and 30 zenith regions and the *directional SVF* was computed for each sky region (see example in Figure 3.4d). Methods of *Musselman et al.* (2012) were used to estimate the direct beam canopy transmissivity by sampling the directional *SVF* in the sky region corresponding to the solar position. Direct beam canopy transmissivity for the three water years at each photo location was estimated at one-minute instantaneous steps and averaged to ten-minute estimates. Figure 3.5a illustrates the ten-minute canopy transmissivity at Site 3, depth sensor 1, estimated during daylight hours between the winter and summer solstices of water year 2008. Examples of direct beam canopy transmissivity at the same location but averaged to 60-minute, 30-minute and one-minute temporal resolutions are provided in Figures 5b-d.

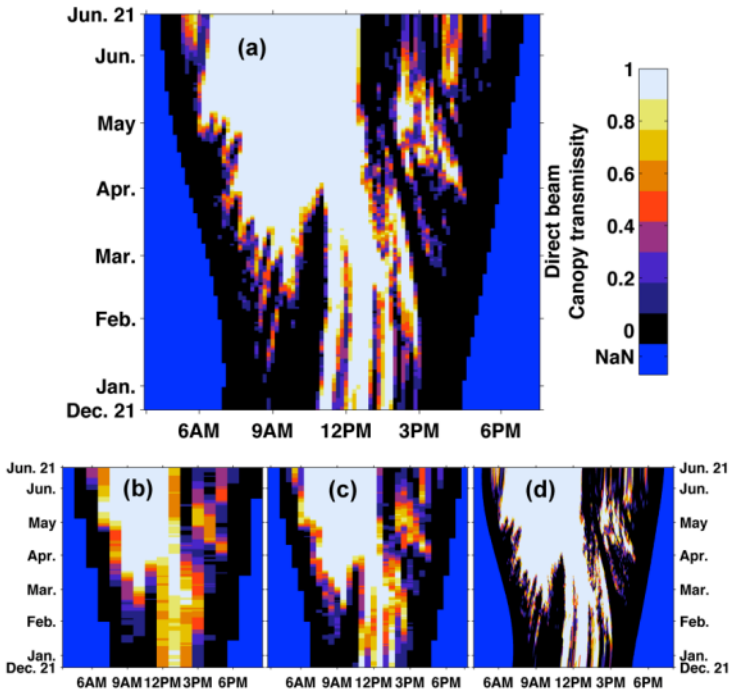

Figure 3.5. Direct beam canopy transmissivity for daylight hours of all days (vertical axes) between the winter and summer solstices at the location of Site 3, sensor 1 determined from hemispherical photo by sampling the directional SVF in the sky direction defined by the solar coordinates at (a) 10-minute, (b) 60-minute, and (c) 30-minute temporal aggregation and (d) one-minute instantaneous values. Temporal resolution at the diurnal scale describes the resolution of the horizontal axes while daily values are plotted along the y-axes.

3.3 Modeling methods

3.3.1 Snow model

The SNOWPACK model was chosen for this study based on its documented performance in forested environments in the SnowMIP2 model inter-comparison project (Rutter et al., 2009). The model calculates the vertical exchange of mass and energy in multi-layered snow and soil profiles. The upper and lower boundary conditions are determined by measured atmospheric forcing and (if available) soil layer thermodynamic properties, respectively. When vegetation cover is present, the upper boundary conditions of the snow or bare ground surface are calculated

by a canopy module in terms of $R_{S\downarrow}$, $R_{L\downarrow}$, and turbulent heat exchange coefficients as outlined in *Lehning et al.* (2006). The SNOWPACK canopy module includes treatment of interception and throughfall of precipitation, evaporation of intercepted snow or rain, transpiration as well as the canopy influence on radiative and turbulent energy fluxes. The model treatment of shortwave radiation transmission is described in detail in *Stähli et al.* (2009). However, most details of the canopy model have not been published to date and the reader is provided a short summary in Appendix A. Hydrometeorological data (Figure 3) used to force the model represented above-canopy fluxes. Hourly temperature data of a three-layer soil profile (i.e. 0 to -10 cm, -10 to -30 cm, and -30 to -60 cm) were provided as forcing to determine the temperature gradient at the snow – soil interface (i.e. Dirichlet boundary conditions). Required soil parameters such as albedo (0.2), porosity (0.21), density (2200 kg m^{-3}), thermal conductivity (3.8 W m^{-1} K^{-1}), and specific heat (900 J kg^{-1} K^{-1}) were estimated based on in-situ soil observations of the largely gravely loam.

3.3.2 Canopy model modification

Scenario NP_{DBT} required a modification to how the canopy model treats direct beam $R_{S\downarrow}$ transmission. Rather than treat both direct and diffuse $R_{S\downarrow}$ with a static canopy absorption factor (see (Eq. A1)), the photo-derived transmissivity of direct $R_{S\downarrow}$ was specified together with hydrometeorological measurements as time-variant input data valid directly at the snow surface. The treatment of above-canopy diffuse shortwave and longwave fluxes was unchanged. Feedback processes within the canopy layer between attenuated shortwave radiation and reemitted longwave radiation were considered via the canopy temperature balance. The

modification was only applied in the case of the scenario NP_{DBT}.

3.3.3 Simulations

The three model scenarios were initialized at locations of the 24 snow depth sensors for three water years. In addition to the 72 sensor-year simulations for each of the three model scenarios, the influence of temporal averaging of direct beam canopy transmissivity on the accuracy of Scenario NP_{DBT} was explored. In this test, the Scenario NP_{DBT} framework was used but the model was forced with direct beam canopy transmissivity estimated at one-minute (instantaneous) time steps, and averaging periods of 10-, 20-, 30-, and 60-minutes. The model forcing data were linearly interpolated accordingly and the five temporal test cases were run with the same inputs and structure. For all presented model scenarios, the third canopy structure parameter, *canopy height*, was specified as 40 m. The canopy extinction coefficient, k_{LAI}, required by the canopy absorption factor (see (Eq. A1)) for all model scenarios was specified as 0.7, slightly lower than reported by *Sicart et al.* (2004) with similar LAI' values, lower canopy heights, and higher canopy density. On the other hand, the value is larger than 0.6 reported by *Stähli et al.* (2009). By design, model simulations were not calibrated to an objective function and the three canopy model parameters (i.e. *canopy openness*, LAI', and *canopy height*) were specified as detailed above. Simulations were initialized at the start of each water year (i.e. 01 October), rather than at maximum accumulation, to permit the model to most accurately represent snowpack properties such as the density profile.

3.3.4 Model evaluation

Model performance was evaluated against the following in-situ observations: 1) manual

SWE estimates; 2) continuous snow depth; 3) snow disappearance date, and 4) the timing of soil moisture increase at a soil depth of -10 cm. Automated snow depth measurements were used in conjunction with density observations from manual snow surveys (Table 3) to estimate location-specific SWE on survey dates. At each sensor location, simulated SWE values at times corresponding to the survey dates were evaluated against measurements as the square root of the variance of the residuals (i.e. root mean square error; RMSE). Similarly, the model SWE bias was calculated as the average difference between modeled and measured SWE values. The bias was computed separately on SWE values obtained during accumulation- and melt-seasons, defined relative to the date of maximum accumulation (see Section 4.1).

An evaluation of simulated and measured hourly (normalized) snow depth during the melt-season was used to infer the relative accuracy of simulated snowmelt rates. Simulated and measured snow depths were normalized by respective snow depths on specified melt-season dates. To focus on melt-driven ablation rather than post-accumulation compaction, the dates used to normalize the depth values were specified as six days after the last significant accumulation event for a given snow year. The six day period was deemed sufficiently long to permit the new snow to settle and beyond six days it was assumed that decreases in snow depth were caused by melt. These dates were 29 February, 2008, 19 April, 2009, and 01 May, 2010. The average (normalized) melt-season snow depth error, in percent, for each simulation and sensor-year was computed as the mean difference between modeled and measured values. The third model evaluation metric, error in the simulated snow disappearance date, was simply the difference, in days, between the simulated and measured snow disappearance dates.

The final metric for model evaluation utilized the availability of soil moisture data from

sensors at a soil depth of -10 cm at three depth sensor locations at each of the four sites. Hence, the simulated timing of seasonal meltwater fluxes exiting the snowpack base, in mm per time step, was compared to the measured timing of the seasonal increase in VWC (at -10 cm soil depths). The initial timing of simulated snowmelt infiltration was determined as the first peak in meltwater flux exceeding 6 mm day^{-1} for three consecutive days during which time no liquid precipitation events occurred. The 'first' peak was defined as that occurring after continuous snow cover was recorded for a minimum of 30 days. The above criteria excluded from consideration early season accumulation and subsequent complete melt events, rain-on-snow events, and the slow release of meltwater throughout the snow-covered period due to ground heat fluxes. The date of measured snowmelt infiltration at -10 cm soil depth was determined as the first pulse exhibiting a minimum of 3% volumetric increase in VWC over three days during which time no liquid precipitation events occurred and after snow cover had persisted for a minimum of 30 days. The error was computed as the difference, in days, between the simulated and measured initial meltwater pulses. A slight time lag would be expected between the simulated meltwater exiting the snowpack and that being measured at -10 cm soil depth, such that a small degree of 'error' on the order of a day or two would occur even under conditions of ideal model performance.

The evaluation of sensor-year simulations against the metrics listed above (other than soil moisture) was limited by depth sensor functionality. Thus, not all sensor-years could be evaluated with all metrics. For consistent inter-comparison of different sensor-years, SWE metrics were evaluated for those sensor-years that included at least one survey measurement made during both the accumulation- and melt-season. An exception was made for water year

2010, in which the 02 May survey was the last of the season and corresponded to maximum accumulation in some sensor locations but the melt-season in others. In this case, the 02 May, 2010 survey was considered to represent the melt-season and the other three surveys the accumulation-season (Table 3). Of the 24 sensor locations, 12, 17 and 19 met this criterion in 2008, 2009, and 2010, respectively. Similar data limitations influenced the other three model evaluation metrics. The normalization of melt-season snow depth was only applied to sensor-years in which snow depth was recorded for at least 50% of the melt-season. This criterion was met at 16, 18, and 20 sensor locations in 2008, 2009 and 2010, respectively. The snow disappearance date was recorded at 17, 19, and 21 sensor locations in the three respective years. Of the 12 snow depth sensor locations with underlying soil moisture sensors, the timing of the seasonal increase in VWC was measured at 10, 8, and 8 locations in 2008, 2009, and 2010, respectively.

The next section presents results from the suite of depth and density observations for three water years followed by an illustrative example of the three model scenarios at two different locations for the same season. Results are then summarized for the three model scenario runs conducted on all sensor-years.

3.4 Results

3.4.1 Depth and SWE measurements

Compared to the 86-year historical record from CCSS measurements near Sites 3 and 4 (Figure 1), maximum annual SWE was near the long-term average (~ 950 mm) in 2008, was 48% below average in 2009, and was 43% above average in 2010. Seasonal maximum SWE was

estimated to coincide with density surveys conducted on 23 March, 2008; 21 March, 2009; and 02 May, 2010 (Musselman et al., 2012). The average maximum SWE across all four sites was 737 mm in 2008, 420 mm in 2009, and 1074 mm in 2010. The seasonal timing and duration of the melt-seasons are defined both by the date of maximum SWE and the date of snow disappearance. The date of snow disappearance varied markedly by year, site aspect and elevation, and between sensors at individual sites (Figure 6). The average snow disappearance dates across all sites were 25 May, 2008, 17 May, 2009, and 15 June, 2010. The average annual melt-season duration was 64, 57, and 45 days corresponding to seasonal average melt rates of 11.5, 7.4, and 23.9 mm day^{-1} in 2008, 2009, and 2010, respectively. The standard deviation (σ) of the snow disappearance date determined at all sensor locations on an average, per-site basis was 10.4 days in 2008, 5.8 days in 2009, and 7.8 days in 2010. Water year 2008 exhibited the most variability in the date of snow disappearance of all three years. This is attributed, in part, to the 2008 melt-season having the longest duration, the fewest snow events (see Figure 4), and the least cloud cover (see *Musselman et al.* [2012]) of the three years. These prolonged melt conditions could be a potential cause of the pronounced sub-canopy snowpack variability observed in 2008.

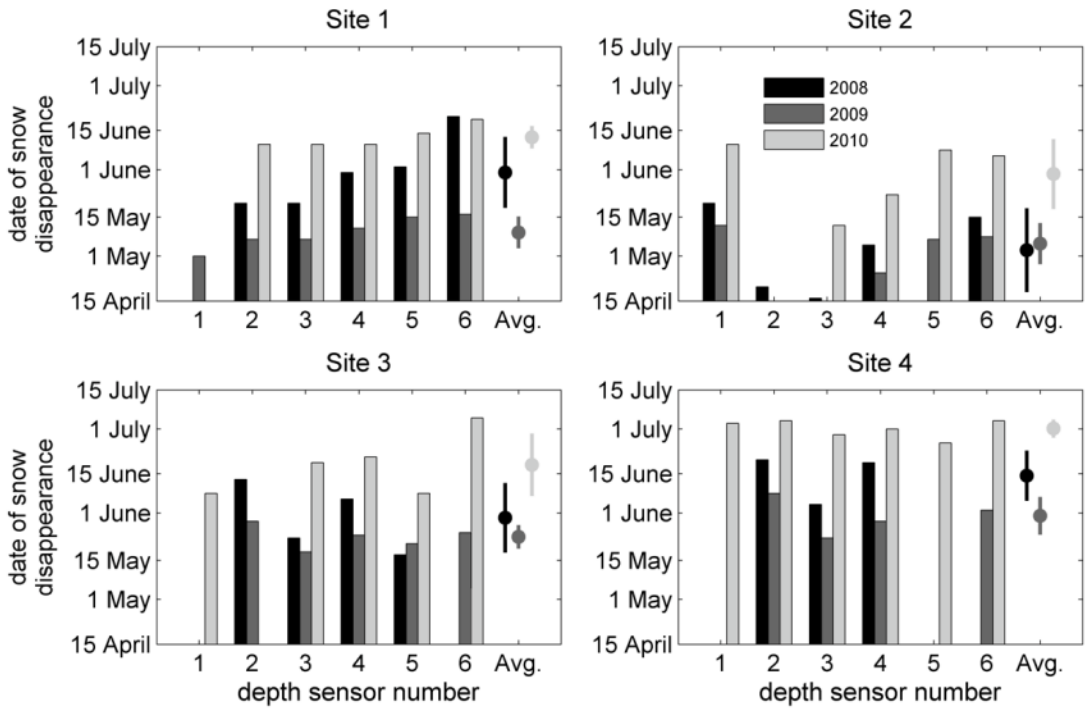

Figure 3.6. Date of snow disappearance measured by the six ultrasonic snow depth sensors at each of the four sites for water years 2008, 2009, and 2010. The average and standard deviation of the snow disappearance date computed for the operational sensors at each site for the three years are indicated by the filled circles and vertical bars.

A similar explanation could be applied to water year 2010, which exhibited the second most variable snow disappearance date despite having the shortest melt-season. However, rather than a prolonged melt-season, enhanced energy fluxes coincident with a *later* melt-season likely resulted in high variability in the date of snow disappearance. On average over all years, σ was greater ($p<0.05$) at Sites 2 and 3 (10.3 days) than at Sites 1 and 4 (5.6 days). This is attributed to Sites 1 and 4 being north-facing with relatively homogeneous aspect relative to Sites 2 and 3 (Table 1). The observations indicate that both seasonal meteorology and physiography (i.e. terrain and canopy configuration) interact to determine the date of snow disappearance and the timing and duration of meltwater inputs. The high variability of the observations and the dynamic nature of sub-canopy snow processes provide the motivation for this modeling study.

3.4.2 Illustrative example of two different simulation results

Results from Scenarios *N*, *NP*, and NP_{DBT} run at two sensor locations (site 2, sensor 2; and site 3, sensor 4) for water year 2008 exhibited different trends in the magnitude and sign of the respective melt-season model errors (Figure 3.7, upper panels). At both locations, minimal differences in snow depth or SWE were observed from initial accumulation until late-February, after which melt began in earnest and the scenario simulations diverged. Compared to measurements, the *N*, *NP* and NP_{DBT} scenarios run at site 2, sensor 2 over-estimated SWE on 23 March by 391.9, 429.5, and 211.6 mm, respectively. Snow had disappeared from the sensor location by the 27 April survey date, which was captured by NP_{DBT} (i.e. 0 mm SWE) but Scenarios *N* and *NP* exhibited high positive SWE biases (Figure 3.7). The normalized *N* and *NP* predictions of melt-season snow depth had an average error of +20.8% and +18.4% and an error in the predicted snow disappearance date of +32 days and +28 days, respectively (Figure 3.7, bottom-left panel). The overestimation of normalized melt-season snow depth is analogous to an underestimation of snowmelt. The NP_{DBT} model improved the predictions significantly for this sensor-year with an average normalized snow depth error of -0.2% and an error in the date of simulated snow disappearance of +7.5 days. The cumulative sub-canopy direct beam solar radiation from 29 February to 26 April (i.e. NP_{DBT} snow disappearance date) was 470 MJ m^{-2}, 685 MJ m^{-2}, and 852 MJ m^{-2} for the *N*, *NP*, and NP_{DBT} scenarios, respectively (Figure 3.7). Note that the *NP* and NP_{DBT} scenarios simulated 45.7% and 81.3% greater direct beam radiation than the nominal scenario *N* over this time period.

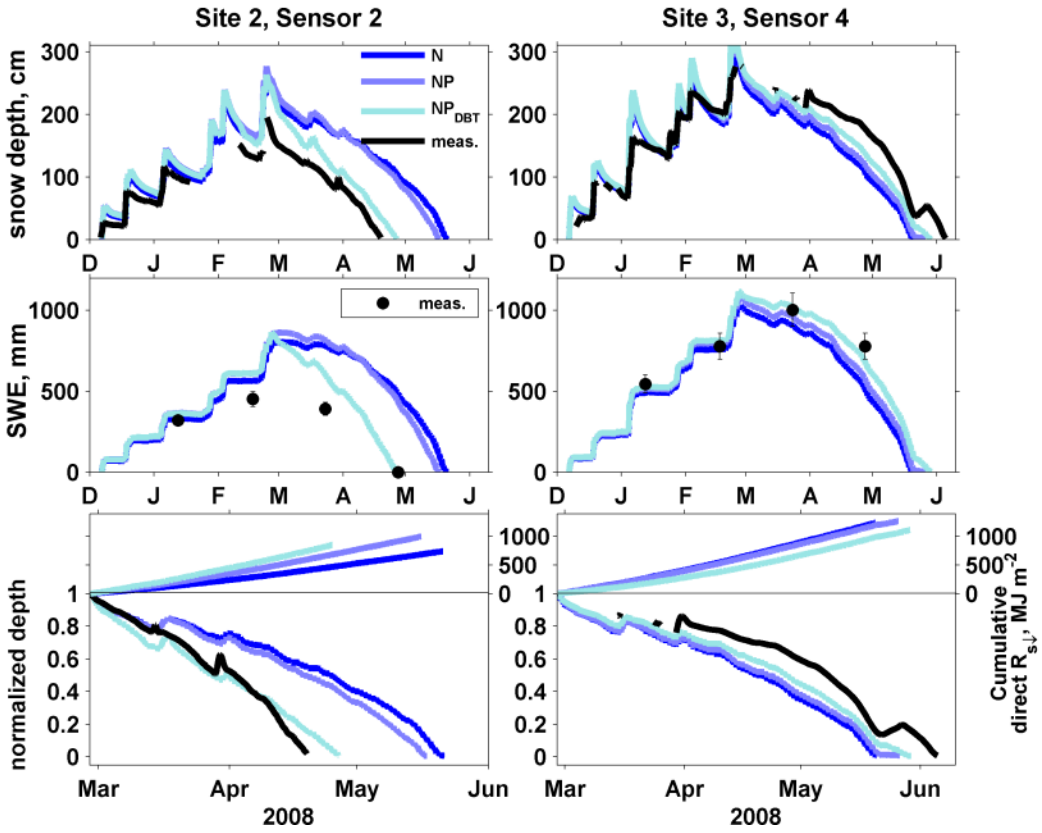

Figure 3.7. Simulations and measurements of snow depth (top) and SWE (center) at site 2, sensor 2 (left panels) and site 3, sensor 4 (right panels) for water year 2008. The simulated and measured melt-season snow depth normalized by the respective depth on February 29, 2008, six days after the last appreciable accumulation event (bottom panels) are plotted with the cumulative sub-canopy direct beam solar radiation (horizontal) simulated by the three scenarios (bottom panels, upper axes). Error bars on the reported SWE measurements represent a 5% uncertainty in both snow density and depth observations.

All **2008** simulations run at the site 3, sensor 4 also accurately estimated SWE and depth in early winter and errors were more pronounced in the spring (Figure 7, right panels). Unlike simulations shown in the left-center panel of Figure 7 in which the nominal *N* and *NP* scenarios *overestimated* measured SWE, the same 2008 scenario runs at site 3, sensor 4 *underestimated* SWE by 95 mm and 43 mm, respectively (Figure 7, right-center panel). Scenario NP_{DBT} slightly overestimated SWE by 24 mm. The normalized *N* and *NP* melt-season snow depth predictions had an average error of -18.5% and -16.0% and an error in the predicted snow disappearance date of -16 days and -10 days, respectively (Figure 7, lower-right panel). The underestimation of

normalized melt-season snow depth is analogous to an overestimation of snowmelt. The NP_{DBT} model improved the predictions for this sensor-year with an average normalized snow depth error of -12.5% and a -7 day snow disappearance date error. The cumulative sub-canopy direct beam solar radiation from 29 February to 26 April was 836 MJ m^{-2}, 807 MJ m^{-2}, and 616 MJ m^{-2} for the *N*, *NP*, and NP_{DBT} scenarios, respectively (Figure 7, lower-right panel). Note that the NP_{DBT} scenarios at both sensor locations in Figure 7 outperformed the nominal scenarios while simulating 81.3% *more* (site 2, sensor 2) and 26% *less* (site 3, sensor 4) cumulative direct beam solar radiation over the same time period (29 February to 26 April) (Figure 7, lower panels). The results suggest that the dynamic treatment of direct beam canopy transmissivity by the NP_{DBT} scenario is able to correct for both positive and negative cumulative energy biases resulting from the use of static, bulk canopy transmissivity estimates.

The model differences seen during the melt-season at the Site 2, sensor 2 location in 2008 are also reflected in the simulated meltwater fluxes from the snowpack base compared to measured soil moisture at -10 cm depth at the same location (Figure 8). Timing differences in the initiation of the melt fluxes from the snowpack base simulated by the *N* and *NP* models were +9 and +7 days, respectively (Figure 8). The NP_{DBT} model improved these estimates with simulated initial meltwater flux from the snowpack base preceding the measured soil moisture increase by two days (Figure 8); note that the snowmelt flux would be expected to precede soil moisture response. All **2008** simulations run at the site 3, sensor 4 also accurately estimated SWE and depth in early winter and errors were more pronounced in the spring (Figure 7, right panels). Unlike simulations shown in the left-center panel of Figure 7 in which the nominal *N* and *NP* scenarios *overestimated* measured SWE, the same 2008 scenario runs at site 3, sensor 4

underestimated SWE by 95 mm and 43 mm, respectively (Figure 7, right-center panel). Scenario NP_{DBT} slightly overestimated SWE by 24 mm. The normalized *N* and *NP* melt-season snow depth predictions had an average error of -18.5% and -16.0% and an error in the predicted snow disappearance date of -16 days and -10 days, respectively (Figure 7, lower-right panel). The underestimation of normalized melt-season snow depth is analogous to an overestimation of snowmelt. The NP_{DBT} model improved the predictions for this sensor-year with an average normalized snow depth error of -12.5% and a -7 day snow disappearance date error. The cumulative sub-canopy direct beam solar radiation from 29 February to 26 April was 836 MJ m^{-2}, 807 MJ m^{-2}, and 616 MJ m^{-2} for the *N*, *NP*, and NP_{DBT} scenarios, respectively (Figure 7, lower-right panel). Note that the NP_{DBT} scenarios at both sensor locations in Figure 7 outperformed the nominal scenarios while simulating 81.3% *more* (site 2, sensor 2) and 26% *less* (site 3, sensor 4) cumulative direct beam solar radiation over the same time period (29 February to 26 April) (Figure 7, lower panels). The results suggest that the dynamic treatment of direct beam canopy transmissivity by the NP_{DBT} scenario is able to correct for both positive and negative cumulative energy biases resulting from the use of static, bulk canopy transmissivity estimates.

The model differences seen during the melt-season at the Site 2, sensor 2 location in 2008 are also reflected in the simulated meltwater fluxes from the snowpack base compared to measured soil moisture at -10 cm depth at the same location (Figure 8). Timing differences in the initiation of the melt fluxes from the snowpack base simulated by the *N* and *NP* models were +9 and +7 days, respectively (Figure 8). The NP_{DBT} model improved these estimates with simulated initial meltwater flux from the snowpack base preceding the measured soil moisture increase by two days (Figure 8); note that the snowmelt flux would be expected to precede soil moisture

response.

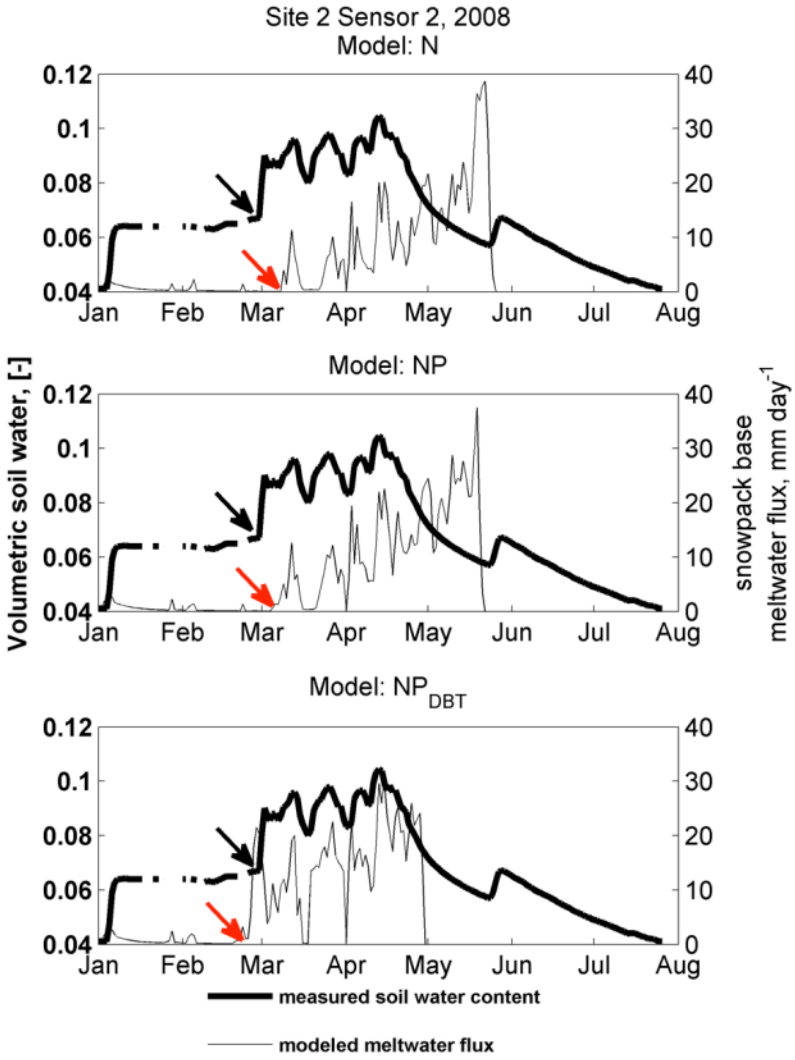

Figure 3.8. Measured volumetric soil water content at -10 cm soil depth (left axes, bold line) and simulated meltwater flux from the snowpack base (right axes, thin line) from water year 2008 at the same site 2, sensor 2 location and three model runs (*N*, top; *NP*, middle; NP_{DBT}, bottom) shown in Figure 3.7 (left panels). Red arrows indicate model-simulated timing of the initial spring meltwater pulse from the snowpack base. Black arrows indicate the timing of the initial spring meltwater pulse as measured by a soil moisture sensor at -10 cm.

3.4.3 Results from all sensor years

3.4.3.1 SWE simulations

On average across 62 operational sensor-years the *N*, *NP*, and NP_{DBT} scenarios yielded relatively high SWE RMSE values of 151, 146 and 127 mm, respectively. During the three accumulation-seasons, no single scenario consistently reduced the SWE biases (Figure 3.9). During the melt-seasons, lower (upper) elevation SWE biases were positive (negative) for all scenarios (Figure 3.9). At lower elevations during the 2008 melt-season, the high positive biases in the *N* (316.6 mm) and *NP* (341.8 mm) scenarios were reduced by approximately 66% with the NP_{DBT} scenario (106.4 mm) (Figure 3.9). Similar reductions in positive melt-season SWE biases obtained with the NP_{DBT} scenario relative to the mean SWE biases of the two nominal scenarios were obtained at lower elevations in 2009 (74% reduction) and 2010 (45% reduction) (Figure 3.9). The *NP* model scenarios reduced the average SWE RMSE and biases of the *N* scenarios by $< 5\%$.

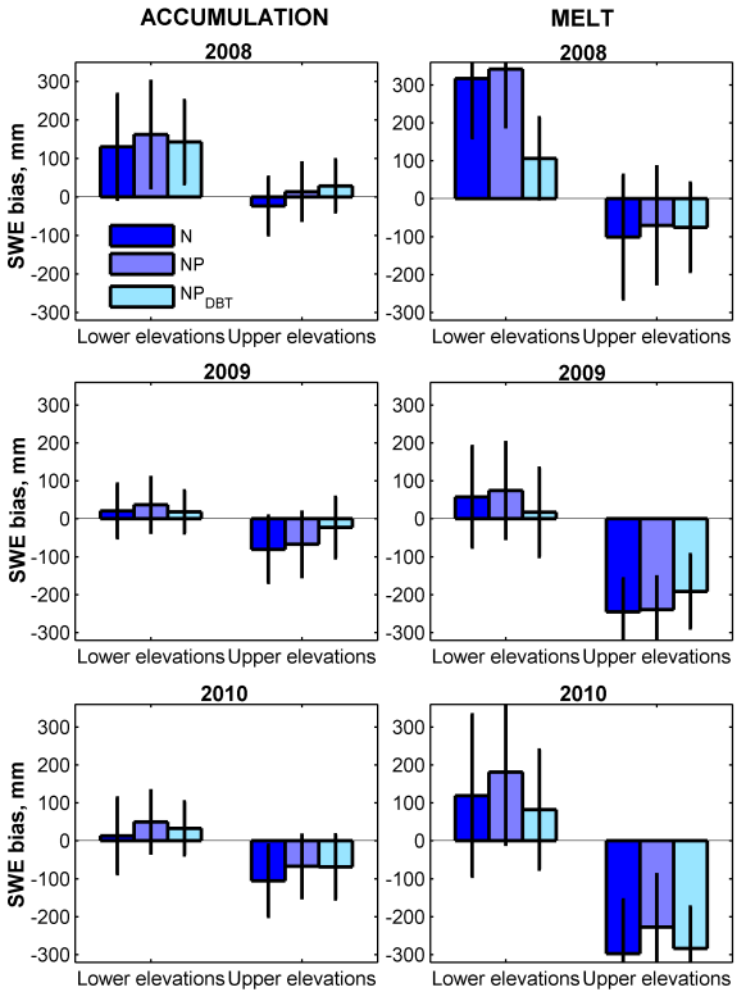

Figure 3.9. Biases in simulated SWE from the three model scenarios run at lower (Sites 1 and 2) and upper (Sites 3 and 4) elevation sensor locations during the 2008, 2009, and 2010 accumulation and melt-seasons respectively computed on measured and modeled SWE values before (left column) and after (right column) maximum accumulation. The error bars represent the mean bias ± the standard deviation of the bias.

3.4.3.2 Snow disappearance date

Across the 57 sensor-years in which measurements were available, the average error in the date of simulated snow disappearance was positively biased toward later snow cover by 7.7, 7.4 and 1.7 days for the *N*, *NP*, and NP_{DBT} scenarios, respectively. Relative to the *N* and *NP* scenarios, the NP_{DBT} scenario reduced the mean bias in the snow disappearance date from 7.9 and 7.6 to 0.6 days in 2008 and from 15.1 and 15.0 to 6.9 days in 2010 for the three respective

scenarios (see Figure 3.10). In 2009, a mean bias reduction was not observed; the *N*, *NP* and NP_{DBT} scenarios had an average bias of -0.7, -1.2, and -3.1 days, respectively.

The mean absolute error (MAE) values of the simulated snow disappearance date from all *N* scenarios (13.8 days) and *NP* scenarios (13.5 days) were reduced by ~ 37% to 8.7 days with the NP_{DBT} scenario; 40%, 19%, and 43% average reductions in 2008 – 2010, respectively. The relative improvement between the *N* and *NP* model scenarios as indicated by the MAE in simulated snow disappearance date was noticeable in 21 of the 57 sensor-years, but the average improvement was less than two days and the difference was not statistically significant (Figure 3.10). The NP_{DBT} scenario reduced the average of the *N* and *NP* snow disappearance date errors in 40 of the 57 sensor-years (Figure 3.10). When evaluated on the basis of individual years, on average, the NP_{DBT} model simulations for water years 2008 and 2010 showed significant improvements over the *NP* scenario in the predicted snow disappearance date of 6.0 ($p<0.05$) and 9.2 ($p = 0.01$) days, respectively. In 2009, the mean reduction in snow disappearance date error between the *NP* and NP_{DBT} runs was two days and the difference was not statistically significant. Model error and relative improvement also showed trends with elevation. When simulations from all years were evaluated, compared to the *NP* simulations, the lower (i.e. Sites 1 and 2) and upper (i.e. Sites 3 and 4) elevation NP_{DBT} runs reduced the MAE in the predicted date of snow disappearance by seven and three days ($p<0.01$), respectively.

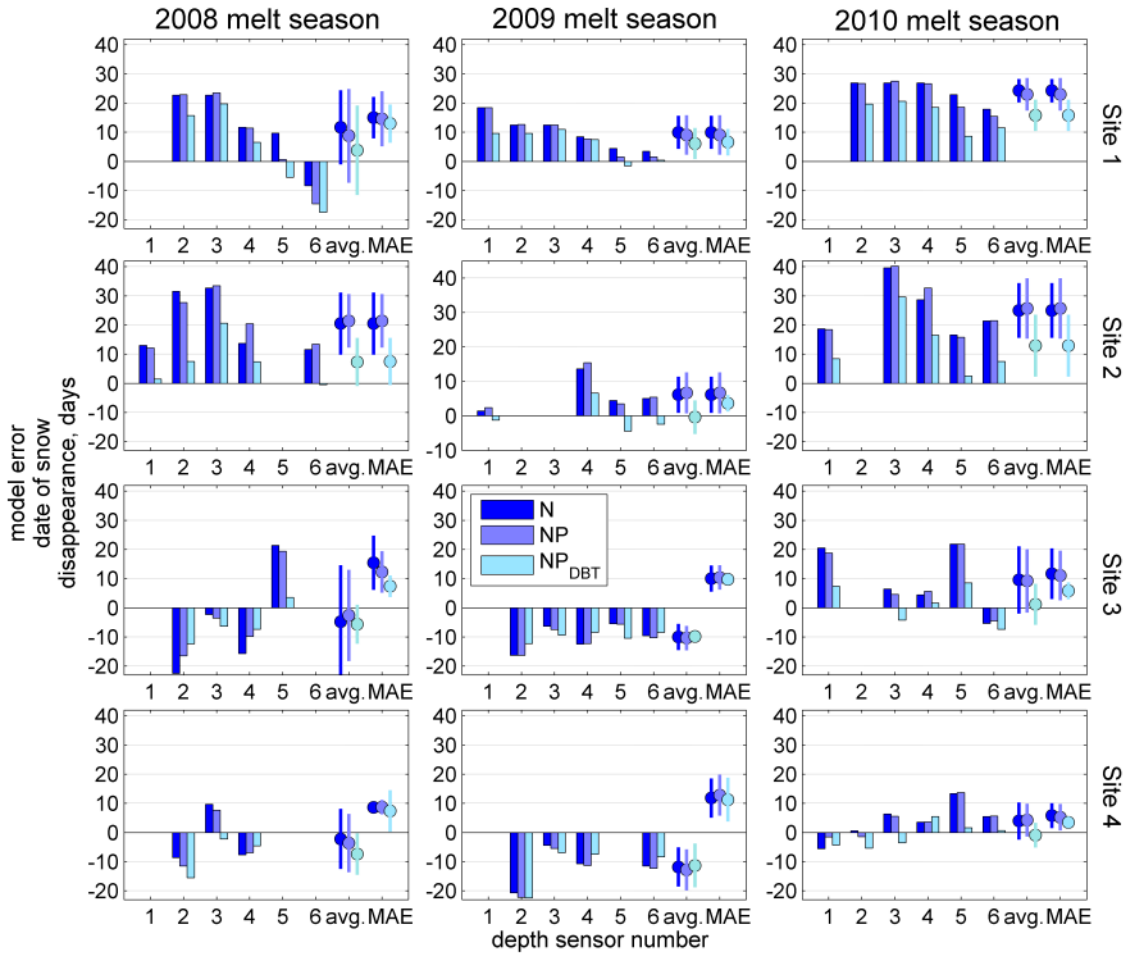

Figure 3.10. Simulated date of snow disappearance compared to depth sensor observation provided as model error (model – measurement) in number of days (y-axis) for each of the three model cases and for simulations conducted at locations of operational sensors (x-axis) at the four sites (panel rows) for water years 2008, 2009, and 2010 (panel columns). Site-average errors and site mean absolute errors and standard deviations are indicated by the filled circles and vertical lines, respectively.

3.4.3.3 Normalized melt-season snow depth

Based on the 54 sensor-years evaluated for error in the normalized melt-season snow depth, the *N* and *NP* scenarios had a slight positive bias of 3.8% and 3.3%, respectively, while the NP_{DBT} scenario had a slight negative bias of -1.1% (Figure 11). In 2008 and 2009, scenarios *N* and *NP* had positive biases and NP_{DBT} exhibited negative biases; the average biases were less than 2%. In 2010, large positive melt-season snow depth biases of 8.4% and 8.3% from the *N*

and *NP* scenarios were reduced to 0.2% for the NP_{DBT} scenarios (Figure 11). The absolute errors of the normalized melt-season snow depth for the three scenarios in 2010 were 11.2%, 10.6%, and 7.8%, respectively. The results indicate snowmelt simulations were generally improved with an explicit treatment of direct beam canopy transmissivity and improvements were greatest in the year with the latest melt-season.

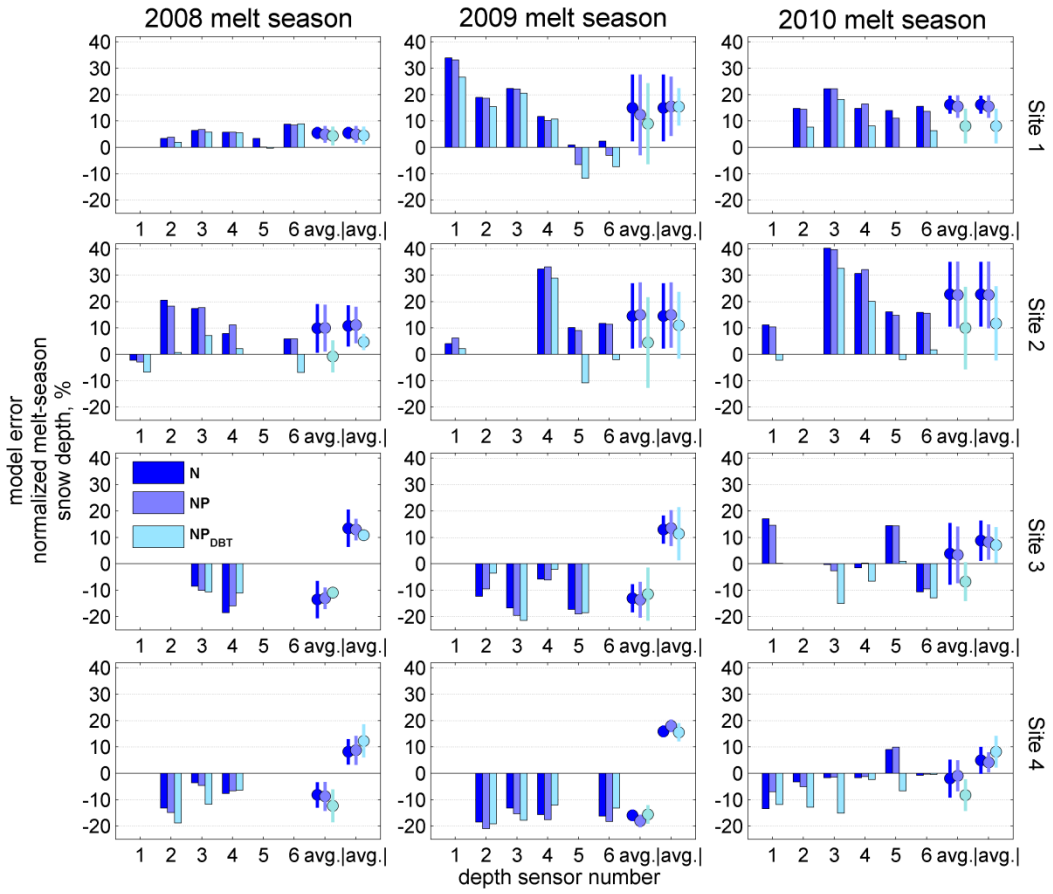

Figure 3.11. Normalized melt-season snow depth error, in percent, for each scenario run for sensor-years that recorded a minimum of half the time-steps over a period between six days after each year's last appreciable accumulation event and the date of snow disappearance. Missing values represent either sensor-years in which the depth sensor did not record at least 50% of the melt-season or sensor-years in which depth data were missing on the specified normalization date.

3.4.3.4 Timing of meltwater soil infiltration

In general, large differences were found between the simulated timing of meltwater exiting the snowpack base and the timing of initial seasonal increase in soil water content measured at -10 cm (Table 4). Overall, the NP_{DBT} scenario reduced snowmelt infiltration timing errors by 50% in nearly half of the sensor-years compared to the *N* and *NP* model scenarios. At lower elevations, modeled meltwater flux timing occurred later than the measured snowmelt infiltration by 22, 20 and 10 days for scenarios *N*, *NP*, and NP_{DBT}, respectively. At upper elevations, the modeled meltwater flux occurred 18 days earlier than observed for all three scenarios in 2008 and 2009; but occurred 15, 8 and 6 days later than observed in 2010 for the three respective scenarios. Improvements (greater than three days) in the predicted timing of initial melt flux between scenarios *N* and *NP* were only recorded in three sensor-years during which an average improvement of 13 days was observed (Table 4). Improvements gained over the *N* and *NP* model scenarios with the NP_{DBT} scenario were observed in 11 sensor-years with an average improvement of 11 days. Interestingly, in no case did the NP_{DBT} scenario increase the mean absolute melt flux timing error by more than one day compared to the *N* or *NP* scenarios (Table 4).

Table 3.4. Lag / error, in number of days, between modeled date of initial spring meltwater flux from the snowpack base and the date of seasonal volumetric soil moisture increase measured at -10 cm beneath the soil surface at three snow depth sensor locations at each of the four sites for water years 2008, 2009 and 2010. Results from the three model scenarios at each sensor location and the mean absolute error (MAE) for each site for the three years are included. Missing values (-) reflect an incomplete soil moisture data record.

	model	2008				2009				2010			
Snow depth sensor :		2	3	4	MAE	2	3	4	MAE	2	3	4	MAE
Site 1	N	17	29	*25*	24	-	*30*	-	30	*9*	-	-	9
	NP	4	30	*13*	16	-	*31*	-	31	*8*	-	-	8
	NP_{DBT}	-7	5	*2*	5	-	*30*	-	30	*6*	-	-	6
Site 2	N	*14*	10	14	13	27	28	*28*	28	14	17	*48*	26
	NP	*12*	9	18	13	13	28	*28*	23	16	14	*49*	26
	NP_{DBT}	*0*	2	6	3	11	14	*13*	13	8	7	*42*	19
Site 3*	N	*-5*	*-21*	-	13	9	*-13*	-	11	*14*	5	-	10
	NP	*-4*	*-22*	-	13	9	*-13*	-	11	*14*	4	-	9
	NP_{DBT}	*-6*	*-22*	-	14	9	*-11*	-	10	*11*	7	-	9
Site 4	N	*-39*	*-40*	-	40	-20	*-26*	-	23	39	0	-	20
	NP	*-38*	*-38*	-	38	-20	*-27*	-	24	16	-1	-	9
	NP_{DBT}	*-39*	*-40*	-	40	-20	*-25*	-	23	11	-4	-	8

* The soil moisture sensors at Site 3 are positioned beneath snow depth sensors 3, 4 and 5.

Despite the improvements with the explicit treatment of direct beam canopy transmissivity, the high MAE values in Table 4 (23 sensor-year MAE of 18 days with the NP_{DBT} scenario) indicate substantial unresolved issues related to predicting the timing of melt fluxes into the soil system. This finding was surprising as maximum SWE and the date of snow disappearance were often simulated with a high degree of accuracy (see Section 5). The results highlight challenges with both the simulation and measurement of snowmelt runoff. Distinct melt-freeze layers on the order of 2 to 5 cm, a result of surface melting between snow events, were commonly observed in the snowpack. These icy melt-freeze layers were a result of surface melting between snow events and subsequent refreezing. The layers may have acted as barriers

to capillary flow and could have impeded preferential 'finger' flow formation by lateral dispersion [Waldner et al., 2004]. Most models are not designed to simulate these nonlinear meltwater dynamics. Similar heterogeneous flow patterns are known to exist in the soil matrix. In the case of pronounced lateral dispersion and heterogeneous preferential flow patterns, a single point measurement of near-surface soil water content may be inadequate to capture the snowpack runoff dynamics occurring over a larger spatial footprint. It should also be noted that any model misspecification of rain/snow input will influence the timing of melt fluxes as discussed in more detail below.

3.4.4 Sensitivity to temporal averaging of direct beam canopy transmissivity

The effect of averaging the direct beam canopy transmissivity over time periods of 60-minutes, 30-minutes, 20-minutes, and 10-minutes as well as forcing the model with 1-minute instantaneous values was first examined at a single location (Figure 12). Relative to automated measurements, the mean error in the normalized depth simulated by models *N*, *NP* and the direct beam model run at 60-minute temporal resolution (i.e. $NP_{DBT(60)}$) were +17.2%, +14.8%, and +13.7%, respectively (Figure 12, bottom panel), and errors in snow disappearance date for this sensor-year were +21, +19, and +20 days, respectively. Running the NP_{DBT} model at a time step of 30 minutes reduced the normalized melt error by 50% and the snow disappearance date error by 33%. The error was further reduced at finer temporal resolution; the normalized melt errors of the model forced at 20-, 10-, and 1-minute resolution were +4.4%, +0.4% and -5.5%, respectively, and the simulated snow disappearance date errors for the three models were +12,

+7 and +1 days, respectively (Figure 12, bottom panel).

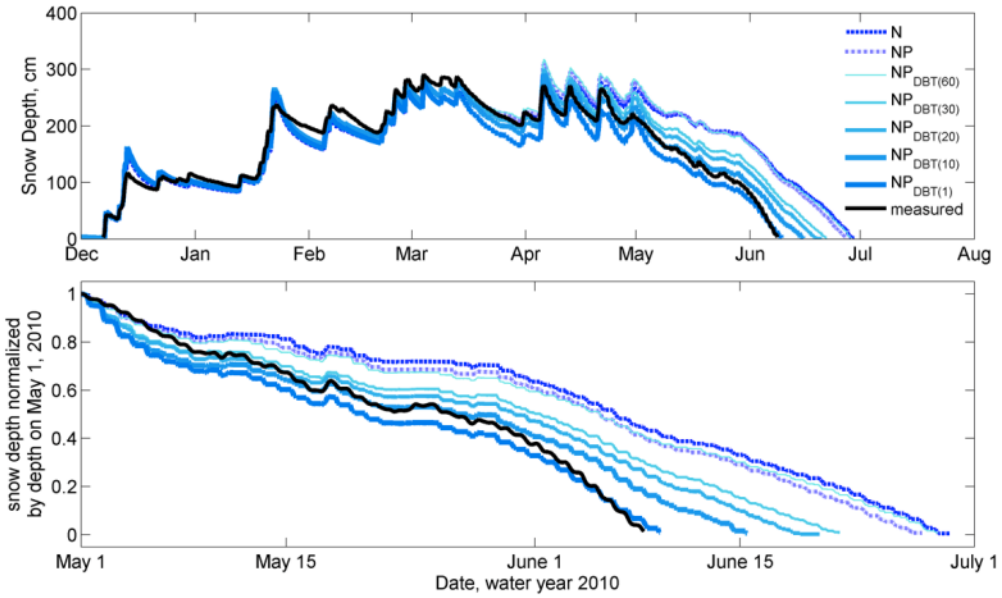

Figure 3.11. Snow depth simulations and measurements during the 2010 water year at Site 3, sensor 1 (upper figure); the location of photos shown in Figures 4 and 5. The effect of averaging the direct beam canopy transmissivity used to force the NP_{DBT} models is examined at 60-, 30-, 20-, and 10-minute averaging and 1-minute instantaneous steps. Melt-season snow depth was normalized by the respective simulated or measured (black line) depth on May 1, 2010 (lower figure) to compare simulated melt rates to measured values.

When all sensor-years were evaluated, improved results from running NP_{DBT} at higher temporal resolution were not as ubiquitous as the sensor-year in Figure 12 illustrates. Compared to the simulated error in snow disappearance date predicted by scenario *NP*, the $NP_{DBT(60)}$ scenario reduced errors by four days in 2008 ($p<0.05$) and one day each in 2009 and 2010. The $NP_{DBT(30)}$ simulations further reduced error by two days in 2008, one day in 2009 and by seven days in 2010 ($p<0.05$). Reducing the time step from 30-minutes to 20-minutes showed no mean absolute error reduction in 2008 and 2009, and an error reduction of one day in 2010. Further reducing the time step from 20-minutes to 10-minutes showed no mean improvement for any year (not shown). Interestingly, increasing the time step from 10-minutes to 1-minute increased

the average model error of the 57 sensor-years in which snow disappearance was recorded by four days in 2008 and three days on average in 2009 and 2010 (not shown). Note that the error reductions reported above that were not statistically significant (i.e. $p>0.05$) were not provided with p-values.

3.5 Discussion

Of the three SNOWPACK model scenarios tested, the bulk Scenario *N* exhibited the greatest overall error when evaluated against point metrics of SWE, snow disappearance date, and the relative timing of snowmelt soil infiltration. In scenario *N*, *canopy openness* values for depth sensor / simulation locations were sampled from the 30 m gridded canopy product. The short spacing (8 to 55 m) between sensor locations relative to the coarser grid scale of the satellite product caused three to four sensors at a given site to fall within the same grid element. In these instances, multiple neighboring sensor / simulation locations were assigned the same *canopy openness* value corresponding to the common NLCD grid cell. In these cases, because LAI' was also held constant for scenario *N*, the only location-specific differences provided to the model at a given site were slope and aspect. The results highlight challenges associated with the evaluation of snowmelt models that use gridded vegetation data against ground-based (often point-scale) observation systems. This scale mismatch was implicit in the experimental design. A common source of uncertainty is faced by studies that evaluate gridded model output against point-scale automated station measurements without explicit consideration of the sub-grid representativeness of the station (Meromy et al., 2012). While it is possible that Scenario *N* would have been better evaluated against gridded measurements of snowpack processes,

Scenario *NP* was designed to test whether model skill was improved when parameterized with point-scale canopy measurements. Any improvement with Scenario *NP* over Scenario *N* would implicitly be a result of 1) removing this scale mismatch and 2) improving point-specific canopy model parameterization.

Systematic model biases were not observed across all sites and years, but errors of similar direction and magnitude were observed at lower and upper elevation sites for particular years. These models errors were likely a combined effect of errors in the meteorological forcing data, the challenge of simulating mixed rain-snow precipitation events, and the lack of consideration of sub-grid scale canopy variability. For example, the high positive SWE bias at lower elevations in 2008 (Figure 9) were the result of a significant rain-on-snow event in early January as indicated by the increased soil moisture at sites 1 and 2 (see Figure 2). During this event, significantly more rain fell at lower elevations where air temperatures were above freezing but below the 1°C rain-snow temperature threshold specified to the model, resulting in a model misallocation of SWE to the snowpack that persisted as a positive bias through the season. In contrast, negative SWE biases were observed at upper elevations (Figure 9), possibly as a result of errors in the seasonal lapse rates used to estimate upper elevation precipitation.

The minimal improvement over the bulk scenario *N* with the added photo-derived canopy structure detail provided to Scenario *NP* was surprising. On average the photo-derived LAI' specified to Scenario *NP* was 2.53 m^2 m^{-2} less than that specified to the bulk model; a fact that should have significantly reduced the positive bias in snow cover persistence seen in Scenario *N* by permitting more radiation to pass through the canopy. In addition, hemispherical *SVF* (used in Scenario *NP*) has been found to exceed satellite-derived 'viewable gap fraction' (used in

Scenario *N*) as a result of off-nadir satellite view geometry, slope and aspect (Liu et al., 2004). However, the use of $SVF_{65°}$ rather than $SVF_{90°}$ would be expected to reduce the bias reported by *Liu et al.* (2004). Compared to the bulk Scenario *N*, the two photo-derived metrics would effectively reduce the model representation of canopy effects and theoretically should have reduced the bias in Scenario *N* snow cover persistence. Simulations of sub-canopy solar radiation are known to be highly sensitive to the value of the canopy extinction parameter k_{LAI} (e.g. Jost et al., 2009). It is possible that the constant k_{LAI} coefficient of 0.7 used in all scenarios was too high and could partially explain the minimal improvement between the *N* and *NP* scenarios. Potential radiative feedbacks in the canopy model could also explain the limited model improvement. For example, a reduction in simulated vegetation coverage would increase the canopy transmission of shortwave but reduce the canopy absorption and emission of longwave radiation. In a natural forest canopy, these radiative feedbacks are nonlinear three-dimensional processes, a thorough analysis of which is beyond the scope of this study.

The limited accuracy of the *N* and *NP* scenarios points to challenges associated with the use of a big-leaf canopy module at the point-scale. Aside from parameter uncertainty, a Beer's-type exponential reduction of above-canopy shortwave radiation may be too coarse of a scaling method to approximate the in-situ radiation dynamics beneath a heterogeneous forest (Ni et al., 1997). Of particular concern is the treatment of direct beam solar radiation because bulk canopy structure parameters are measured over an inordinately larger canopy area than impacts the direct beam. In addition, the non-uniform (and non-random) distribution of vegetation structure causes a many-to-one problem when using a bulk *canopy openness* metric (i.e. derived from photos or satellite). Many different canopy gap configurations can result in the same *canopy openness*

value. These different canopy configurations will influence mass and energy exchange differently, yet the differences would not be resolved with the single *canopy openness* metric. Rather than treat all fluxes with a bulk canopy treatment, an explicit consideration of detailed canopy structure may be more accurate; the NP_{DBT} model was designed to test this hypothesis.

In general, significant improvements were gained from a modification of SNOWPACK to accept a time-variant input of direct beam canopy transmissivity derived from hemispherical photos. The benefit of the NP_{DBT} scenario was particularly reflected in melt-season model results. Both positive and negative biases in melt-season SWE and snow disappearance date predicted by the *N* and *NP* scenarios were greatly reduced with the NP_{DBT} scenario. The reductions of both positive and negative biases indicate the effectiveness of the direct beam modification; NP_{DBT} is not simply globally increasing or decreasing the canopy transmission. The positive melt-season biases and subsequent improvements with the explicit treatment of direct beam canopy transmissivity suggest that the big-leaf model tends to underestimate shortwave canopy transmission during the melt-season when solar radiation is relatively high and the sun tracks across a higher and much larger sky area (see Figure 5b).

The inter-annual differences in relative model improvement gained from the explicit treatment of the direct beam may be attributable to inter-annual differences in melt-season meteorology. *Musselman et al.* (2012) computed a clearness index from the same above-canopy shortwave radiation data used in this study for melt-seasons 2008-2010. The index identified 4, 23, and 8 cloudy days for the three respective melt-seasons. The results indicate that the cloudiest year (i.e. 2009) showed the lowest degree of model improvement with the NP_{DBT} scenario. Of the three years, 2009 also exhibited the least SWE and lowest variability in

measured snow disappearance date. Conversely, the melt-season errors in the bulk, nominal models were generally greater in magnitude and positive (indicating an underestimation of melt) in 2010 when snowmelt occurred later in the year, under conditions of enhanced energy fluxes. Of the three years evaluated, improvements gained by the direct beam modification were greatest under these conditions of enhanced energy, higher solar elevations, and reduced cloud cover.

Positive and negative errors in the simulated timing of snowmelt soil infiltration (Table 4) indicate substantial issues related to predicting the timing of melt fluxes into the soil system despite accurate representation of peak SWE and snow disappearance date. It is possible that a model misspecification of snow instead of rain at upper elevations during a January 4-7, 2008 rain-on-snow event underestimated the liquid water absorbed by the snowpack; the soil moisture record (see Figure 2) indicates all liquid precipitation from this event at upper elevations was stored in the pack. As the liquid water content in a snowpack affects the thermodynamic properties as well as the melt dynamics and runoff production, particularly in areas of deep snow cover (Livneh et al., 2010), precipitation-type classification errors could significantly impact the simulated timing of snowmelt soil infiltration in addition to model weaknesses in representing water transport as discussed above.

The improvement offered by NP_{DBT} run at 10-minute resolution compared to the *N* and *NP* scenarios run at 60-minute time steps raises two main questions regarding: *i*) limitations of the Beer's Law treatment of shortwave radiation through a discontinuous canopy; and *ii*) the time step required of direct beam canopy transmissivity to capture the mean sub-canopy shortwave irradiance over a given time period. While numerous studies have confirmed the former (e.g. Li et al., 1995; Ni et al., 1997; Nijssen and Lettenmaier, 1999; Yang et al., 2001), fewer studies

have conducted explicit sensitivity tests of the latter (e.g. Baldocchi et al., 1986; Reifsnyder et al., 1971). Sub-canopy shortwave irradiance in forests with numerous canopy gaps exhibits a general bimodal distribution as a result of sunflecks (i.e. higher mode) and shadows (i.e. lower mode) (Essery et al., 2008b) similar to what has been observed in the upper portions of continuous canopies (e.g. Norman and Jarvis, 1974; Ovington and Madgwick, 1955). Consequently, representing sub-canopy shortwave irradiance with a mean value is complicated, particularly when the median of the direct beam canopy transmissivity distribution is close to zero and the mean is sensitive to sunflecks (see Musselman et al., 2012). *Hardy et al.* (2004) suggest that choosing an optimum temporal resolution requires careful consideration of the data application. The ten-minute averages of one-minute instantaneous estimates (Figure 5a) were used in this study because this resolution was deemed adequate to capture the temporal dynamics of sunflecks on the forest floor relative to coarser time steps. *Pearcy* (1990) found that cumulative sub-canopy irradiance from sunflecks longer than 10 minutes could account for more than two-thirds of the daily shortwave irradiance. In addition, this approach was less computationally intensive and was more typical of meteorological measurement intervals than the one-minute scenario.

The presence of canopy coverage is known to decrease snow model predictive accuracy, largely as a result of errors in simulating individual surface energy flux terms (Ellis et al., 2010; Rutter et al., 2009; Sicart et al., 2004) such as shortwave (Hardy et al., 2004) and longwave radiation and their associated feedbacks with canopy elements (Pomeroy et al., 2009). There are numerous uncertainties associated with atmospheric forcing (e.g. catchment-scale cloud cover patterns), individual model equations (e.g. the empirical disaggregation of shortwave into direct

and diffuse components), and parameters (e.g. the canopy extinction coefficient). Hemispherical photography represents a method of estimating high-resolution direct beam canopy transmissivity, thus minimizing a significant source of model uncertainty. The presented methods are simple and inexpensive compared to the requirements needed to maintain long-term sub-canopy radiation monitoring stations in forested regions. In addition, transmissivity values derived from photos taken in healthy conifer forests are generally valid over long time scales. The methods could be used to improve estimates of snowmelt dynamics at individual research sites for hydrological and ecological applications.

The physical basis of the SNOWPACK model made it well suited for this study. Future work should evaluate the utility and potential differences of introducing direct beam canopy transmissivity measurements to other process-based models. Additionally, many questions remain regarding scale issues related to canopy parameters and the assumptions inherent to Beer's-type canopy radiation models, particularly when applied to areas of steep terrain and heterogeneous canopy coverage. For example, research is needed that bridges observations made at forested catchment and plot-scales to quantify hydrometeorological variability (e.g. variance) in representations of mean states and fluxes at larger scales relevant to hydrologic and climate models. Future efforts will address some of these scale issues by applying the presented methods to airborne LiDAR data (e.g. Essery et al., 2008a) with an explicit treatment of longwave radiation (e.g. Pomeroy et al., 2009) within the distributed land surface model Alpine3D (Lehning et al., 2006) and snowpack reconstruction techniques (e.g. Durand et al., 2008a; Durand et al., 2008b; Molotch, 2009; Molotch and Margulis, 2008). Toward this goal, preliminary tests conducted in the Wolverton basin of voxel aggregation of multiple-return

discrete LiDAR data (e.g. Hagstrom et al., 2010) combined with an efficient ray tracing algorithm (e.g. Hagstrom and Messinger, 2011) and look-up table shows promise for producing high-resolution, spatially distributed estimates of direct beam canopy transmissivity.

3.6 Conclusions

When canopy model parameters *canopy openness* and LAI' were obtained from satellite data at 30 m resolution and literature-based sources, respectively, the nominal model (Scenario *N*) was unable to resolve the highly variable sub-canopy snowpack dynamics. When the same two canopy model parameters were obtained from hemispherical photos (Scenario *NP*), consistently improved results were not obtained. When the nominal model was modified to accept a time series of photo-derived direct beam canopy transmissivity (Scenario NP_{DBT}), the average error in the date of snow disappearance was improved by six days. The positive biases in melt-season SWE obtained at lower elevations with scenario *N* were reduced by no less than 45% (2010) and as much as 74% (2009). The MAE of the simulated snow disappearance date was reduced by 40% in 2008, 19% in 2009, and 43% in 2010. Compared to soil moisture measurements, average improvements in the timing of snowmelt soil infiltration of 11 days were observed with the explicit consideration of direct beam canopy transmissivity. The optimum temporal resolution of the direct beam canopy transmissivity was determined to be 30-minute averages of one-minute instantaneous values; hourly averages performed no better than the *N* or *NP* scenarios and time steps finer than 30-minutes did not result in overall improvement. The model improvements gained by including time-variant photo-derived direct beam canopy transmissivity were greatest in 2010; a year with high SWE, a late melt-season, and low spring

cloud cover. The results illustrate the important contribution of direct beam shortwave radiation to the sub-canopy melt-season snowpack dynamics. The estimation of time-variant direct beam canopy transmissivity thus minimizes a significant source of snowmelt model uncertainty at the point-scale in forested regions.

Chapter 4. Inter-annual snow accumulation and melt patterns in forested and alpine terrain

This chapter evaluates distributed snow cover dynamics for the same time period and general region presented in Chapters 2 and 3 with a land surface model evaluated against multi-scale observations. The work supplements and builds upon the results of the previous two chapters. In Chapter 2, canopy effects on snowmelt were found to vary as a result of distinct inter-annual differences in the timing and magnitude of maximum SWE. This chapter examines whether these and similar inter-annual snowmelt trends are detectable across larger gradients of elevation and vegetation cover. In Chapter 3, the nominal canopy model was found to under-estimate seasonal snowmelt rates when maximum SWE occurred late in the spring. This chapter assesses inter-annual and seasonal patterns in the relative distribution of simulated catchment SWE. The sensitivity of the results to known limitations in the forcing data and the canopy model is discussed.

Extensively validated model simulations of snow depth and SWE are then used to evaluate seasonal and inter-annual patterns of accumulation and melt. This approach is particularly useful to evaluate snow cover dynamics in places where few or no validation

measurements are available. For example, observations of SWE and depth are generally limited to small areas of seasonally snow-covered mountainous regions. Very few stations observe dynamics in steep alpine areas that contain the most SWE for the longest duration or at lower elevations where snow cover is transient or ephemeral, despite these areas contributing a large fraction of seasonal snow water resources (Hamlet et al., 2005). As a result, trends and patterns of snow deposition and melt in ephemeral snow zones are poorly documented, but this zone is expected to shift upward in elevation under warmer climate conditions and influence significantly larger areas and a greater fraction of regional water resources (Minder, 2010). The validated physically based snow model is a useful tool to evaluate seasonal and inter-annual trends in these regions.

Two primary research questions motivate this study: 1) *How well can a land surface model simulate inter-annual snow cover properties over a large and physiographically diverse area?* and 2) *How do inter-annual differences in seasonal meteorology impact the relative distribution of SWE and how are these patterns related to forest cover, elevation, and terrain?*

4.1 Study domain and observations

4.1.1 The Kaweah River basin

The work is conducted over a rectangular grid encompassing the 1,085 km^2 Kaweah River basin on the western slope of the southern Sierra Nevada, California, USA (36.4ºN, 118.6ºW) (Figure 4.1). The elevation of the catchment ranges from over 3800 m in the western peaks of Sequoia National Park to 250 m in the small town of Three Rivers, CA. The catchment represents ~ 72% of the contributing area of Lake Kaweah, formed by a terminus dam and

largely used for flood control of downstream agricultural and municipal lands (USGS, 2012). The land cover and climate vary significantly with elevation. Approximately 98% of the Kaweah River basin is comprised of four land cover types: conifer forest (58%), shrub (26%), bare soil / rock (10%), and grass / tundra (4%) (Figure 4.1). Lower elevation (< 1800 m asl) foothills are a mix of grassland, chaparral shrub and oak woodlands characterized by mild, wet winters and hot, dry summers. Winter snow cover at these lower elevations is intermittent and the average annual precipitation is 660 mm (NPS, 2012). Conifer forest stands of various species composition and density dominate the middle elevations between 2000 m and 3000 m asl, including red fir, Jeffrey pine, white fir, lodgepole pine, and Giant Sequoia. The climate of the middle elevations is characterized by cool, seasonally snow-covered winters and warm, dry summers. Average annual precipitation at these middle elevations is ~ 1080 cm (NPS, 2012). The forest vegetation of the sub-alpine zone, between 3000 m and 3600 m asl, is sparse and consists of scatter stands of lodgepole and foxtail pines. Winter precipitation at these upper elevations is not measured. Land cover at the highest elevations is composed of rock and alpine vegetation and snow cover persists from November to July in most years.

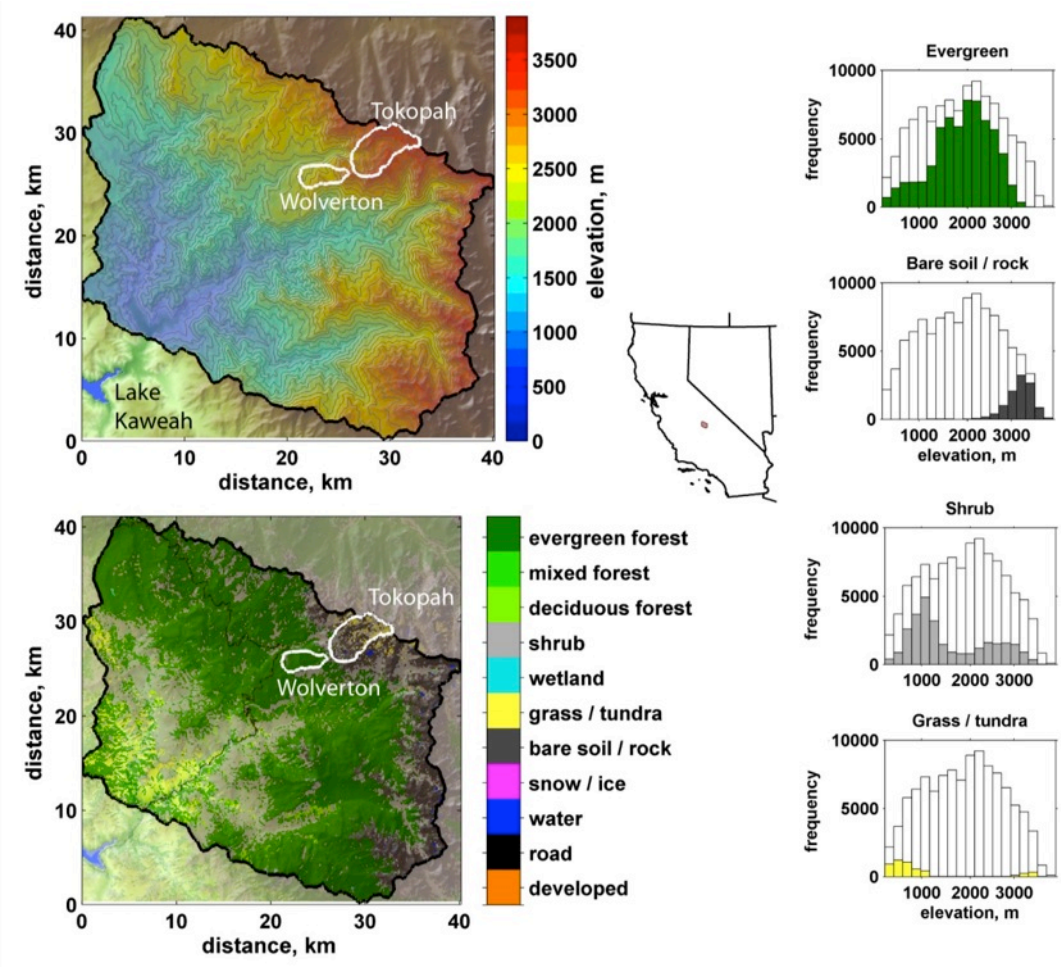

Figure 4.1. The elevation and land cover distribution of the 1,085 km^2 Kaweah River basin (outlined in black) on the western side of the southern Sierra Nevada, California. The forested 7.22 km^2 Wolverton and largely alpine 19.1 km^2 Tokopah sub-basins are outlined in white. Approximately 98% of the Kaweah River basin is comprised of four primary land cover types (right). The figures at right highlight the elevation distribution of the primary land cover types relative to the distribution of the Kaweah River basin.

4.1.1.1 Wolverton sub-basin

The 7.22 km^2 forested Wolverton sub-basin is described in detail in Chapters 2 and 3. It is representative of regional mid-elevation mixed conifer forests with tall, old growth trees with an average canopy density of 65%, interspersed with small grassy meadows. The location of the Wolverton sub-basin within the greater Kaweah River basin is indicated in Figure 4.1.

4.1.1.2 Tokopah sub-basin

The 19.1 km^2 Tokopah basin is representative of small headwater (i.e. upper elevation) basins in the southern Sierra Nevada having poorly developed soils, sparse vegetation, limited groundwater storage, and rapid hydrologic response (Tonnessen, 1991). The elevation of this gauged basin ranges from 2629–3487 m asl, with numerous alpine lakes, granitic bedrock, and forest cover restricted to small areas of the valley floor. Figure 4.1 indicates the location of the Tokopah basin within the greater Kaweah River basin.

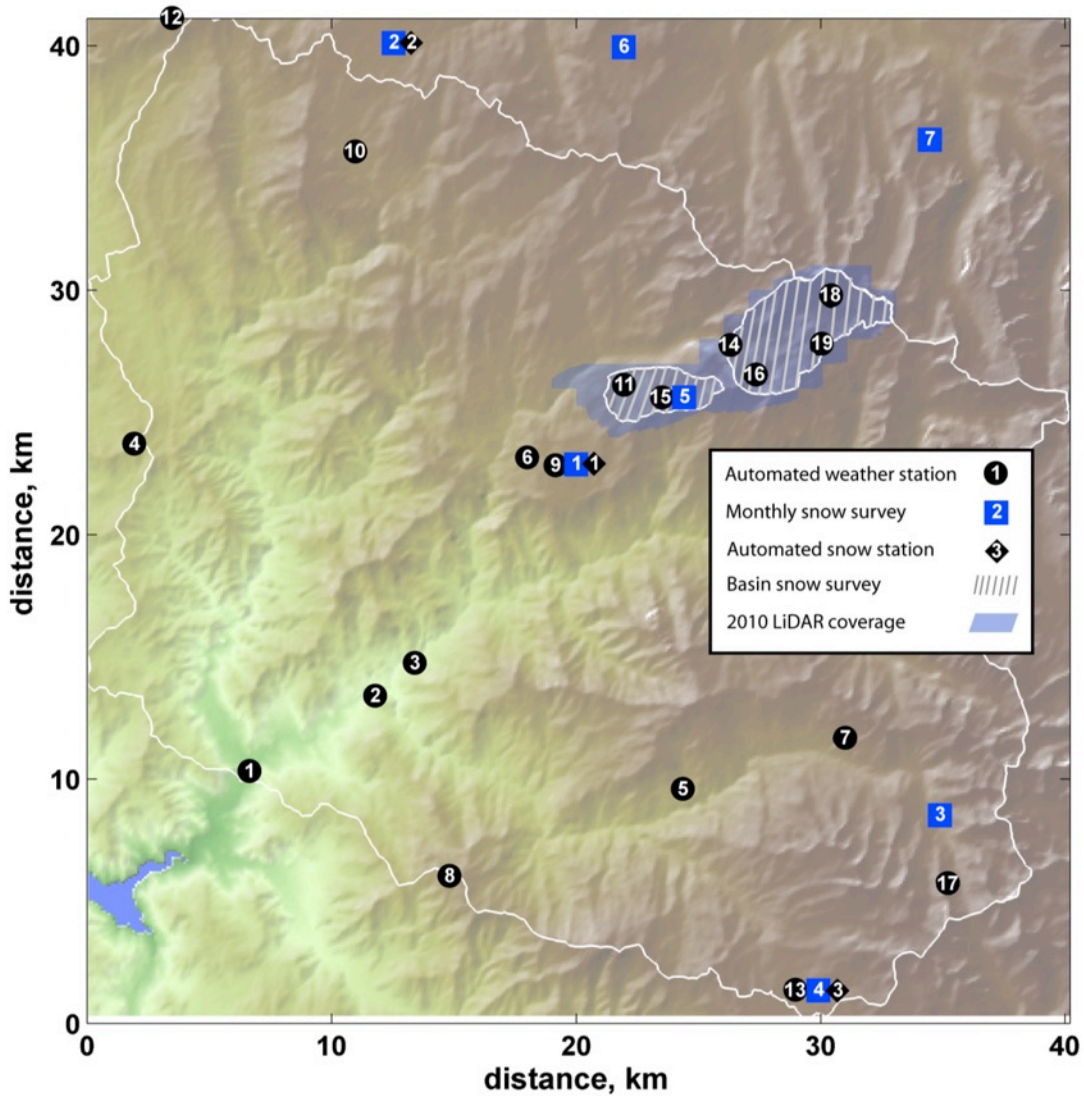

Figure 4.2. Locations of 19 automated weather stations, seven monthly snow surveys, three automated snow stations, repeated basin-scale manual snow surveys, and the footprint of a 2010 airborne LiDAR snow survey within and surrounding the greater Kaweah River basin. Station numbers, ranked by elevation, correspond to those in Table 4.1.

4.1.2 Meteorological measurements

Hourly meteorological observations for the three water years (2008, 2009 and 2010) were available from 19 regional stations maintained by nine different state and government agencies and research institutes (Figure 4.2 and Table 4.1). Not all stations were continuously operational

and not all stations reported the same meteorological variables. Table 4.1 provides information about the stations and their measured variables. Air temperature was recorded at 15 stations and wind speed and relative humidity were each measured at 13 stations. The station coverage spanned a large elevation range (263 m to 3288 m asl) and spatial extent of the basin (Figure 2). Six stations in the Kaweah River basin measured precipitation. The Ash Mountain station at 527 m asl provided the only low elevation precipitation measurements. The Lower Kaweah station (heated, shielded tipping bucket), and the Atwell, Giant Forest, Bear Trap Meadow, and Hockett Meadow stations (storage gauges) are located within an elevation band of 1926 m to 2592 m asl. Data from the Hockett Meadow station were not used because significant delays in the timing of measured precipitation and large post-event spikes were indicative of gauge error. The exclusion of the Hockett Meadow station limited the number of precipitation gauges at middle elevations to four within a much narrower elevation range (1926 to 2073 m asl) with no measurements available at higher elevations. Figure 4.3 shows the daily average temperature and accumulated weekly precipitation for 01 October 2007 to 30 September 2010 measured at the lower elevation Ash Mountain station and at middle elevations as averaged over the four stations. The high seasonality of annual precipitation and distinct differences in the precipitation magnitude and the seasonal temperature range between the lower and middle elevations is evident (Figure 4.3). The catch efficiency of the regional precipitation gauges was accounted for as described in Chapter 3.

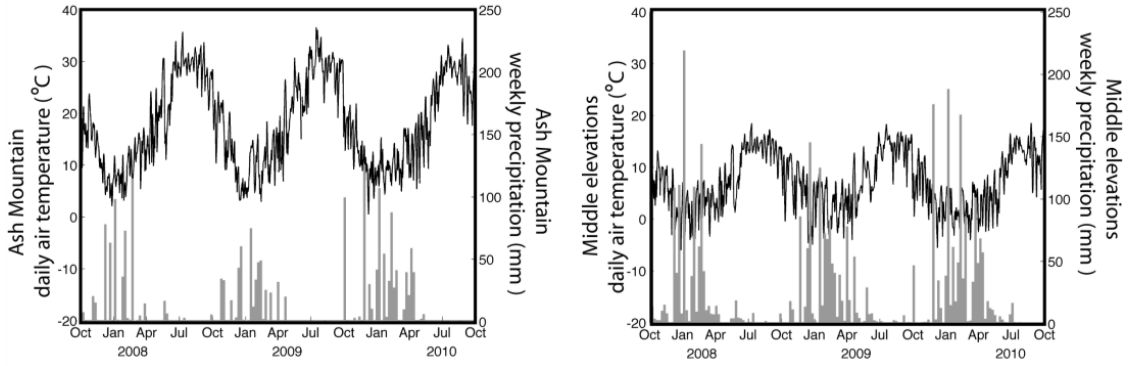

Figure 4.3. Measured weekly cumulative precipitation (gray bars) and daily average temperature (black line) at the lower elevation Ash Mountain station (527 m asl) (left) and averaged at four mid-elevation stations (1926 m to 2073 m asl) (right).

Downwelling shortwave and longwave radiation unobstructed by vegetation and surrounding terrain were measured at the Topaz Lake meteorological station in the Tokopah basin. These measurements were required by a radiosity model to estimate the incoming above-canopy irradiance over the model domain. A description of the radiosity model is provided in Section 4.2.2.

Table 4.1. Meteorological station and snow measurement details. Station numbers are ranked by station elevation and correspond to those mapped in Figure 4.2. The variables measured at each location are listed: air temperature (Ta), relative humidity (RH), wind velocity (wv), precipitation (ppt), snow water equivalent (SWE), and snow depth (depth).

#	Station name	Elevation (m)	Measured variables*	Operating agency
Automated met. stations				
1	D0117	263	Ta, RH, wv	APRSWXNET
2	C4177	378	Ta, RH, wv	APRSWXNET
3	Ash Mountain	527	Ta, RH, wv, ppt	NPS
4	Shadequarter	1323	Ta, RH, wv	CDF
5	Wolverton	1598	Ta, RH, wv	NPS
6	Lower Kaweah	1926	Ta, RH, wv, ppt	NPS
7	Atwell	1951	ppt	USACE
8	Case Mountain	1967	Ta, RH, wv	BLM
9	Giant Forest	2027	Ta, ppt	USACE
10	Bear Trap Meadow	2073	ppt	USACE
11	Wolverton Meadow	2229	Ta, RH, wv	SNRI
12	Park Ridge	2299	Ta, RH, wv	NPS
13	Hockett Meadows	2592	ppt	USACE
14	Marble Fork	2626	Ta	ERI
15	Panther Meadow	2640	Ta, RH, wv	SNRI
16	Emerald Lake	2835	Ta, RH, wv	ERI
17	Farewell Gap	2896	Ta	USACE
18	Topaz Lake	3232	Ta, RH, wv, SW, LW	ERI
19	M3	3288	Ta, RH, wv	ERI
Automated snow stations				
1	Giant Forest	1951	SWE	USACE
2	Big Meadows	2317	SWE	USACE
3	Farewell Gap	2896	SWE, depth	USACE
Monthly snow surveys				
1	Giant Forest	1951	SWE, depth	NPS
2	Big Meadows	2317	SWE, depth	CADWP
3	Mineral King	2439	SWE, depth	NPS
4	Hockett Meadow	2592	SWE, depth	NPS
5	Panther Meadow	2622	SWE, depth	NPS
6	Rowell Meadow	2698	SWE, depth	KRWA
7	Scenic Meadow	2942	SWE, depth	KRWA

*Meteorological variables used in this study.
APRSWXNET: Automatic Position Reporting System as a Weather NETwork
NPS: National Park Service (Sequoia and Kings Canyon National Parks)
CDF: California Department of Forestry
USACE: United States Army Corps of Engineers
BLM: Bureau of Land Management
SNRI: Sierra Nevada Research Institute, University of California Merced
ERI: Earth Research Institute, University of California Santa Barbara
CADWP: California Department of Water and Power
KRWA: Kaweah River Water Association

4.2 Methods

4.2.1 The Alpine3D land surface model

Alpine3D (Lehning et al., 2006) is a land surface model with a particular emphasis on snow process representation. It has been used in the study of mountain hydrological processes in Switzerland and Austria (e.g. Groot Zwaaftink et al.; Michlmayr et al., 2008; Mott et al., 2008) including projections of future snow and runoff regimes (e.g. Bavay et al., 2009; Kobierska et al., 2011). A brief summary of the model is presented here and the reader is referred to these previous studies for detailed descriptions. At the core of Alpine3D is the one-dimensional SNOWPACK model presented in Chapter 3. The vegetation – snow – soil model includes the parameterized canopy module presented in Appendix A and used in the nominal model scenarios in Chapter 3. At each grid cell, a one-dimensional snow column composed of an arbitrary number of layers varies according to the grid cell-specific atmospheric forcing. Meteorological station data were statistically interpolated to determine the forcing variables at each grid cell. The interpolation methods are described in the following section.

4.2.2 Meteorological interpolation methods

Meteorological input (e.g. precipitation, air temperature, wind speed, relative humidity) measured at point locations were spatially distributed using the MeteoIO model (available online: https://slfsmm.indefero.net/p/meteoio). The model permits user-specified methods of filtering, resampling and spatially interpolating meteorological data. It is based on the MicroMet model of *Liston and Elder* (2006b) and is used in this study to establish physically appropriate above-canopy atmospheric forcing for each grid cell. In MeteoIO, the user can specify a

hierarchy of interpolation methods for each variable and statistical criteria to determine the optimal interpolation method.

The result of each interpolation is evaluated through the use of a variable-specific rating method (R^2) that accounts for the number of available stations as well as the quality of the data. For each time step and each interpolated variable, the algorithm that receives the highest score is used to interpolate that variable. Note that the interpolation algorithms are time-independent such that all parameters and variables that are automatically calculated are done so for each model time step with no memory of previous performance. Since elevation can have a profound influence on many of the meteorological variables, several of the interpolation methods (briefly described below) use (linear) elevation trends. The slope of the linear relation is computed from the available station data. To account for outliers in the data, if the correlation between the input data and the computed linear regression is less than 0.7, the regression will be re-calculated with one less point, cycling through all points. The best result is then used. Given the large number of meteorological stations in the Kaweah basin, this dynamic interpolation model is expected to be more accurate than the use of a single algorithm or constant lapse rate used in similar studies.

4.2.2.1 Air temperature

Air temperature was interpolated over the domain using an inverse distance weighting (IDW) algorithm with elevation detrending / reprojection. The lapse rate was computed from the data as described previously. If the R^2 value was less than 0.6 for all iterations, a specified lapse rate of -0.008°C m^{-1} was used. If results from the IDW-lapse algorithm were still poor ($R^2 < 0.7$), a simple linear regression with the specified constant lapse rate was computed and the best result from all interpolation methods was used to distribute air temperature over the domain.

4.2.2.2 Relative humidity

Relative humidity was interpolated as *Liston and Elder* (2006b) by computing the dew point temperature for each station point and interpolating with the same methods used for air temperature, described previously.

4.2.2.3 Wind speed

Wind speed was interpolated using a simple weighting method that accounts for terrain curvature and slope (see Liston and Elder, 2006b). However, because wind transport of snow was not considered in this study, the IDW-lapse algorithm may be sufficient to represent spatial wind speed fields.

4.2.2.4 Precipitation

The IDW-lapse algorithm was used to initialize the precipitation field. After initialization, grid cells that were at or below 0°C were modified according to the method described in *Magnusson et al.* (2011) and *Huss et al.* (2008). The method is a parametric approach that uses terrain curvature to simulate sloughing and avalanching of snow from steep slopes to flatter valley locations and has been shown to be successful in steep, alpine terrain.

4.2.2.5 Incoming shortwave radiation

A three-dimensional radiative transfer (i.e. *radiosity*) model was employed that treats terrain as a Lambertian emitter/reflector surface and the sky as an emitter surface of zero reflectivity (Helbig et al., 2009). The model required that incoming shortwave radiation be measured at a location where it was unobstructed by surrounding terrain or forest cover. The

model computed the direct and diffuse atmospheric corrections, accounting for the effects of local cloud cover. The respective contributions of the direct and diffuse components are modified through the consideration of shade and reflected irradiance from surrounding grid cells. Currently, the radiosity model does not account for cloud cover spatial heterogeneity; atmospheric corrections were computed at a single meteorological station and uniformly applied to the full domain. Solar radiation provided to the model was measured at the Topaz Lake station in the Tokopah basin. The three-year dataset is described in Chapters 2 and 3 and was well correlated (R = 0.93) with solar radiation measurements made at middle elevations in the Kaweah River basin (see Chapter 2).

4.2.2.6 Incoming longwave radiation

Longwave radiation was also measured at the Topaz Lake station. Atmospheric emissivity at the station was computed using the local air temperature and relative humidity. The emissivity was extrapolated across the model domain using a sky view approach defined in *Lehning et al.* (2006), which allows valley locations with reduced sky view to have higher thermal irradiance than ridge locations with more sky view. The approach accounted for the modification of incoming atmospheric longwave radiation by the contribution of that emitted from surrounding terrain. The extrapolated emissivity was then reconverted to longwave irradiance using the grid cell-specific interpolated air temperature described previously.

4.2.3 Simulations

Alpine3D was run over the greater Kaweah River basin (Figure 4.1) at 100 m horizontal grid spacing and hourly resolution for three water years (i.e. 01 October 2008 to 30 September

2010). The land cover type (Figure 4.1) and forest canopy density was obtained from the 2001 National Land Cover Dataset (Homer et al., 2004). The native 30 m resolution of these products was up-scaled to 100 meters to match the model grid spacing; land cover type was resampled using a nearest-neighbor approach and canopy density was resampled with a cubic convolution computed on the nearest 16 cells. Simulations were run over a gridded domain composed of 412 rows and 402 columns, rather than only on the basin itself. The larger domain encompasses the Kaweah River basin and also includes additional meteorological and SWE measurement stations just beyond the basin boundaries (Figure 4.2). Model output at the daily scale included distributed estimates of SWE, snow depth, surface temperature, and short- and long-wave surface irradiance.

4.2.4 Model evaluation methods

Model results were evaluated against a suite of multi-scale manual and automated observations. This section describes the measurements.

4.2.4.1 Automated SWE and depth measurements

Daily SWE observations were obtained from three automated stations in the region (see Table 4.1 and Figure 4.2). One of the three stations also measured snow depth. Modeled snow depth and SWE fields were evaluated against these station observations. In addition to these three point measurements, the Wolverton sub-basin includes the extensive network of ultrasonic snow depth sensors described in Chapters 2 and 3. The four research sites each include six snow depth sensors and each site falls within a different 100 m x 100 m grid cell. The mean snow depth computed from six sensors at each site provided a robust estimate of the snow depth, and

thus the model error, at four grid cells in the forested Wolverton basin. Snow depth error values were computed as the difference between modeled and measured values when the simulated depth occurred beyond the observed range, otherwise the error was assumed to be negligible. The date of snow disappearance measured by the automated sensors also served as a useful metric of melt-season model performance.

4.2.4.2 Repeated manual SWE and depth measurements

In addition to automated hourly measurements, monthly manual SWE measurements were made as part of an extensive, multi-agency effort to monitor regional snow water resources (Table 4.1). Multiple SWE measurements made with Federal snow tubes are averaged over an area approximately equal to the model grid spacing. The survey measurements thus provide a SWE estimate that is more representative of the average value within a corresponding model grid cell than a single automated station measurement, but at monthly rather than daily time scales. Manual monthly SWE and depth surveys were conducted at six locations within the model domain between the months of February and May. Modeled snow depth and SWE were evaluated against observations made at the seven monthly manual survey locations.

4.2.4.3 Distributed snow surveys

Intensive ground-based surveys of the Wolverton and Tokopah sub-basins were conducted for two winter seasons (water years 2008 and 2009) to document SWE and depth distribution in these forested and alpine environments. Distributed snow depth surveys of the forested Wolverton basin were conducted during three annual campaigns timed to coincide with seasonal accumulation (mid-February), maximum accumulation (mid-March), and melt (late-

April). A total of six surveys were conducted in the Wolverton sub-basin. The 2009 Tokopah surveys were similarly designed to capture seasonal snow distribution during accumulation (early-March), maximum accumulation (early-April), and melt (mid-May). In 2008, the Tokopah sub-basin was only surveyed at maximum accumulation (early-April).

Segmented graduated aluminum probes were used to measure snow depth at pre-determined locations (i.e. waypoints). Surveyors navigated to the waypoints using Geographic Position System (GPS) units. At each waypoint, three snow depth measurements each separated by five meters were made along a north-south axis. In 2008, Wolverton basin waypoints were spaced at 100 m. This spacing was increased to 250 m in 2009 to increase spatial coverage. Because similar surveys were conducted in the Tokopah basin in 1997 and 1998, for consistency and to promote comparison, locations where measurements were repeated for the earlier surveys were used as waypoints for the 2008 and 2009 surveys. Figure 4.4 illustrates the locations of measured snow depths for each survey. A total of 1480 waypoint measurements (4440 single depth measurements) were recorded during the two years. In addition, snow density and stratigraphy was recorded at multiple snow pit locations for each survey (see Figure 4.4). An undisturbed snow face was excavated to ground and snow density in duplicate columns was measured in 10 cm vertical intervals by weighing snow samples acquired with a 1000 cm^3 cutter. In total, measurements of 25 snow pits were made in the two basins for the two years.

The average snow density was used to estimate SWE at depth measurement locations, which represent the average of three depth measurements. Simulated SWE at model grid-elements corresponding to the waypoint locations were then directly evaluated against the measurements. The potential uncertainty associated with the measurement / model scale disparity

is not considered here.

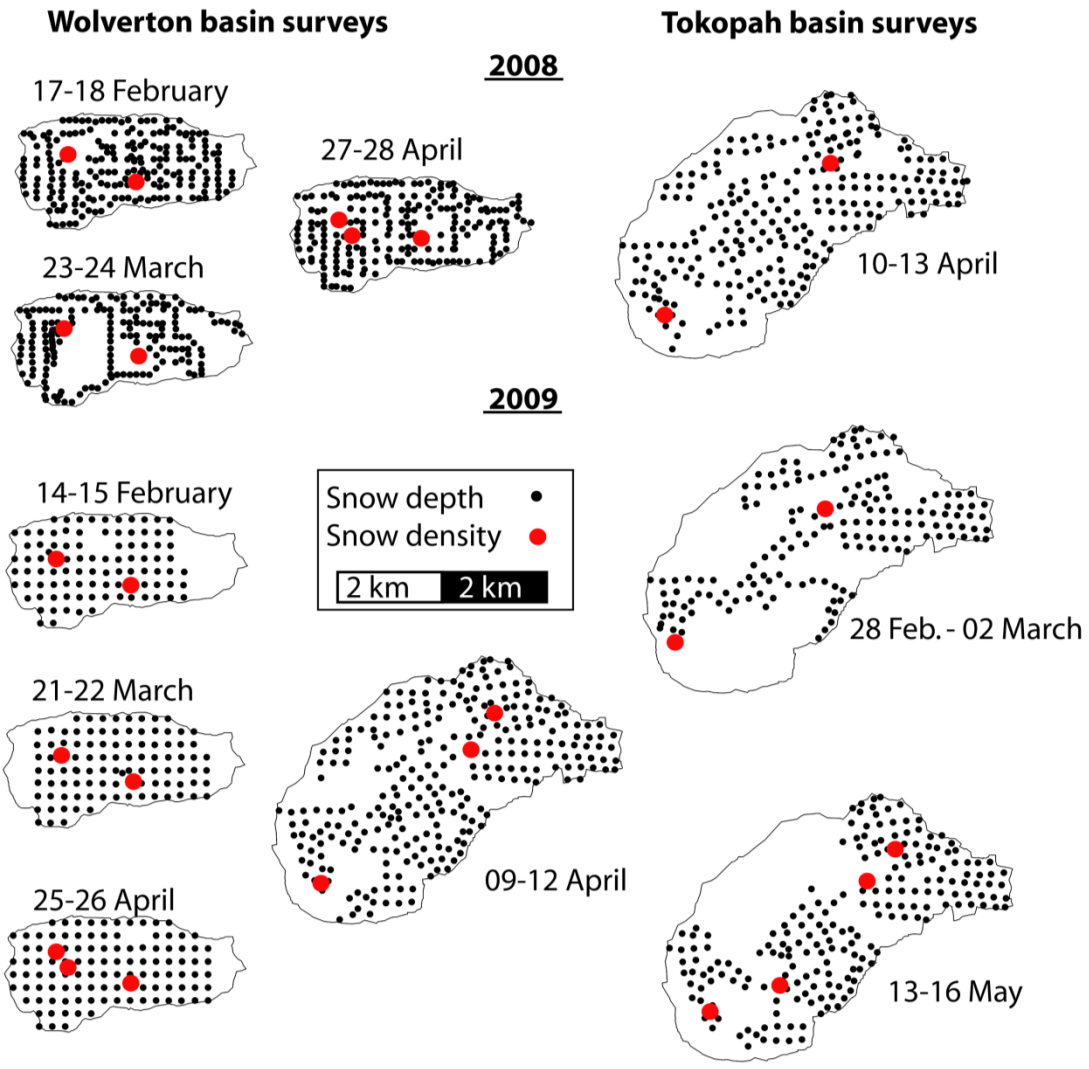

Figure 4.4. Map illustrating snow depth and density measurements in the Wolverton and Tokopah basins in 2008 and 2009.

4.2.4.4 LiDAR snow depth

Airborne LiDAR surveys are arguably superior to traditional mapping and surveying techniques because of the high measurement accuracy, density, and the relatively large spatial extent. The National Center for Airborne Laser Mapping (NCALM) flew two scanning LiDAR

flights over the greater Wolverton and Tokopah sub-basins on 22-23 March, 2010 (snow-on) and in August, 2010 (snow-off) (see Figure 4.2). The average point densities for the snow-on and snow-off flights were 8.2 and 10.0 points m^{-2}, respectively. Data filtering was conducted to separate ground / snow surface returns from non-surface returns (e.g. vegetation returns). The non-surface returns were removed and the surface point elevations were interpolated to a raster DEM with one-meter horizontal grid spacing (see thorough review of filtering algorithms and associated uncertainty by Meng et al., 2010). The same filtering algorithms were used on data from both flights and the surface elevation difference (i.e. '*snow-on heights – snow-off heights*') produced a raster representing the snow depth for the snow-on flight date over a spatial domain determined by the overlap of the two flight footprints.

4.3 Measurement results

The snow depth, density, and SWE measurement results highlight inter-annual trends in accumulation and melt patterns both in time and space. Measurements made at one scale can be compared to those made at a larger scale. Such comparisons can be helpful to understand scale relationships of SWE and to identify limitations and/or utility of observations made at a particular scale to infer dynamics made at another.

4.3.1 Distributed snow surveys

Snow survey results are listed in Table 4.2. The measurements made in 2008 and 2009 indicate similar seasonal and inter-annual trends documented previously in Chapters 2 and 3. For brevity these observations are not discussed here. An excellent example of scale relationships is seen between snow depth measured at the basin-scale as obtained by repeated surveys and the

snow depth measured by the network of automated sensors. The survey observations (hundreds of point measurements made over a large area at a discrete time) were compared to snow depth measured by the sensors (26 point measurements at hourly time steps). Figure 4.5 compares the range, mean, and standard deviation of snow depth from repeated Wolverton surveys to the observations of snow depth from the depth sensor network. The comparison is made for three surveys each in 2008 and 2009.

Table 4.2. Summary statistics of the Wolverton and Tokopah snow surveys in 2008 and 2009. Missing data (-) values indicate no survey was conducted on that date. Figure 4.4 includes the exact dates of each survey.

Snow survey results	Wolverton basin			Tokopah basin		
2008	***Feb.***	***Mar.***	***Apr.***	***Mar.***	***Apr.***	***May***
mean depth, cm	190	190	115	-	202	-
standard deviation, cm	30	37	58	-	88	-
maximum depth, cm	253	353	314	-	523	-
density, ± std., kg m^{-3}	364±24	399±12	439±12	-	445±65	-
2009	***Feb.***	***Mar.***	***Apr.***	***Mar.***	***Apr.***	***May***
mean depth, cm	156	122	81	219	214	117
standard deviation, cm	34	35	46	57	95	79
maximum depth, cm	242	199	179	405	484	393
density, ± std., kg m^{-3}	262±9	333±30	415±5	302±6	372±57	435±30

The network of 26 ultrasonic snow depth sensors captured the basin mean snow depth as determined from distributed survey measurements with accuracy greater than 85%. The results indicate that when sensors are carefully located to sample a basin's range of elevation, aspect, and forest cover known to engender variability in snow depth, the observations may negate the need for basin-scale surveys by capturing the larger-scale mean and variability. *A priori* knowledge of snow distribution may thus be of great utility when determining the most efficient and effective sensor placement that minimizes the number of sensors required to estimate the mean and variance of basin-scale snow depth. For example, LiDAR data provide a level of detail necessary to evaluate basin-scale snow depth variability with a high degree of accuracy. A similar comparison of the 2010 depth sensor measurements to the snow depth measured by the

LiDAR flight, masked to the Wolverton basin extent, indicates that the depth sensor network captured the basin mean depth to within a 3% error (Figure 4.5). The LiDAR measurement results from the Wolverton and Tokopah sub-basins are presented below.

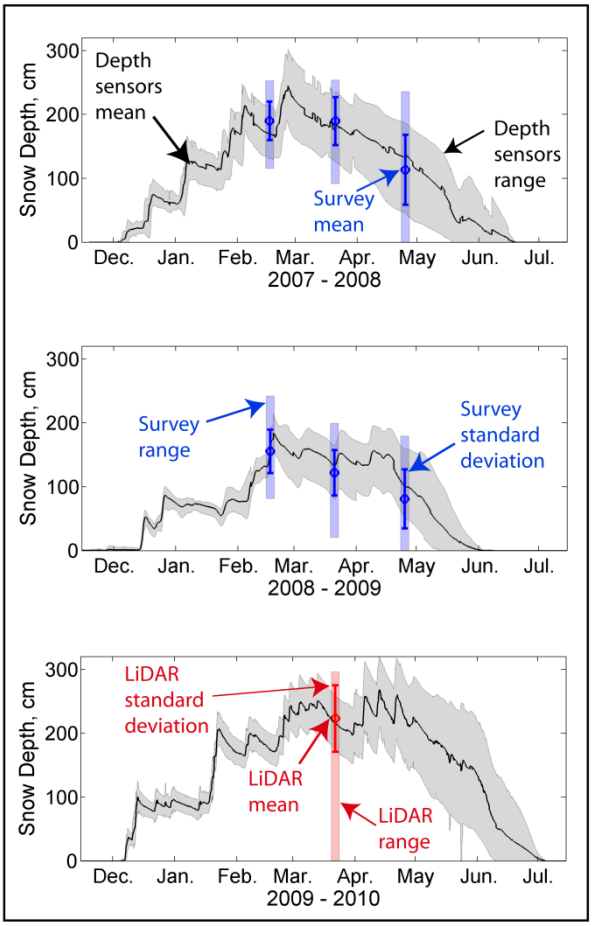

Figure 4.5. Comparison of the mean and range of snow depth measured by the network of 26 ultrasonic sensors in the forested Wolverton basin and the range, mean, and standard deviation (std.) of snow depth measured from the repeated catchment-scale surveys in water years 2008 (top) and 2009 (middle) and depth measured by the LiDAR flight in 2010 (bottom).

4.3.2 LiDAR snow depth

The mean LiDAR-derived snow depth in the Wolverton basin on 23 March 2010 was

211±55 cm. The mean Tokopah snow depth was 279±110 cm. In both basins the median snow depth was within 1% of the basin mean depth, indicating limited influence of outliers (e.g. exorbitantly high snow depths) on basin mean snow depth. The standard deviation of the snow depth values in the forested Wolverton basin (26% of basin-mean) and the largely alpine Tokopah basin (39% of basin-mean) suggests that distinctly different physical processes impact the snow depth and its variability in the two basins.

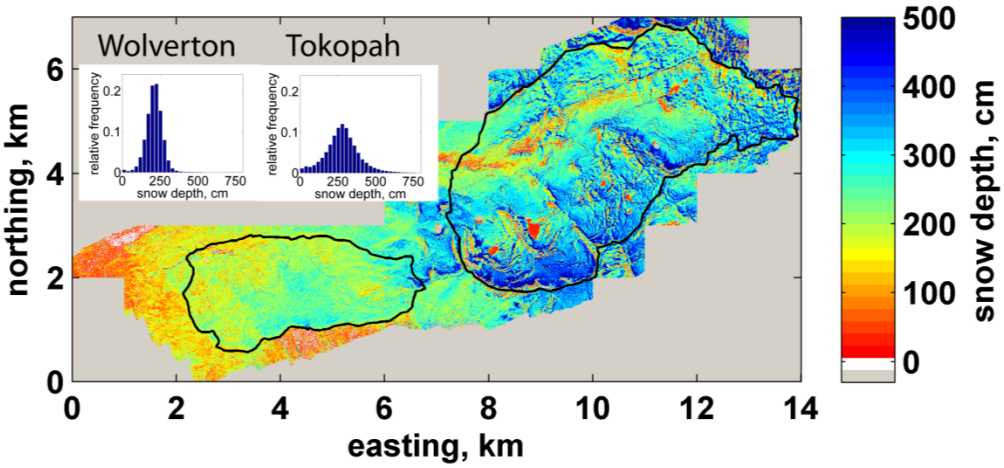

Figure 4.6. LiDAR-derived snow depth over the Wolverton and Tokopah basins.

While LiDAR provides an immense level of detail on the distribution of snow depth in these alpine and sub-alpine environments, the depth data at the time of a single flight represents only a snapshot in time and does not capture the temporal dynamics of this variability. In Section 4.4, the Alpine3D model is used to evaluate how the variability may change in both time and space. First, the accuracy of the land surface model to simulate these local and regional processes must be tested. In this context, the high-resolution of the LiDAR data was useful to evaluate model performance as well as sub-grid variability resulting from the scale discrepancy between the model and measurements.

4.3.3 Regional point-scale SWE and depth measurements

Manual measurements of snow depth and SWE from regional surveys conducted monthly at seven locations in and surrounding the Kaweah River basin are provided in Table 4.3. SWE and depth from the three automated stations are presented and discussed in Section 4.4.

Table 4.3. Snow depth and SWE data from monthly manual surveys in the region. Data available online: http://cdec.water.ca.gov/cgi-progs/snowQuery_ss. Surveys were conducted on approximately the first day of each listed month; months when surveys were not conducted are indicated (-).

#	Station name	2008								2009								2010							
		depth, cm				SWE, mm				*depth, cm*				SWE, mm				*depth, cm*				SWE, mm			
		Feb.	Mar.	Apr.	May	Feb.	Mar.	Apr.	May	Feb.	Mar.	Apr.	May	Feb.	Mar.	Apr.	May	Feb.	Mar.	Apr.	May	Feb.	Mar.	Apr.	May
1	Giant Forest	99	216	114	5	295	607	493	20	91	122	102	91	348	582	455	279	142	188	155	152	450	640	726	668
2	Big Meadows	203	218	157	-	668	879	802	-	71	152	107	-	224	516	513	-	155	208	178	-	495	757	876	-
3	Mineral King	-	216	145	30	-	762	714	155	71	137	86	36	279	373	368	198	145	234	168	142	432	724	671	653
4	Hockett Meadow	-	264	175	114	-	533	945	643	-	-	117	58	-	-	554	312	-	216	211	183		671	892	1128
5	Panther Meadow	-	287	234	178	-	1245	1115	889	122	229	198	173	404	826	861	732	236	282	257	282	638	965	1156	1394
6	Rowell Meadow	183	-	157	-	505	-	808	-	79	-	135	-	284	-	599	-	168	-	183	-	478	-	798	-
7	Scenic Meadow	165	-	140	-	493	-	620	-	76	-	135		239	-	554	-	152	-	165	-	467	-	699	-

4.4 Alpine3D model results and discussion

The model provides spatially distributed estimates of snow properties. Here, model simulations of snow depth and snow water equivalent are evaluated at daily time steps (1200 local time). Examples of the simulated snow depth (Figure 4.7) and SWE (Figure 4.8) fields on 01 April, 01 May, and 01 June for each of the three years are provided. In general, the monthly snapshots highlight seasonal and inter-annual variability in melt-season snowpack dynamics similar to the measurement and model results presented in Chapters 2 and 3.

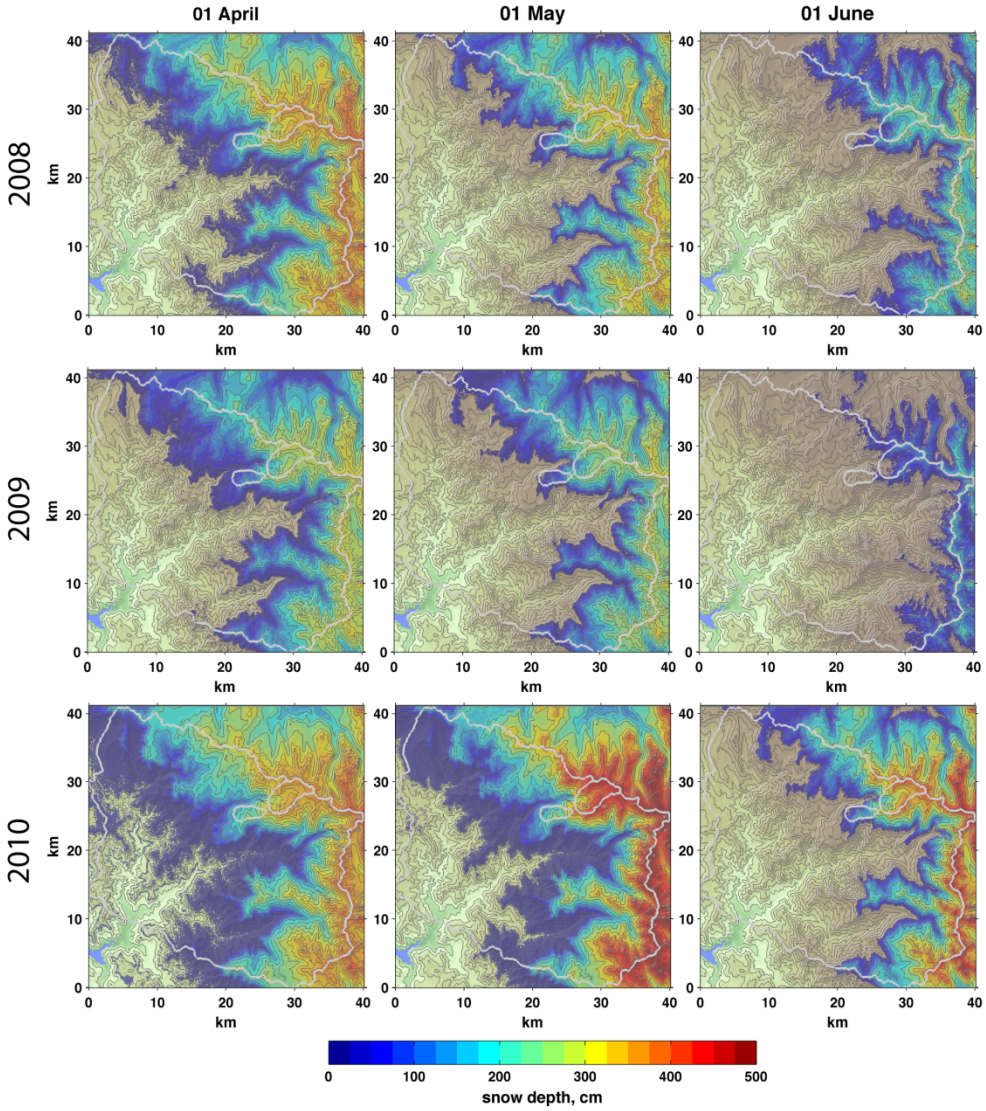

Figure 4.7. Alpine3D simulated snow depth fields over the greater Kaweah River basin on the first day of the months of April, May, and June for years 2008, 2009, and 2010. The Tokopah, Wolverton, and Kaweah River basins are outlined and elevation contours correspond to those in Figure 4.1.

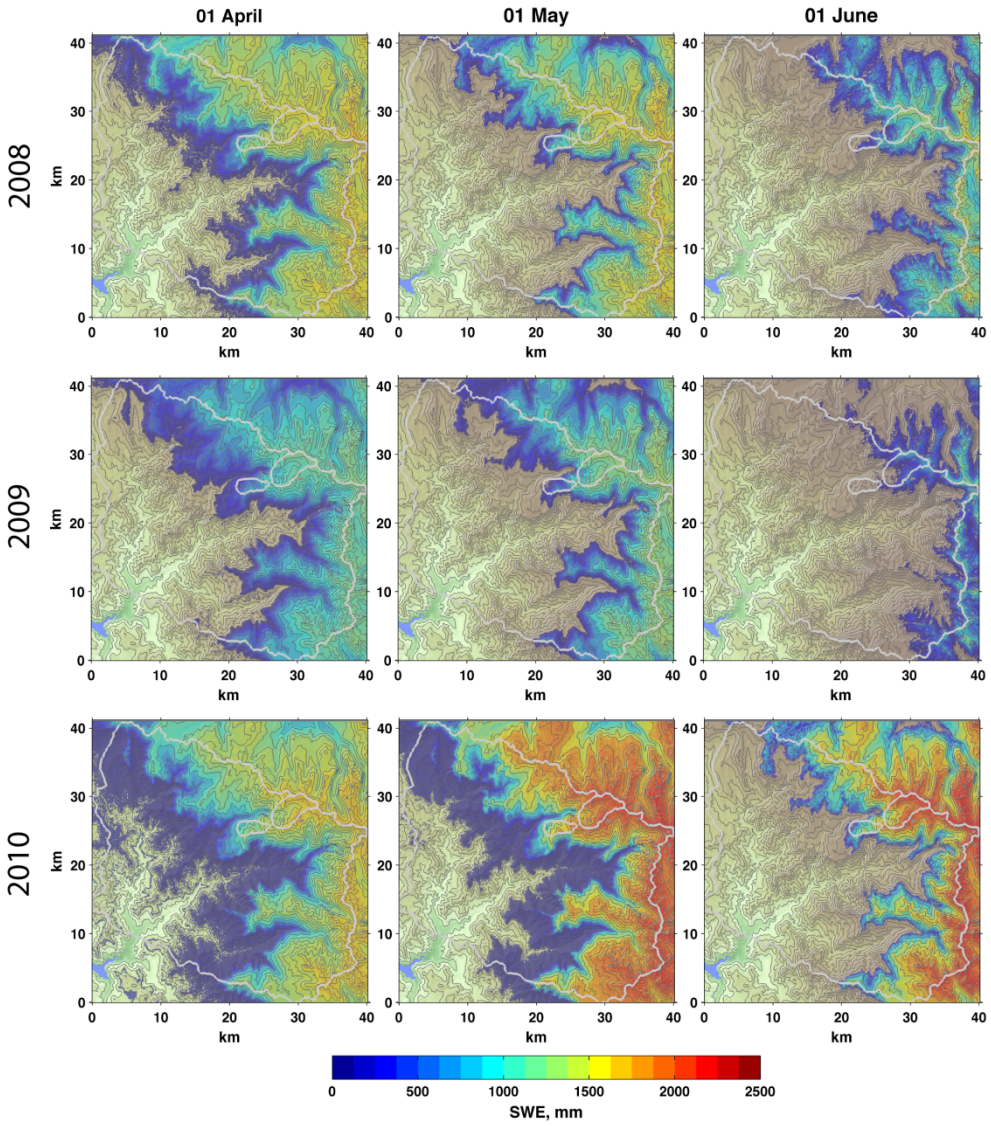

Figure 4.8. Alpine3D simulated snow water equivalent (SWE) over the greater Kaweah River basin on the first day of the months of April, May, and June for years 2008, 2009, and 2010. The Tokopah, Wolverton, and Kaweah River basins are outlined and elevation contours correspond to those in Figure 4.1.

In this section, the distributed results are quantitatively evaluated against measurements. Alpine3D snow depth and SWE results are evaluated against measurements made at the multiple scales described in Section 4.3: i) point-scale automated stations, ii) multiple automated stations

within a single model grid cell, iii) multiple manual measurements (repeated monthly) made within single grid cells, iv) basin-scale manual point measurements, and v) basin-scale distributed LiDAR measurements. The snow depth model results are first evaluated in Section 4.4.1, followed by the SWE results in Section 4.4.2. Finally, the inter-annual patterns are analyzed in Section 4.4.3.

4.4.1 Snow depth

4.4.1.1 Point-scale snow depth analysis

The highest elevation automated snow station, and the only snow station outside of the Wolverton sub-basin to measure hourly snow depth, was at Farewell Gap (Table 4.1; Figure 4.2). The average model snow depth errors, computed on days when either or both of the modeled and measured values were nonzero, were +2.8 cm, -13.9 cm, and -9.3 cm in 2008, 2009 and 2010, respectively (Figure 4.9). Of note is the significant model underestimation of snow depth during water year 2009 as a result of underestimating a nearly sustained 16-day period of accumulation between 05 and 21 February during which 145 cm of accumulation was recorded but 101 cm were simulated. Despite the underestimation of a large snow accumulation event at Farewell Gap in 2009, the model exhibited high accuracy in the simulation of melt-season snow depth for all three years (Figure 4.9); the model accurately predicted the date of snow disappearance to the day in 2008, within two days in 2009, and within one day in 2010. The snow depth RMSE values were 13.4 cm, 23.3 cm, and 14.8 cm in 2008, 2009, and 2010, respectively.

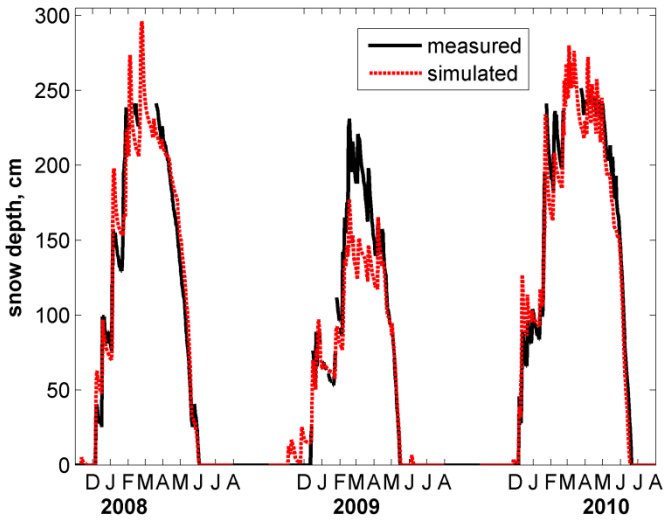

Figure 4.9. Simulated and measured snow depth at the Farewell Gap station for the three water years.

4.4.1.2 Sub-grid point-scale snow depth analysis

A comparison of simulated snow depth at locations of the four research plots in the forested Wolverton sub-basin provides insight into how the model at 100 m resolution grid spacing compares to multiple sub-grid observations. The mean (absolute) annual model snow depth errors averaged at all sites were only +5.4 cm (8.0 cm), -1.2 cm (2.6 cm), and +1.3 (1.3 cm) in 2008, 2009 and 2010, respectively (Figure 4.10). The results highlight a high degree of model accuracy in the prediction of snow depth when evaluated against multiple point-scale sensors located within a single model pixel. In general, snow depth model errors were most pronounced early in the accumulation season with lowest model errors during the melt season (Figure 4.10). For example, the snow disappearance date was within the observed range at all four sites in all three years. The only exception to this was at Site 4 in 2010 (see Figure 4.10) where the model simulated snow disappearance one day earlier than the earliest observed date.

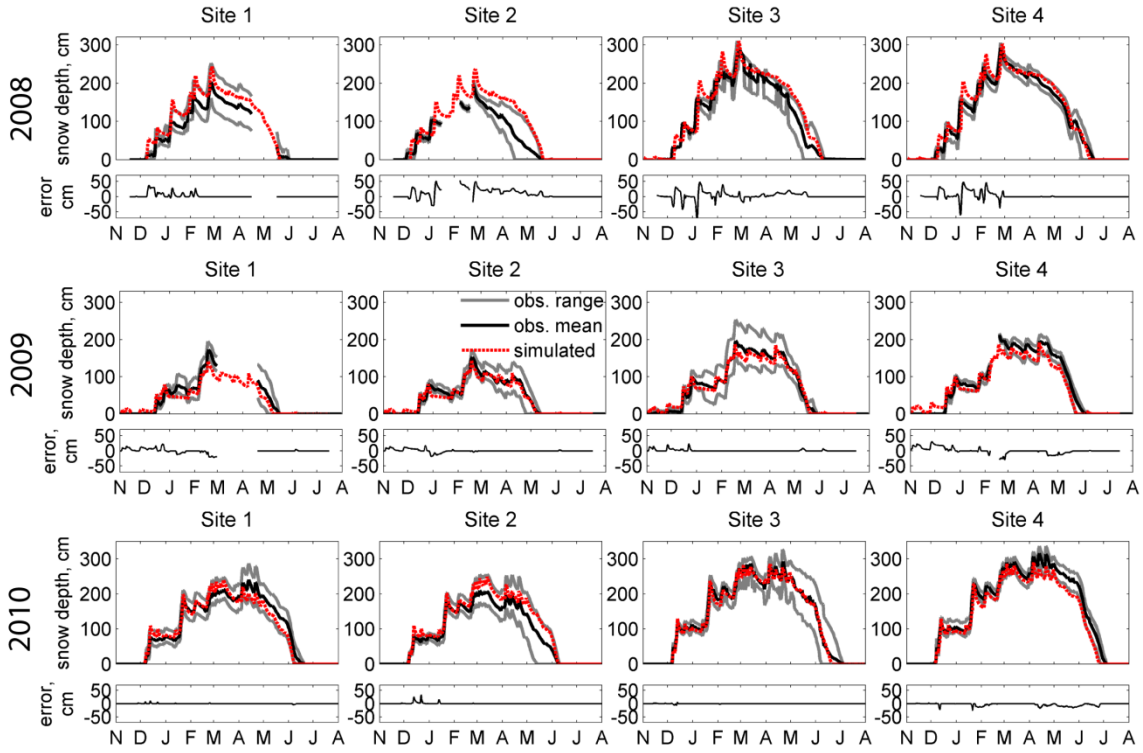

Figure 4.10. Comparison of three years of simulated (daily) snow depth to the observed mean and range of snow depth measured by six automated sensors each within four grid cells corresponding to locations of the forested research sites in the Wolverton sub-basin. The associated error for each site and year is shown as the difference between modeled and measured values when the modeled values occur beyond the observed range.

The model error seen in the February 2009 series of snow events that accumulated 145 cm at the Farewell Gap station (Figure 4.9) and was significantly underestimated (44 cm or 30.3%) by the model was not seen in the Wolverton basin where 111 cm were recorded and underestimated by only 15 cm (13.5%), on average. The difference in storm total (and model error) between the two sites could be a result of spatial variability of precipitation; significantly more precipitation may have fallen at Farewell Gap at a distance of 24 km from the Wolverton basin and in an area where precipitation was not measured.

4.4.1.3 Distributed snow depth analysis

Snow depth simulated by Alpine3D was compared to repeated monthly snow depth

measurements at seven survey locations. The comparison of seven model grid elements to snow depth survey measurements conducted in transects approximately equal to the model grid spacing potentially offers a higher degree of sub-grid representation than the high temporal, but single-point resolution of the automated snow depth sensor evaluated in Section 4.4.1.1. Additionally, the regional coverage of the monthly surveys (Figure 4.2) offers greater regional information than the network of 24 depth sensors presented in Section 4.4.1.2, at the expense of reduced temporal observation (i.e. monthly rather than hourly). Tables 4.4 – 4.6 include the model depth error for each of the seven stations for 2008, 2009, and 2010, respectively. Figure 4.11 summarizes the seasonal average normalized snow depth error at all seven survey sites for each of the three years. In general, model depth error was highest when evaluated against survey data at the Giant Forest (i.e. Site #1; negative error, or underestimated snow depth) and Scenic Meadow (i.e. Site #7; positive error, or overestimated snow depth) survey locations (Figure 4.11). These two survey locations represent the low and high elevation station end-members, respectively. The absolute depth error was highest at the Scenic Meadow survey site (i.e. Site #7 in Figure 4.11) for all three years. It is possible that the site's location on the leeward side of the Tokopah watershed is in a precipitation shadow that is not captured by the available precipitation gauges or by the statistical interpolation method. The same seasonal average normalized snow depth errors showed strong linear relationships ($R^2 > 0.80$, $p<0.01$) with the distance of the survey location from the nearest precipitation gauge used to force the model (Figure 4.11, right panel). The results suggest that model errors increased both with distance and elevation from the nearest precipitation gauge, an indication that spatial precipitation patterns are not well represented by the available station measurements.

Overall, the model showed consistency in the degree and magnitude of normalized snow depth error for all years with the exception of the lowest elevation survey sites 1 and 2 in 2009, where the model underestimated depth (Figure 4.11). These negative errors at the lowest elevation survey site (i.e. Site 1, Giant Forest) are counterintuitive when considered in the context of the close proximity to a precipitation gauge. The model is particularly challenged at this site because it is heavily forested and in a region that experiences more rain-on-snow events compared to upper elevation snow survey locations. In general, model snow depth errors were greater later in the season (i.e. April and May) than during the accumulation season (Tables 4.4 – 4.6).

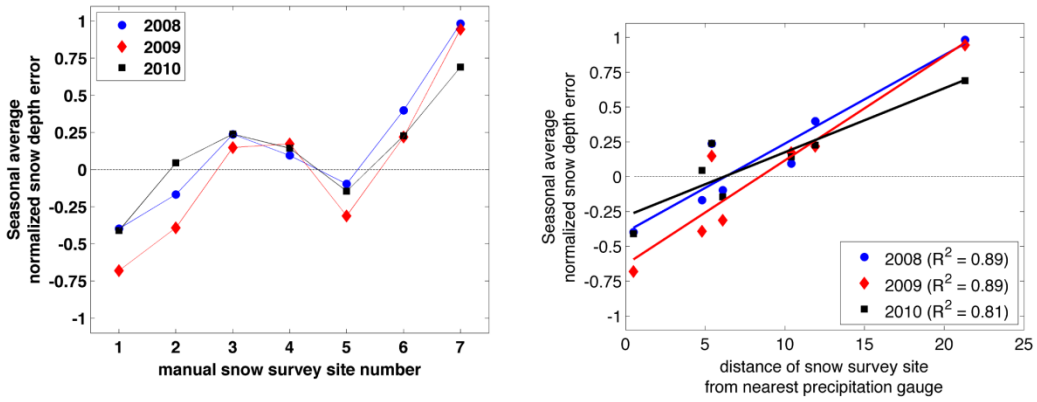

Figure 4.11. (Left): The Alpine3D normalized snow depth error computed against measurements made at manual snow survey locations (see Figure 4.2 and Table 4.1) as the seasonal average (February to April) error for each of the three years of the study. The survey number scheme is in order of increasing site elevation. (Right): The normalized snow depth error values plotted against the linear distance of survey locations from the nearest precipitation gauge used to force the model. The R^2 values shown are statistically significant ($p_{(0.05)} < 0.01$).

Finally, snow depth simulations were evaluated against repeated catchment-scale survey measurements made in the Wolverton and Tokopah sub-basins. In the forested Wolverton sub-basin, the model accurately represented the basin-mean snow depth well within one standard deviation of the measured values for three surveys conducted each in 2008 and 2009 (Figure

4.12). The model error was greatest on 28 April 2008 (18% overestimation) and 15 February 2008 (19% underestimation). In the largely alpine Tokopah sub-basin, the model significantly overestimated the basin-mean snow depth by 58% compared to the April 2008 survey measurements (Figure 4.12). The model was unable to simulate the high measured snow depth variability. For example, the minimum and maximum measured (modeled) depths were 0 cm (147 cm) and 523 cm (377 cm), respectively (see range in Figure 4.12). The results suggest that the model is not capturing areas of very low or high snow depth, which were measured in regions of exposed rock cliffs and ridgelines where preferential deposition is driven by wind transport. These processes often occur at scales much smaller than the 100 m model resolution and the issue of sub-grid variability is best addressed with high-resolution LiDAR data. For example, *Mott and Lehning* (2010) found that the most realistic wind field and snow deposition patterns were obtained at very high model resolution (5 m) compared to results of the same models run at larger grid spacing (up to 50 m). In the next section, the model is evaluated against LiDAR data, but the issue of sub-grid variability is beyond the scope of the study. Compared to the April 2008 survey results, in 2009 the basin-mean snow depth error values in the Tokopah were lower and were within one standard deviation of the measured values. Despite accurate depth simulation on 02 March 2009, basin-mean depth was overestimated on 12 April (+37%) and 16 May (+34%) (Figure 4.12).

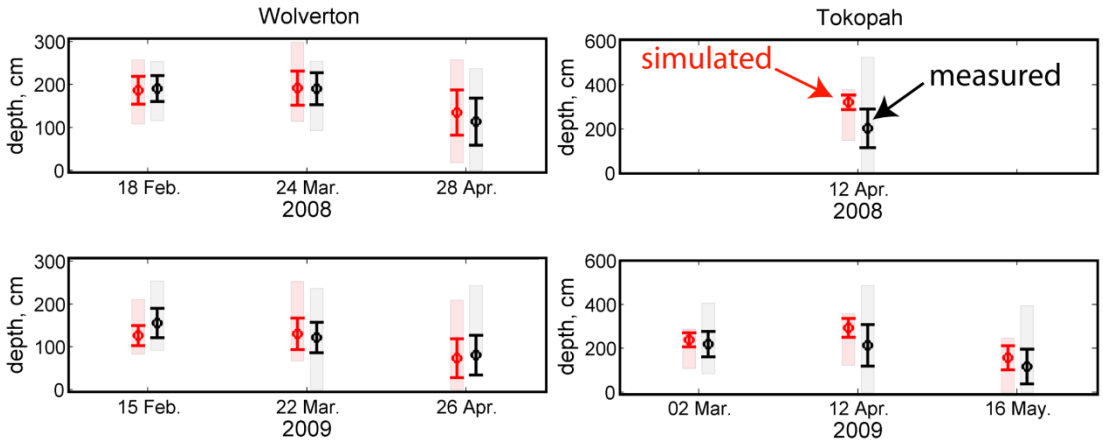

Figure 4.12. The mean (circles), standard deviation (bars), and range (shading) of snow depth in the Wolverton and Tokopah basins measured during catchment-scale surveys and simulated by Alpine3D.

4.4.1.4 LiDAR snow depth analysis

Compared to LiDAR-derived snow measurements obtained on 23 March 2010, Alpine3D significantly over-estimated snow depth (Figure 4.12). The mean error in the Tokopah sub-basin was 51 ± 70 cm, or a 27% over-estimation of the basin-mean measured value (see Section 4.3.2). The mean snow depth error in the Wolverton sub-basin was -2 ± 21 cm. In general, the model performed well at the forested lower elevations. Model errors were highest (positive, or an overestimation of depth) in areas that were steep and rocky with southerly aspects (see Figure 4.13); these are areas of the Tokopah basin that typically do not hold significant snow because of exposure to wind (and subsequent scour) and solar radiation (and subsequent melt).

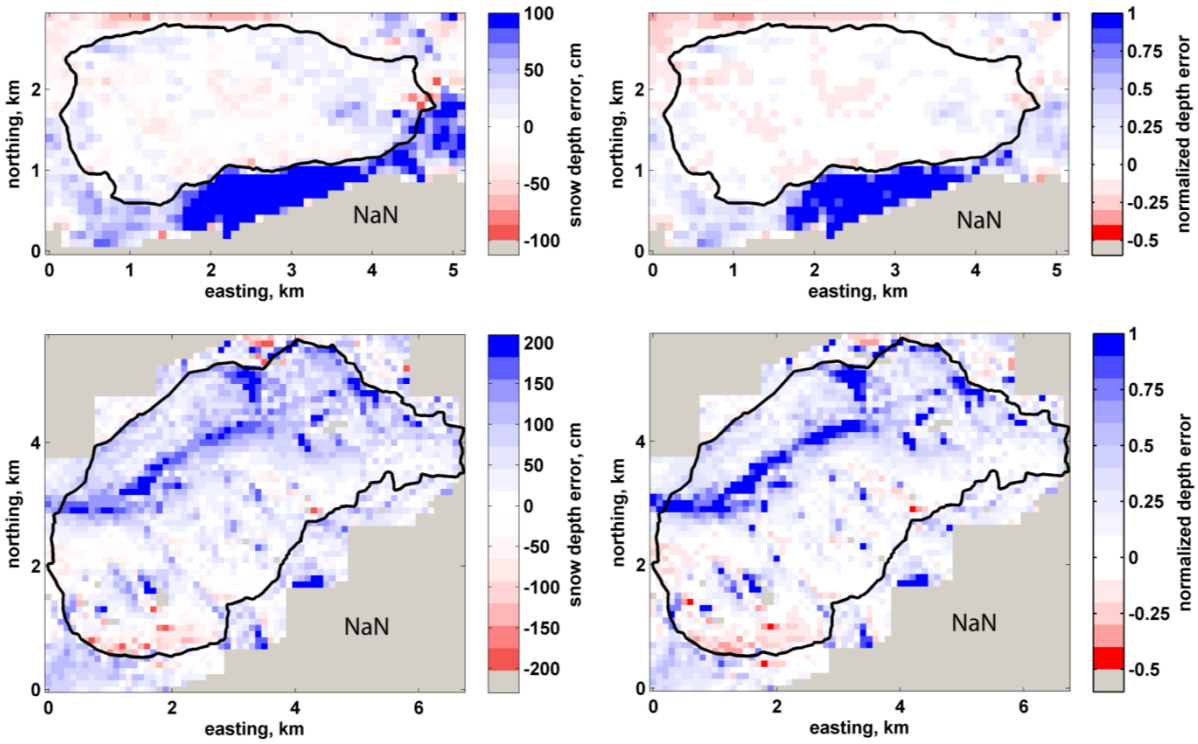

Figure 4.13. (Left panels) Error (modeled – measured) in simulated snow depth on 23 March 2010 determined from LiDAR measurements up-scaled to 100 m spatial resolution to match the model grid spacing. (Right panels) The model error normalized by the up-scaled snow depth measurements. Gray shading indicates the model domain beyond the measurement footprint.

Because wind redistribution was not accounted for in these model runs, it is possible that the model overestimated deposition by ignoring scouring effects on the rocky, windward slopes. The additional snow cover (i.e. higher albedo) might have negated the simulated melt dynamics between patches of steep, wind-exposed rock and the strong solar radiation on the southerly aspects. This suggests that the model is not accurately simulating mid-winter melt and/or snowpack densification on these south-facing, high elevation slopes; the surface of which are largely exposed bedrock.

4.4.2 SWE

Similar to snow depth, when simulated SWE was evaluated against monthly snow survey

data, the errors were generally positive (i.e. the model overestimated SWE) at four of the seven survey sites (Figure 4.14 and Tables 4.4 – 4.6). For all three years, the seasonal average normalized SWE error was lowest at survey sites 1, 2, and 5 (Figure 4.14); note that these three survey locations (Giant Forest, Big Meadows, and Panther Meadow, respectively) are the closest of the seven survey sites to the precipitation gauges used to derive the model forcing. Much like the snow depth results presented above, SWE error was generally greater at the upper elevation survey sites that were furthest from nearest precipitation gauge and errors were lower at the middle elevation sites closest to the nearest precipitation gauge (Figure 4.14, right panel). The results support the hypothesis that much of the model error may be explained by precipitation forcing errors. At the lowest elevation survey site, SWE in 2008 was generally underestimated compared to survey measurements (Table 4.4).

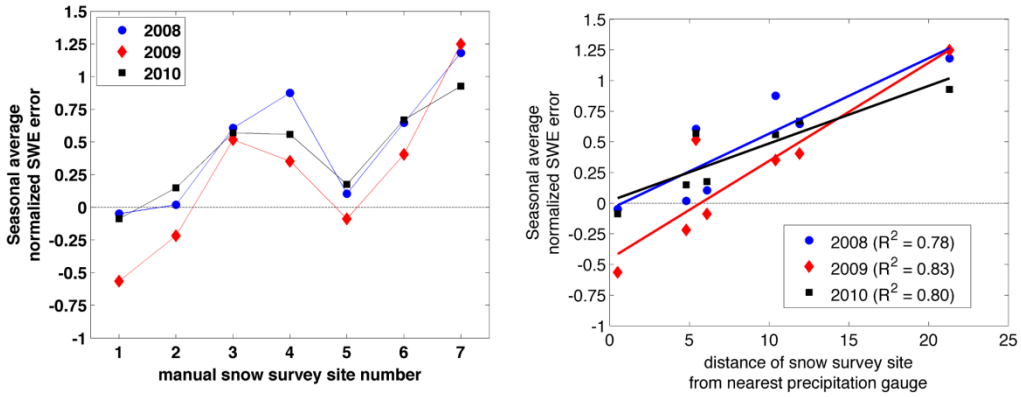

Figure 4.14. (Left): The Alpine3D normalized SWE error computed against measurements made at manual snow survey locations (see Figure 4.2 and Table 4.1) as the seasonal average (February to April) error for each of the three years of the study. The survey number scheme is in order of increasing site elevation. (Right): The normalized SWE error values plotted against the linear distance of survey locations from the nearest precipitation gauge used to force the model. The R^2 values shown are statistically significant ($p_{(0.05)} < 0.01$).

When modeled SWE was evaluated against Wolverton and Tokopah catchment-scale surveys, the basin-mean SWE was significantly greater than observed basin-mean SWE (i.e.

surveyed depth values multiplied by basin-average snow density measurements) (Figure 4.15). In 2008, the model overestimated the Wolverton basin-mean SWE by 32%, 49% and 70% in February, March and April, respectively (Figure 4.15). In 2009, the model overestimated SWE by 14%, 53% and 27%, in February, March and April, respectively (Figure 4.15); note that February and April mean SWE values were well within the measured standard deviation. The overestimation of SWE in the Wolverton sub-basin differs significantly from the accurate simulation of the snow depth discussed in Section 4.4.1.3 and shown in Figure 4.11. The discrepancy is a result of a difference between measured and simulated snow density. Measured (modeled) basin-mean density values in the Wolverton basin were 364 kg m^3 (496±35 kg m^3), 399 kg m^3 (585±32 kg m^3) and 439 kg m^3 (440±110 kg m^3) in February, March, and April 2008, respectively. Interestingly, the model tended to *underestimate* snow density late in the melt season, particularly at lower elevations when snow depths were < 40 cm. For example, the Wolverton basin-mean modeled snow density in April 2008 was highly variable because lower elevations that had very little snow remaining were erroneously simulated to have snow density values < 300 kg m^3 while areas with deeper snow had values near 600 kg m^3 (not shown). Future work should examine a potential model tendency to underestimate melt-season snow density values under conditions of low snow depth, when density values would be expected to remain high.

Modeled basin-mean SWE in April 2008 in the Tokopah basin was overestimated by 47% (Figure 4.15) whereas basin-mean depth was overestimated by 58% (see Figure 4.12). In this alpine area the model is slightly underestimating snow density (454 kg m^3) compared to measurements (495 kg m^3). The reason for the density discrepancy between the model and

measurements in the Wolverton basin is not immediately clear.

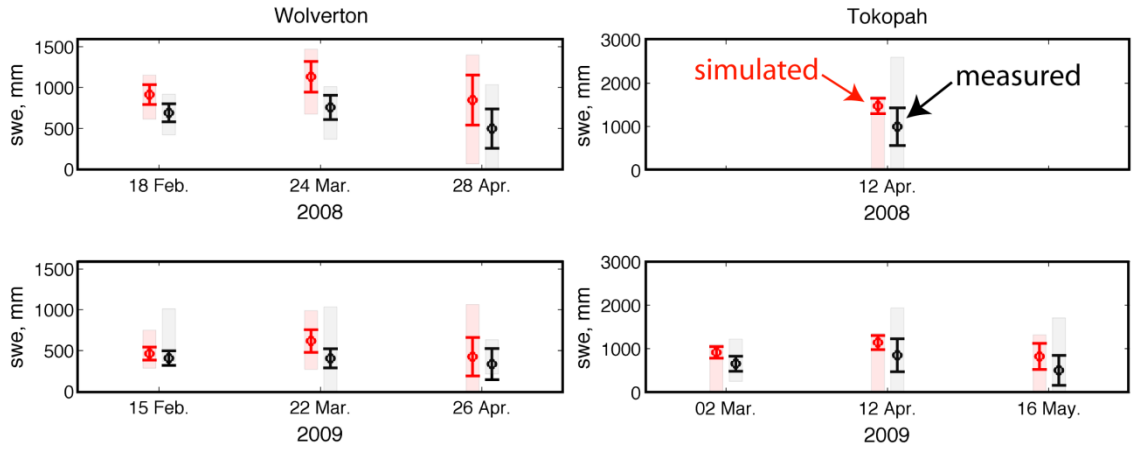

Figure 4.15. The mean (circles), standard deviation (bars), and range (shading) of SWE in the Wolverton (left panels) and Tokopah (right panels) basins measured during catchment-scale surveys and simulated by Alpine3D.

Table 4.4. Alpine3D normalized snow depth and SWE error computed against monthly survey measurements made in the area of the greater Kaweah River basin for 2008. Reported error is the difference between the modeled and measured values normalized by the measured value. Months when the measured value was zero but the simulated value was non-zero are indicated by 'na'. Months when surveys were not conducted are indicated (-).

#	Station name	2008							
		Feb.	Mar.	Apr.	May	Feb.	Mar.	Apr.	May
		norm. depth error				norm. SWE error			
1	Giant Forest	-0.16	-0.53	-0.50	na	0.30	-0.09	-0.36	na
2	Big Meadows	-0.27	-0.17	-0.06	-	-0.06	0.08	0.04	-
3	Mineral King	-	0.10	0.37	2.51	-	0.60	0.62	3.15
4	Hockett Meadow	-	-0.06	0.25	0.47	-	1.38	0.37	0.63
5	Panther Meadow	-	-0.13	-0.06	-0.05	-	0.03	0.18	0.20
6	Rowell Meadow	0.21	-	0.59	-	0.63	-	0.66	-
7	Scenic Meadow	0.70	-	1.27	-	0.88	-	1.48	-

Table 4.5. Alpine3D normalized snow depth and SWE error computed against monthly survey measurements made in the area of the greater Kaweah River basin as Table 4.4 but for 2009.

#	Station name	2009							
		Feb.	Mar.	Apr.	May	Feb.	Mar.	Apr.	May
		norm. depth error				norm. SWE error			
1	Giant Forest	-0.65	-0.57	-0.82	na	-0.58	-0.45	-0.66	na
2	Big Meadows	-0.33	-0.47	-0.38	-	-0.10	-0.22	-0.33	-
3	Mineral King	0.15	-0.05	0.35	0.59	0.26	0.63	0.66	0.46
4	Hockett Meadow	-	-	0.17	0.84	-	-	0.35	0.94
5	Panther Meadow	-0.28	-0.37	-0.29	-0.37	-0.02	-0.15	-0.09	-0.13
6	Rowell Meadow	0.26	-	0.18	-	0.48	-	0.33	-
7	Scenic Meadow	1.09	-	0.80	-	1.59	-	0.91	-

Table 4.6. Alpine3D normalized snow depth and SWE error computed against monthly survey measurements made in the area of the greater Kaweah River basin for 2010.

#	Station name	2010							
		Feb.	Mar.	Apr.	May	Feb.	Mar.	Apr.	May
		norm. depth error				norm. SWE error			
1	Giant Forest	-0.40	-0.38	-0.44	-0.61	0.03	0.01	-0.30	-0.29
2	Big Meadows	-0.02	-0.09	0.07	-	0.18	0.18	0.09	-
3	Mineral King	0.21	0.13	0.37	0.59	0.60	0.41	0.69	0.97
4	Hockett Meadow	-	0.17	0.12	0.33	-	0.64	0.48	0.53
5	Panther Meadow	-0.28	-0.09	-0.06	-0.12	0.21	0.15	0.17	0.29
6	Rowell Meadow	0.06	-	0.40	-	0.61	-	0.72	-
7	Scenic Meadow	0.42	-	0.96	-	0.76	-	1.09	-

When compared to SWE measured during the monthly survey conducted at the Panther Meadow survey site in the Wolverton basin, the mean model errors were +14%, -10%, and +21% in 2008, 2009, and 2010, respectively (Tables 4.4 – 4.6). The errors were lower than the previous comparison of modeled SWE to catchment-scale (spatial-mean) survey measurements. The SWE discrepancy between the Panther Meadow monthly measurements (made with a Federal snow tube sampler) and the basin-scale measurements (derived from snowpit density measurements) are possibly a result of differences in reported density values. An evaluation of the model against continuous SWE data in the region provides additional insight into potential

sources of the SWE error discrepancy.

In 2008 the model simulated SWE at the Giant Forest station with an RMSE of 49 mm and at the Big Meadows station with an RMSE of 39 cm (Figure 4.16). At the higher elevation Farewell Gap station the model overestimated SWE in 2008 with an RMSE of 127 mm. The errors shown in Figure 4.16 do not reflect the high errors seen in the basin-scale survey results. A simple comparison of density measured snow at the automated Farewell Gap station where both depth and SWE were recorded indicates that the seasonal maximum density in 2008 was generally greater than 550 kg m^{-3} and the density was consistently greater than 500 kg m^{-3} between 25 March and the 30 May snow disappearance date; the mean density during this period was 551 kg m^3. The melt-season density values both from the Federal snow tube measurements at Panther Meadow and the collocated automated depth sensor and snow 'pillow' at Farewell Gap (> 500 kg m^3) are significantly greater than the density values measured in the Wolverton snowpits in the same year (< 440 kg m^3). The errors could have resulted from measurement error, but the source of that error is not immediately clear.

In general, Figure 4.16 illustrates low model error in the simulation of SWE. The lowest model errors were obtained at the Giant Forest station for all years (RMSE = 51 cm SWE) and at all sites in 2008. In 2009, the model underestimated SWE compared to measurements at the Big Meadows station (RMSE = 91 cm, normalized model error = -0.33), but accurately estimated SWE at Giant Forest (RMSE = 25 cm, normalized model error = -0.12), and Farewell Gap RMSE = 50 cm, normalized model error = -0.08) stations. In 2010, the model overestimated SWE by 15% at Giant Forest, 27% at Big Meadows, and 23% at Farewell Gap. The 2010 results from these automated SWE stations are consistent with the errors observed in snow depth fields

from the 2010 LiDAR flight in which positive depth errors generally increased with elevation (see Figure 4.13).

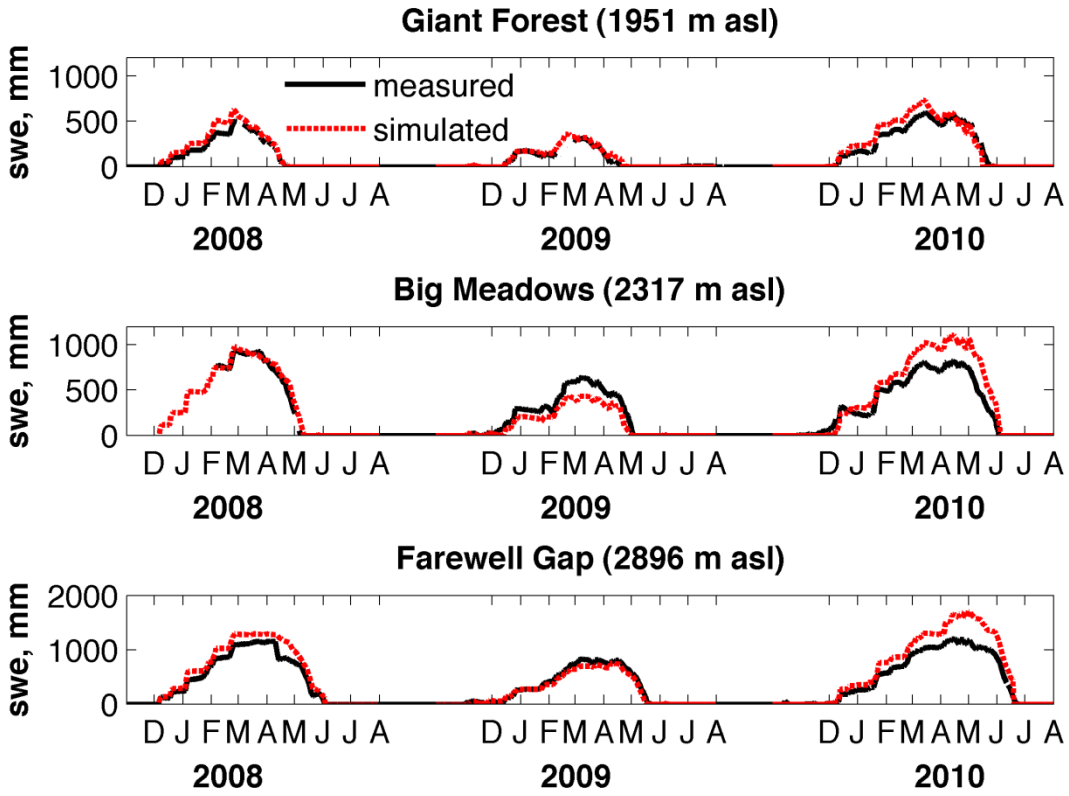

Figure 4.16. Comparison of measured and simulated SWE at the three automated snow stations spanning the middle elevation range of the greater Kaweah River basin.

Finally, the data from the three automated SWE stations can be used to evaluate how well the model predicts the date of snow disappearance. This date is of critical hydrological and ecological importance as it defines the end of snowmelt water input to the soil system. Because of scale issues with comparing point measurements to the modeled 100 m x 100 m grid element, a more robust comparison was obtained in the Wolverton basin where multiple automated snow depth sensors fell within individual model grid cells. The model accurately predicted the snow

disappearance date within the observed range (see Figure 4.10). The point comparison of SWE station measurements of snow disappearance date provides a less robust estimate of model skill, but over a much larger domain than the Wolverton basin evaluation. At all locations and for all three years, the model accurately predicted the date of snow disappearance with an accuracy of three days or better (see Figure 4.16). The exception to this was at the lower elevation Giant Forest station in 2010 when the model predicted snow disappearance ten days earlier than the measured date. In general, compared to all available automated measurements (27 total stations) Alpine3D accurately predicted the date of snow disappearance.

4.4.3 Inter-annual accumulation and melt patterns

The model results were used to evaluate inter-annual accumulation and melt patterns. Distinct patterns are evident. In particular, four metrics were computed for each year: 1) the date of maximum SWE; 2) the date of snow disappearance; 3) the spring melt duration computed as the number of days between the first two metrics; and 4) the fraction of that melt duration in which the daily SWE change was negative (i.e. melt was simulated). The next sections describe the computation of each of these metrics, evaluate the simulated values against automated station measurements, and finally inter-annual patterns are compared and discussed.

4.4.3.1 Date of maximum SWE

Maximum SWE was measured on 27 February 2008 at the middle elevation Giant Forest (Figure 4.17, lower-left panel) and Big Meadows (Figure 4.17, left-center panel) stations (see Table 4.7). This coincided with the timing of the last appreciable precipitation event of the 2008

season (see Figure 4.9), after which melt began at both stations as inferred from the SWE record. Conversely, maximum SWE was measured at the upper elevation Farewell Gap station five weeks later on 05 April 2008 (Table 4.7).

Table 4.7. Date of maximum SWE measured and modeled at the three automated snow stations and modeled mean and standard deviation of the date of maximum SWE in the Wolverton and Tokopah basins for the three years of the study.

Date of max. SWE	2008			2009			2010		
Location	Meas.	Model	Error, days	Meas.	Model	Error, days	Meas.	Model	Error, days
Giant Forest	27 Feb.	26 Feb.	-1	na	22 Feb.	na	15 Mar.	15 Mar.	0
Big Meadows	27 Feb.	26 Feb.	-1	06 Mar.	07 Mar.	+1	14 Apr.	14 Apr.	0
Farewell Gap	05 Apr.	06 Apr.	+1	07 Mar.	11 Apr.	+35	14 Apr.	01 May	+16
Wolverton basin	na	12 Mar. ± 18 d	na	na	30 Mar. ± 20 d	na	na	08 Apr. ± 10 d	na
Tokopah basin	na	08 Apr. ± 6 d	na	na	29 Apr. ± 7 d	na	na	10 May ± 8 d	na

The date coincided with the timing of the last (minor) precipitation event of the season and no melt was observed prior to this date. The three SWE records measured at different elevations are examples of an elevation transect across energy and precipitation gradients. Figure 4.17 illustrates a distinct transition from the lower elevations where melt progresses quickly after the date of maximum SWE (e.g. Giant Forest) to middle elevations where melt is more temporally variable after maximum SWE (e.g. Big Meadows), to upper elevations where melt is delayed relative to lower elevations, causing the date of maximum SWE (and the subsequent melt) to occur later in year.

Compared to measurements at the Giant Forest and Big Meadows automated stations, the dates of maximum SWE were simulated within one day in 2008, 2009, and 2010 (Table 4.7; note that a sensor error at Giant Forest prevented the observation of maximum SWE in 2009). Errors in simulated maximum SWE were observed at the higher elevation Farewell Gap station (Table 4.7) in 2009 and 2010. These two years were characterized by significant spring snow accumulation that caused many 'local maxima' in the SWE time series (Figure 4.17) that are

close in magnitude to the seasonal (i.e. 'global') maximum SWE. For this reason, slight model errors in SWE on the order of 1% could result in errors in the simulated maximum SWE date exceeding one month (Table 4.7). On its own, the importance of the date of maximum SWE in the context of water availability can be ambiguous. However, when evaluated in conjunction with the date of snow disappearance and, particularly, the number of days between the two metrics, more information on general snowmelt dynamics is obtainable.

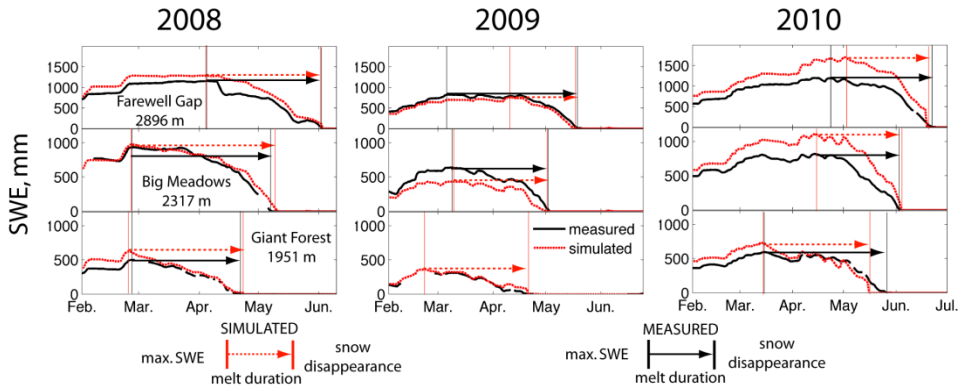

Figure 4.17. Comparison of simulated and measured SWE (in mm) at the three automated stations for the three years. The station data are shown in increasing elevation (from lower to upper panels) to highlight the general later shift in the date of maximum accumulation and/or snow disappearance with elevation and the variable impact of this shift on melt duration.

4.4.3.2 Date of snow disappearance and melt season duration

When evaluated against automated sensors, Alpine3D was highly accurate in the predicted date of snow disappearance (see Figures 4.10 and 4.17 and Section 4.4.1). For all simulated years, the date of snow disappearance was determined as the first date that snow disappeared after the date of maximum SWE accumulation. When computed in this way, the metric has reduced physical meaning at lower elevations where snow cover melts out after each snow event (i.e. is ephemeral in nature). But since regional snow measurements were unavailable

at lower elevations where ephemeral snow cover persists, this study largely focused on snowmelt dynamics in regions with continuous seasonal snow cover.

Figure 4.18 shows the regional distribution of the simulated date of maximum SWE (Figures 4.18a-c), snow disappearance date (Figures 4.18d-f), and the number of days between maximum SWE and snow disappearance (Figures 4.18g-i) for years 2008, 2009 and 2010. The locations of the three automated SWE stations are indicated in Figure 4.18 and the measurements plotted in Figure 4.17 are useful to evaluate the larger-scale trends shown in Figure 4.18. In general, the simulated date of snow disappearance varied smoothly across the terrain (Figure 4.18d-f); it occurred earlier at lower elevations and on south aspects and later at upper elevations and on north aspects. The date of maximum SWE varied less consistently with elevation than the snow disappearance date, but when it did change, it occurred abruptly (Figure 4.18a-c). For example, in 2008 the date of maximum SWE was relatively constant at middle elevations but jumped to one month later at and above an elevation of approximately 2600 m. Similar 'breakpoints' in the timing of maximum SWE were simulated in 2009 and 2010 at an elevation of approximately 2200 m and 2000 m asl, respectively. The breakpoint stands out clearly in spatial maps of the seasonal melt duration (Figure 4.18h-i).

In particular, the longest melt durations in the region are found to occur at middle elevations and the exact location of that band varies inter-annually. The melt duration generally increases from lower elevations to the middle elevation until this maximum SWE breakpoint is reached where the melt duration decreases significantly before increasing again with elevation. A great example of these melt duration dynamics is seen in the measured / modeled data at the three automated SWE stations that effectively transect this narrow elevation range in 2008

(Figure 4.17). The lowest elevation Giant Forest station is located lower in elevation than this melt duration breakpoint. The Big Meadows station is located just below the breakpoint where melt duration is longest, and the Farewell Gap station is located significantly above this breakpoint where the melt duration is shorter than at Big Meadows but longer than directly above the breakpoint (Figures 4.18). Figure 4.17 clearly shows strong agreement between the measured and simulated melt duration trends at the three sensor locations. The simulated melt duration was 58 days at Giant Forest, 75 at days Big Meadows, and 63 days at Farewell Gap, while the measured values were within two days of the simulated durations (Figure 4.17).

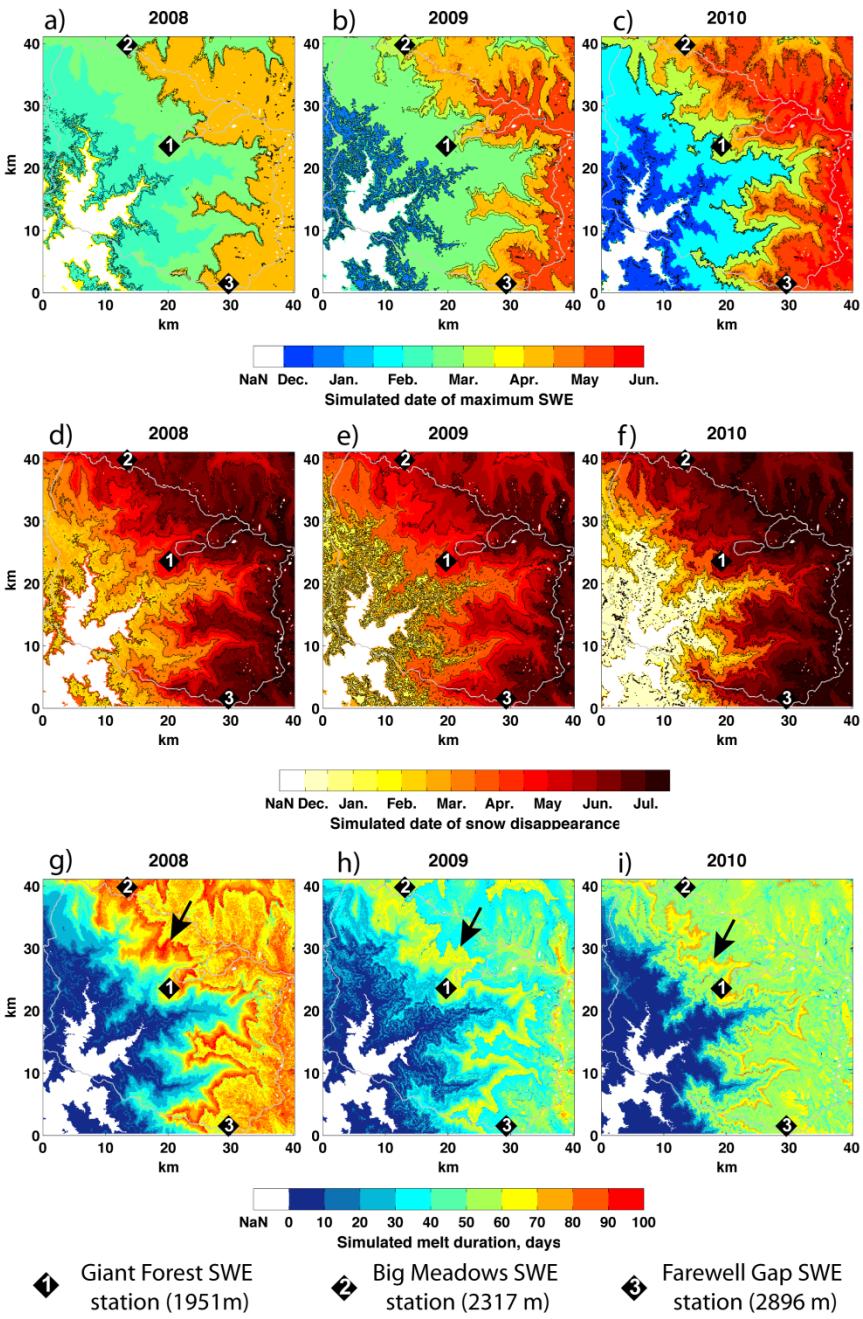

Figure 4.18. (a – c): Simulated date of maximum SWE in (a) 2008, (b) 2009, and (c) 2010. (d – f): Simulated date of snow disappearance for (d) 2008, (e) 2009, and (f) 2010. (g – i): Simulated snow melt duration computed as the number of days between the dates of maximum SWE and snow disappearance for (g) 2008, (h) 2009, and (i) 2010. Arrows indicate the approximate elevation of the melt duration 'breakpoint'. Locations of the three automated stations are indicated.

Figure 4.19 illustrates the elevation distribution of the simulated melt duration shown in Figure 4.18 for each of the three years. The longer melt duration at middle elevations is apparent. The elevation band of the longest melt duration ranges from 2200 m to 2600 m asl in 2008, 2000 m to 2400 m asl in 2009, and 1600 m to 2200 m asl in 2010. The longer melt duration occurred over a ~400 m elevation range in 2008 and 2009, and a slightly greater elevation range of ~600 m in 2010. The previously mentioned 'breakpoint' is specified by the upper value of these ranges.

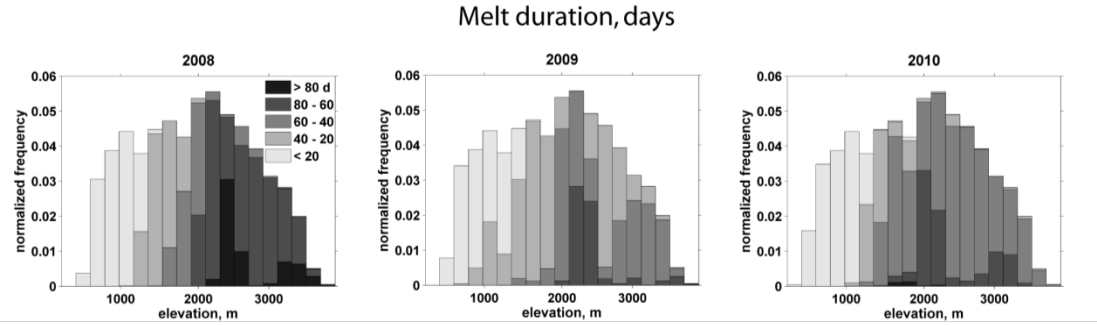

Figure 4.19. Histograms of the elevation distribution of the simulated melt duration, in days, for the three years.

The physical meaning of the melt breakpoint and this elevation band of prolonged melt duration is worth addressing. First, the term 'melt duration' to refer to the period of time between the dates of maximum SWE and snow disappearance is somewhat misleading in that melt does not necessarily occur over the entire period. Days that are below freezing and/or days with snowfall do frequently occur after the date of maximum accumulation. The fraction of this melt duration in which melt actively occurs (i.e. a negative daily change in SWE is simulated) is plotted in Figure 4.20. In 2008, a year with very little precipitation or cloud cover after maximum SWE, daily SWE loss occurred in 90% of the melt duration period (Figure 4.20). Generally, that percentage increased with elevation in 2008 and did not vary significantly in

spatial extent (note the large area of 90% values in Figure 4.20). In contrast, late-season snowfall and/or cloud cover characterized years 2009 and 2010. In these years, the same middle elevation bands had distinctly lower percentages (i.e. < 85%) of days after maximum accumulation in which melt occurred (Figure 4.20). As inferred from the automated station measurements within this elevation range, this is a result of mid-winter melt that reduces snowpack SWE and causes maximum SWE to occur earlier. In effect, any late season snowfall that might result in a later seasonal maximum SWE at higher elevations where colder temperatures limit mid-winter melt, would not exceed the mid-winter maximum SWE value at middle elevations where mid-winter melt regularly occurs.

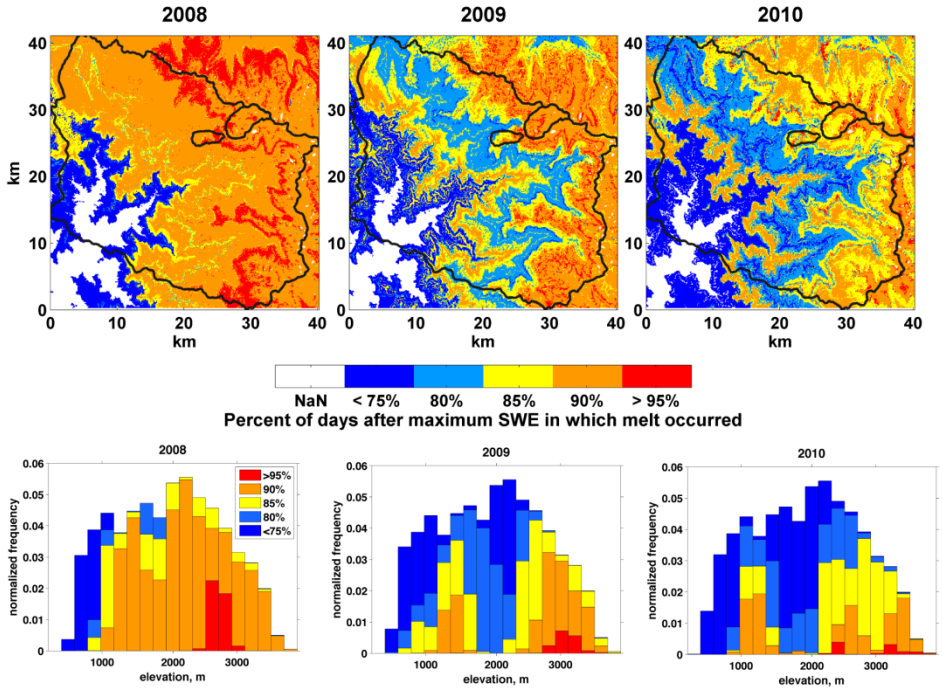

Figure 4.20. (top row): The simulated fraction of days, in percent, between the periods of maximum SWE and snow disappearance in which melt occurred for years 2008, 2009 and 2010. (bottom row): Histograms of the elevation distribution of the simulated fraction of days, in percent, after maximum SWE in which melt occurred for each of the three years.

There is significant ambiguity with the use of the 'date of maximum SWE' metric to infer

melt timing and processes. As discussed previously, slight variations in seasonal SWE magnitude and/or melt rates can change the maximum SWE date by more than a month with little if any influence on the hydrology or ecology. A more comprehensive analysis of seasonal and inter-annual snowmelt processes includes considering the number of days in which melt occurred normalized by the snow cover duration, and the average melt rate computed only on days in which melt occurred. Figure 4.21 (upper panels) shows the snow cover duration for each of the three years. The 2010 season recorded the latest snow disappearance date of the three years at the middle elevations as measured at the automated stations, but the shortest snow cover duration at the highest elevations (Figure 4.21 upper panels). This is a result of 2008 and 2009 both receiving early-season (i.e. October and November) snowfall that persisted as continuous snow cover at upper elevations but melted out at lower elevations, whereas the first snowfall of 2010 did not occur until early December.

The fraction of the snow-covered period in which melt was simulated (i.e. a net daily change in SWE < -0.6 mm day^{-1} was observed) showed interesting inter-annual variability in terms of where the majority of melt occurred (Figure 4.21 center panels). This metric is useful to infer seasonal water availability to the soil system. Many of the results were intuitive. For example, when snow-covered, the lowest elevations experienced snowmelt 80% to 100% of the time in all three years and the highest elevations were least prone to melt events in all three years.

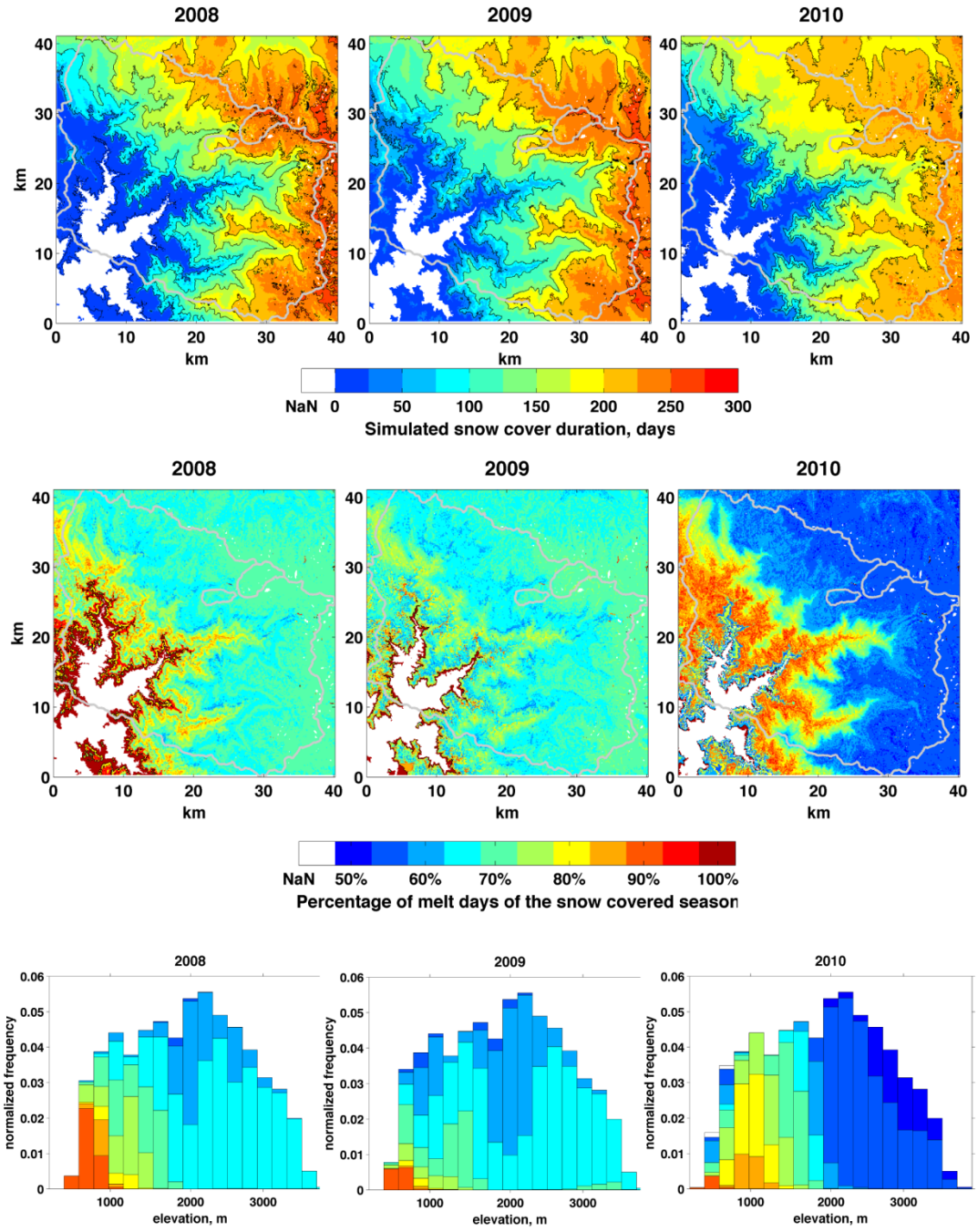

Figure 4.21. (Top panels) The number of days with snow cover, (middle panels) the percent of the snow covered period in which daily net melt occurred, and (lower panels) the elevation distribution of the melt fraction shown in the middle panels for each of the three years (figure columns).

Other results were less intuitive. For example, the upper elevations in 2010 experienced melt

~55% of the snow-covered period while in both 2008 and 2009 melt occurred during ~75% of the snow-covered period (Figure 4.21 center panels). The difference was caused by the early-season snowfall in 2008 and 2009 that resulted in more (average) melt days than in 2010 when continuous snow cover at upper elevations began in December when solar elevations and air temperatures were lowest. Finally, as seen in the previous analysis of the melt duration, the middle elevations showed distinct differences in melt frequency. The bottom panels in Figure 4.21 show the elevation distribution of the simulated melt frequency for the three years. In 2008 and 2009, the middle elevations (~1800 m – 2200 m asl) had slightly lower frequency of melt (60%) than the upper elevations (~65%) and significantly lower frequency than the lowest elevations (75% - 100%). This discrepancy was not simulated in 2010 (Figure 4.21). While the differences in melt frequency between middle and upper elevations in 2008 and 2009 were slight, they are counter-intuitive and likely a result of the melt occurring over different time periods and at different rates at different elevations.

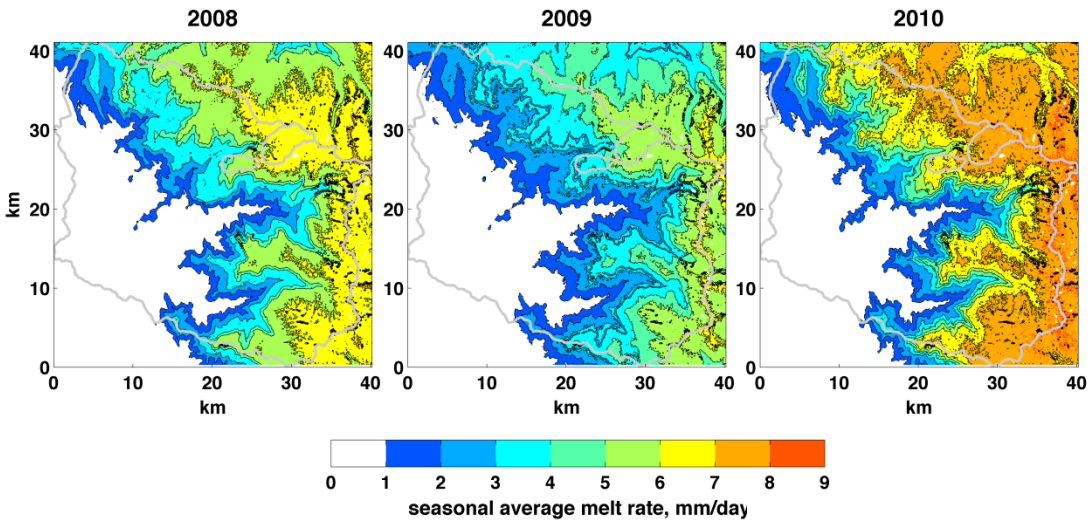

Figure 4.22. The average melt rate computed only on days in which melt occurred for 2008, 2009, and 2010.

Figure 4.22 shows the average melt rate computed as the magnitude of daily SWE change only computed on days when the change in SWE was negative. The seasonal average melt rate generally increased with elevation. At lower elevations, where mid-winter melt occurred under generally lower temperatures and energy fluxes, the seasonal average melt rate was lowest (< 3 mm day^{-1}). Conversely, the upper elevations were simulated to have the greatest seasonal average melt rates of 6.5 mm day^{-1}, 5.5 mm day^{-1}, and 7.5 mm day^{-1} in 2008, 2009, and 2010, respectively. The high melt rates at the upper elevations are caused by melt occurring predominantly in the spring and early summer when temperatures and energy fluxes are greatest. The inter-annual variability simulated by Alpine3D supports the findings of Chapter 2, in which cloud cover and, implicitly, late-season precipitation, was found to explain a majority of the inter-annual snowmelt variability measured in the Wolverton basin.

The results suggest that there exists a critical elevation zone that 1) remains continuously snow covered throughout the winter and early spring, 2) is prone to intermittent but significant inter-storm melt (i.e. SWE loss), 3) has an earlier date of maximum SWE as a result of early season melt that reduces snowpack SWE such that late season snowfall does not exceed the mid-winter maximum value, and 4) provides the most sustained period of meltwater fluxes to the soil system. Furthermore, the elevation range of this critical band varies inter-annually depending on seasonal meteorology but generally overlapped the conifer forest elevation zone in all three years (see Figure 4.1).

4.5 Summary

The results of the model evaluation highlight strengths and weaknesses in both the snow model and the extensive suite of multi-scale measurements. Overall, the model accurately estimated snow depth, SWE and the timing of snow disappearance at middle elevations. The model accuracy in terms of depth and SWE was most limited at the upper elevations, and particularly in the Tokopah basin compared to basin-scale survey measurements in 2008 and 2009 and LiDAR measurements in 2010. Snow depth and SWE errors computed on monthly survey measurements made at seven locations in the greater Kaweah River basin were found to (linearly) become more positive with distance of the survey location from the nearest precipitation gauge. The results suggest that precipitation uncertainty is a critical limitation on snow model accuracy. Precipitation is possibly the most difficult variable to measure at the point-scale as well as to interpolate over complex terrain. Precipitation data used in the study were not measured above elevation 2073 m asl and linear lapse rates were computed to extrapolate lower elevation measurements to the higher elevations. The application of the linear lapse rate with an IDW statistical extrapolation of *Liston and Elder* (2006b) to precipitation data in regions that were great distances from and/or on opposite sides of large ridges from gauges were unlikely to represent complex orographics known to cause synoptic scale precipitation variability.

Good model performance was noted when simulated depth was compared to catchment-scale observations made in the forested Wolverton basin (six manual surveys and one LiDAR campaign), but SWE was overestimated by as much as 50%. It is possible that the precipitation lapse rates computed from gauge measurements made at the lower and middle elevations of the

Kaweah River basin are higher than might be measured between middle and upper elevations. Modeled melt-season basin-mean snow density values exceeded Wolverton snow pit measurements by greater than 15%, but were similar to those derived from local automated depth and SWE measurements. Compared to automated measurements, the normalized model SWE error was generally less than 10% but larger positive model biases near 25% were observed at the highest elevation stations in 2010, the season with the most precipitation. The model simulated the snow disappearance date within two days of the measured dates in nearly all cases. In locations and years where SWE was overestimated compared to automated station measurements but the snow disappearance date occurred within a few days of the measured value, the simulated melt rates must also have been overestimated. While this was not explicitly evaluated, these two errors (overestimating SWE and melt rate) must have counteracted each other.

The clusters of automated snow depth sensors showed great utility in estimating sub-grid scale ranges of snow depth and snow disappearance dates. The model compared well to the mean snow depth at locations of the depth sensor clusters and was generally within the observed range, particularly during the melt season. The model also accurately predicted the date of maximum SWE accumulation in six of the eight sensor-years in which automated SWE measurements were available. The ability of the model to predict with high accuracy the dates of maximum SWE and snow disappearance made it useful to evaluate seasonal and inter-annual melt patterns.

In summary, the above analyses of seasonal and inter-annual snowmelt patterns highlighted distinct melt differences between lower, middle, and upper elevations. Snowmelt was generally most frequent (70% - 95% of the snow-covered season) at the lower elevations where

snow cover was ephemeral and seasonal mean melt rates computed on days when melt was simulated were generally low (< 3 mm day^{-1}). At upper elevations, melt occurred during less than 65% of the snow-covered period, it occurred later in the season, and mean melt rates were the highest of the region (> 6 mm day^{-1}). Middle elevations remained continuously snow covered throughout the winter and early spring, were prone to frequent but intermittent melt, and provided the most sustained period of seasonal mean snowmelt (~ 5 mm day^{-1}). The melt dynamics (e.g. timing and melt rate) unique to these middle elevations may be critical to the local forest ecosystem. Furthermore, the three years evaluated in this study indicate a marked sensitivity of this elevation range to seasonal meteorology, suggesting that it could be highly sensitive to future changes in climate.

Chapter 5. Conclusions and Future Work

5.1 Conclusions and original contributions

The three studies described above represent an analysis of the distribution of snow properties in forested and alpine terrain. As previously noted, the overarching science question addressed in this thesis is: *What are the limitations of physically based models in forested regions and how do model limitations observed at the plot-scale impact larger-scale estimates of snow water resources in mountainous terrain?* This question has been addressed using a multi-scale, multi-year measurement approach that documented the variability, and point-scale and spatially distributed modeling methods that simulated the observations.

In Chapter 2, snowmelt rates measured for three years at forested research plots were presented. Estimates of sub-canopy direct beam solar irradiance and sky view factor (SVF_θ)

derived from hemispherical photographs were used to explain the spatial distribution of observed melt rates. Cumulative direct beam irradiance during the observed snowmelt periods explained the most variability in melt rates for the most cloud-free melt season (58% in 2008; four cloudy days) and explained the least melt rate variability for the cloudiest melt season of the study (29% in 2009; 23 cloudy days). Conversely, sky view factor (SVF_θ) explained the most variability in snow ablation rates under cloudier conditions (i.e. 87% in 2009) and the relationships were strongest when developed over the entire hemisphere.

In Chapter 3, the two metrics studied in Chapter 2 (sub-canopy direct beam irradiance and SVF_θ) were applied to a one-dimensional physically based soil-snow-vegetation model to test the utility of the metrics to simulate observed variability. Three model scenarios, each with a different level of canopy structure detail, were tested. Model simulations of the three water years initialized at the same snow depth sensor locations were evaluated against observations of snow water equivalent (SWE), snow disappearance date, and volumetric soil water content. When bulk canopy model parameters *canopy openness* and *effective leaf area index* were obtained from satellite and literature-based sources, respectively, the model was unable to resolve the variable sub-canopy snowmelt dynamics. When the canopy parameters were obtained from hemispherical photos, the model improvements were not statistically significant. However, when the model was modified to accept the photo-derived time-varying direct beam canopy transmissivity presented in Chapter 2, the error in the snow disappearance date was reduced by as much as one week and positive and negative biases in melt-season SWE and snow cover duration were significantly reduced. Errors in the timing of soil meltwater fluxes were reduced by 11 days on average. The optimum aggregated temporal model resolution of direct beam canopy transmissivity was

determined to be 30-minutes; hourly averages performed no better than the bulk canopy scenarios and finer time steps did not increase overall model accuracy. The improvements illustrate the important contribution of direct shortwave radiation to sub-canopy snowmelt and confirm the known non-linear melt behavior of snow cover.

In Chapter 4, a distributed version of the snow-vegetation model used in Chapter 3 is applied to a large domain (~ 1,650 km^2) spanning an elevation gradient in excess of 3500 m and land cover ranging from semi-arid grasslands to perennial snowfields. Results from three years of simulation were evaluated against a suite of multi-scale observations made across the seasonally snow-covered region. Specifically, model accuracy was evaluated: 1) in forested areas where model errors are typically highest, and 2) at upper elevations where the most snow water resources accumulate yet no precipitation measurements are available. Alpine3D accurately simulated snow depths in the middle elevation conifer forests compared to data from four clusters of six ultrasonic snow depth sensors covering the spatial extent of a model grid cell. At upper elevations, the model tended to overestimate SWE. The SWE errors could largely be explained ($R^2 > 0.80$, $p<0.01$) by distance of the SWE measurement from the nearest precipitation gauge. The results suggest that precipitation uncertainty is a critical limitation on snow model accuracy. As observed at the point-scale in Chapter 3, depth and SWE errors at middle and upper elevations were greatest in 2010 when snowmelt was delayed until late spring. A comparison of simulated snow depth to LiDAR measurements in the alpine Tokopah basin indicated that the Alpine3D model overestimated basin-mean snow depth by 27%, particularly at the highest elevations and on south aspects in steep, rocky terrain. Additionally, the model is unable to capture much of the depth variability seen in the LiDAR data, possibly as a result of

not simulating wind transport and redeposition in the model. If the precipitation forcing errors could be improved to better represent basin mean snow depth, errors in the variability may be less important at larger scales relevant to snow water resources.

The model accurately simulated the snow disappearance date within two days of the measured dates in nearly all cases where automated measurements were available, indicating good melt-season performance in middle elevation, forested regions in close proximity to precipitation gauges. An analysis of seasonal and inter-annual snowmelt patterns highlights distinct melt differences between lower, middle, and upper elevations. Snowmelt was generally more frequent at the lower elevations where snow cover was episodic, but the seasonal mean melt rates were generally low (< 3 mm day^{-1}) because the melt occurred in mid-winter when sun elevations and temperatures were lowest. At upper elevations, melt occurred less than 65% of the snow covered period but when it did occur, the seasonal mean melt rates were the highest of the entire region. Middle elevations remain continuously snow covered throughout the winter and early spring, are prone to more frequent melt, have an earlier date of maximum SWE, and provide the most sustained period of meltwater fluxes to the soil system. The melt dynamics unique to these middle elevations may be critical to the local forest ecosystem. Furthermore, the elevation range of this snowmelt regime varies inter-annually with seasonal meteorology.

In summary, it has been shown that snow water resources vary significantly in mountainous, forested terrain. This variability varies inter-annually as a result of complex interactions between seasonal meteorology, terrain, and vegetation. Furthermore, this study shows that the dynamic nature of physically based snow models have the potential to simulate this variability in complex, mountainous terrain. The series of studies has identified the utility

and limitations of physically based models to simulate snow depth and SWE in forested and alpine terrain. Notable findings include:

1) Sub-canopy snowmelt rates vary inter-annually and that variability cannot reliably be explained with the same canopy metrics for each year;

2) Sub-canopy direct beam solar irradiance was found to explain nearly 60% of the observed variability in sub-canopy seasonal melt rates for a largely cloud-free melt-season;

3) Conversely, the sky view factor explained the most variability in seasonal melt rates during a very cloudy melt-season;

4) When the metrics sky view factor and direct beam canopy transmissivity were provided to a modified one-dimensional snow model significant improvements in simulated melt rates and the timing of meltwater fluxes were obtained over the nominal model with bulk canopy representation;

5) The distributed snow model most accurately simulates the basin-mean snow depth and SWE in regions in close proximity to precipitation gauges;

6) Results highlight unique seasonal melt patterns in middle elevation forested areas where snow cover is consistent, melt is frequent, but the seasonal mean fluxes are reduced compared to higher elevation melt fluxes.

Several important caveats and limitations include: 1) error values in precipitation and solar radiation significantly impact the capacity of snow models to predict seasonal maximum SWE and melt patterns, respectively; 2) model SWE error increases with distance from the precipitation gauges used to derive the model forcing; 3) while the point-scale model showed improved results when modified to accept time-varying direct beam canopy transmissivity, currently no method exists to estimate this canopy metric over large areas (see Section 5.2); 4) combined, the results of the three studies imply that physically based models may be most limited in their predictive capacity as a result of precipitation uncertainty.

These caveats and limitations highlight the need for future work as discussed in more detail below. Overall, the flexibility and fidelity of the presented methods and models make them valuable tools for quantifying and improving our understanding of hydrometeorological process interactions and their individual impacts on catchment hydrology and snow cover distribution. The Alpine3D model could be used to provide real-time estimates of snow water resources in mountainous areas, provided reliable measurements or estimates of meteorological forcing variables are available.

5.2 Future work

The next steps to improving snow model accuracy in forested and alpine mountainous areas include: 1) developing a spatially-distributed estimate of detailed direct beam canopy transmissity; 2) investigation of the optimal spatial and temporal scales at which to estimate net energy fluxes in forested areas and precipitation / redistribution in alpine areas; 3) evaluating

detailed forest canopy radiative transfer models (both photo- and LiDAR-derived canopy representations) against in-situ observations of sub-canopy direct and diffuse components; 4) further investigation of the canopy radiative transfer models, including uncertainty characterization at spatially-aggregated scales in steep and varied terrain; 5) evaluation of Alpine3D forced by high-resolution gridded regional climate model output over the Kaweah River basin compared to runs forced by interpolated ground-based meteorological observations; 6) force Alpine3D with meteorological data representative of future climate conditions downscaled from a high-resolution regional weather model with boundaries forced with National Centers for Environmental Prediction (NCEP) North American Regional Reanalysis (NARR) IPCC emission scenarios.

One of the primary sources of model error was identified as precipitation forcing uncertainty, particularly at high elevations. Future efforts will evaluate the utility of a Bayesian reconstruction model technique (e.g. Durand et al., 2008a), to characterize precipitation patterns using snow covered area estimates based on visible and NIR satellite measurements. The approach could be used to improve estimates of precipitation patterns in alpine terrain where traditional measurements are not available.

In regard to the forested elevations, an important addition to this work will be made by an ongoing research project to derive detailed canopy metrics including sky view factor (e.g. Essery et al., 2008a) and solar direct beam canopy transmissivity from airborne scanning LiDAR data. The technique will make possible distributed estimates of direct beam canopy transmissivity in the forested Wolverton basin. The results will be compared to estimates from hemispherical photographs and used to evaluate spatial patterns in sub-canopy shortwave irradiance. In an

inverse application, the model could be used to simulate the attenuation of direct sunlight by vegetation, which has been shown to warm canopy elements above the ambient air temperature by as much as 30° C (e.g. Pomeroy et al., 2009). The estimates will be used to improve canopy model representation of sub-canopy sensible heat fluxes, and longwave irradiance. Toward this goal, preliminary tests conducted in the Wolverton basin of voxel aggregation of multiple-return discrete LiDAR data (e.g. Hagstrom et al., 2010) combined with an efficient ray tracing algorithm (e.g. Hagstrom and Messinger, 2011) and look-up table shows promise for distributed applications of the current work.

Potential applications of the distributed land surface model include real-time simulation. The snow model could be used to provide physically based initial conditions to streamflow forecast models. Additionally, the native PREVAH conceptual runoff model could be calibrated on historic streamflow data to provide real-time streamflow estimates for a basin of interest. Such analysis may be of interest to water resource management in regions where mountain snowpack represents a critical component of the water resource infrastructure.

Appendix A. SNOWPACK canopy model description

The SNOWPACK model treats the canopy as a single 'big-leaf' with a temperature T_c (K) and storage of intercepted water I (mm) characterized by three common input parameters: *canopy height*, *LAI'* and *canopy openness*. The canopy temperature is calculated by solving an energy balance equation for the canopy layer, including shortwave and longwave radiation and the

turbulent energy fluxes. Heat storage in the canopy is assumed to be zero, thus the energy needed for phase change between frozen and liquid interception is neglected.

The model uses a two-layer RT model for a single canopy layer adopted from *Taconet et al.* (1986), which takes into account multiple reflections between the canopy layer and the surface layer below (snow or bare soil). Absorption of $R_{S\downarrow}$ and $R_{L\downarrow}$ by the canopy layer is determined by the dimensionless absorption factor σ_f:

$$\sigma_f = 1 - \exp\left(-k_{LAI} LAI'\right) \tag{A1}$$

where k_{LAI} (-) is an extinction parameter that is a function of needle orientation and stand structure, and is typically between 0.4 and 0.8. The reflectance or absorption of incident $R_{S\downarrow}$ and $R_{L\downarrow}$ on the canopy elements is determined by the canopy layer albedo and emissivity, respectively. The canopy emissivity is assumed to be equal to unity, while the canopy albedo is treated as a dynamic function of intercepted rain or snow:

$$\alpha_c = f_{wet}\alpha_{wet} + \left(1 - f_{wet}\right)\alpha_{dry} \tag{A2}$$

where f_{wet} (-) is the fraction of the canopy covered by intercepted water calculated as the ratio of the interception storage and the interception capacity I_{max}:

$$f_{wet} = \left(I / I_{max}\right)^{2/3} \tag{A3}$$

and α_{wet} (-) and α_{dry} (-) are parameters for the albedo of wet and dry canopy, respectively. The albedo for the wet part of the canopy can be set differently for liquid and frozen interception. Typical values for needle leaf canopies are α_{dry}=$\alpha_{wet,rain}$=0.1 and $\alpha_{wet,snow}$=0.3-0.4. The radiation fluxes for the two-layer canopy module are only applied to the fraction of the surface covered by

the canopy as defined by the *canopy openness* parameter and otherwise above-canopy $R_{S\downarrow}$ and $R_{L\downarrow}$ fluxes are permitted to pass to the ground surface unimpeded by the canopy layer. Model improvements have been made to enable a more dynamic treatment of canopy transmissivity than the static representation evaluated in this study. In the most recent model version, the *canopy openness* is assumed to be constant for $R_{L\downarrow}$ and the diffuse fraction of $R_{S\downarrow}$ (as in this study), whereas it is adjusted as a function of solar elevation angle and an assumed canopy geometry defined by the height and diameter of the trees following *Gryning et al.* (2001). The adsorption factor for direct solar radiation can now either be calculated using eq. (3) or optionally modified as a function of solar angle Ω following *Chen et al.* (1997). The combined transmission of direct and diffuse shortwave radiation is then given by:

$$\tau_c = \left(1 - f_{diffuse}\right) \mathrm{e}^{-k_{LAI} LAI' / \sin(\Omega)} + f_{diffuse} \mathrm{e}^{-k_{LAI} LAI'} \qquad \text{(A4)}$$

where $f_{diffuse}$ (-) is the diffuse fraction of above-canopy global shortwave radiation. Future efforts will evaluate this dynamic, bulk treatment of canopy transmissivity against the results of the explicit, photo-derived methods presented here.

The maximum canopy interception rate ΔI (mm hr^{-1}) of above-canopy precipitation P (mm hr^{-1}) is calculated as a function of canopy storage saturation with an equation originally proposed by *Merriam* (1960), in the form given by *Pomeroy et al.* (1998b):

$$\Delta I = c_{\Delta t} \left(I_{max} - I\right) \left(1 - \exp\left\{ - \frac{\left(1 - f_{through}\right) P}{I_{max}} \right\} \right) \qquad \text{(A5)}$$

where $c_{\Delta t}$ is a time-step dependent parameter called the unloading coefficient, with a suggested value of 0.7 for hourly time steps (Pomeroy et al., 1998b), $f_{through}$ is the fraction of direct

throughfall set equal to the *canopy openness* parameter, and I_{max} (mm) is the maximum interception capacity. The latter is calculated as a linear function of *LAI*:

$$I_{max} = i_{LAI} LAI \tag{A6}$$

where the parameter i_{LAI} (mm) is assumed to be a constant for intercepted rain, and a function of the density of intercepted snow $\rho_{s,int}$ (kg m^{-3}) following *Pomeroy et al.* (1998b):

$$i_{LAI} = i_{max} \left(0.27 + 46 / \rho_{s,int} \right) \tag{A7}$$

Schmidt and Gluns (1991) reported estimates of the parameter i_{max} (mm m^{-2}) for spruce (5.9) and pine (6.6). The density of the intercepted snow $\rho_{s,int}$ (kg m^{-3}) is estimated as a function of air temperature (Lehning et al., 2002a). The interception is further assumed to be liquid above and frozen below the air temperature threshold for frozen precipitation (1°C) specified to the SNOWPACK model and used to determine precipitation gauge catch efficiency, described in Section 2.1. Thus, unloading of snow as a consequence of increased air temperature and reduced storage capacity is calculated whenever *I* exceedes I_{max}.

The aerodynamic resistances for sensible and latent heat fluxes are calculated using a two-layer model that assumes logarithmic wind profiles above, within, and below the canopy adopted from (Blyth et al., 1999). The aerodynamic resistances from the canopy level to the reference level of the meteorological forcing data is calculated with the usual bulk formulation based on displacement height and surface roughness lengths of momentum and heat including a Monin-Obukhov stability correction following *Högström* (1996) and *Beljaars and Holtslag* (1991). An additional within-canopy resistance r_{add} (s m^{-1}) is added for the fluxes from the canopy surface and the snow surface to the canopy layer on the general form:

$$r_{add} = \ln\left(z_{0\mathrm{m}} / z_{0\mathrm{h}}\right)\frac{1}{u_* k} f_{LAI} \qquad \text{(A8)}$$

where z_{0m} and z_{0h} are the surface roughness lengths of either the canopy or the snow surface, u_* is the friction velocity estimated above the canopy, and k is the Von Kármán constant (0.4). The final term in (Eq. 9) , f_{LAI}, is an exponential function of LAI:

$$f_{LAI} = 1 + r_{a,LAI}\left(1 - \exp\{-LAI\}\right). \qquad \text{(A9)}$$

where the parameter $r_{a,LAI}$ is the maximum multiplicative increase.

References

Aguado, E., 1985. Radiation Balances of Melting Snow Covers at an Open Site in the Central Sierra Nevada, California. Water Resour. Res., 21(11): 1649-1654.

Allen, R.G., Trezza, R. and Tasumi, M., 2006. Analytical integrated functions for daily solar radiation on slopes. Agricultural and Forest Meteorology, 139(1-2): 55-73.

Anderson, E.A., 1986. The National Weather Service River Forecast System and its applications to cold regions, 6th Int. Northern Basins Symposium-Workshop, Michigan Technological University, Houghton, Michigan, pp. 219-237.

Baldocchi, D.D., Hicks, B.B. and Camara, P., 1987. A Canopy Stomatal Resistance Model for Gaseous Deposition to Vegetated Surfaces. Atmospheric Environment, 21(1): 91-101.

Baldocchi, D.D., Hutchison, B., Matt, D. and McMillen, R., 1986. Seasonal variation in the statistics of photosynthetically active radiation penetration in an oak-hickory forest. Agricultural and Forest Meteorology, 36(4): 343-361.

Baldocchi, D.D., Matt, D.R., Hutchison, B.A. and McMillen, R.T., 1984. Solar radiation within an oak--hickory forest: an evaluation of the extinction coefficients for several radiation components during fully-leafed and leafless periods. Agricultural and Forest Meteorology, 32(3-4): 307-322.

Bales, R.C. et al., 2011. Soil Moisture Response to Snowmelt and Rainfall in a Sierra Nevada Mixed-Conifer Forest. Vadose Zone Journal, 10(3): 786-799.

Barlage, M. et al., 2010. Noah land surface model modifications to improve snowpack prediction in the Colorado Rocky Mountains. J. Geophys. Res., 115(D22): D22101.

Bartelt, P. and Lehning, M., 2002. A physical SNOWPACK model for the Swiss avalanche warning: Part I: numerical model. Cold Regions Science and Technology, 35(3): 123-145.

Bavay, M., Lehning, M., Jonas, T. and Löwe, H., 2009. Simulations of future snow cover and discharge in Alpine headwater catchments. Hydrological Processes, 23(1): 95-108.

Becker, P., Erhart, D.W. and Smith, A.P., 1989. Analysis of forest light environments part I.

Computerized estimation of solar radiation from hemispherical canopy photographs. Agricultural and Forest Meteorology, 44(3-4): 217-232.
Beljaars, A.C.M. and Holtslag, A.A.M., 1991. Flux parameterization over land surfaces for atmospheric models. Journal of Applied Meteorology, 30: 327-341.
Beniston, M., 2003. Climatic Change in Mountain Regions: A Review of Possible Impacts. Climatic Change, 59(1): 5-31.
Blöschl, G., 1999. Scaling issues in snow hydrology. Hydrological Processes, 13(14-15): 2149-2175.
Blyth, E.M., Harding, R.J. and Essery, R., 1999. A coupled dual source GCM SVAT. HAL - CCSD.
Bonan, G.B., 1998. The Land Surface Climatology of the NCAR Land Surface Model Coupled to the NCAR Community Climate Model*. Journal of Climate, 11(6): 1307-1326.
Bréda, N.J.J., 2003. Ground-based measurements of leaf area index: a review of methods, instruments and current controversies. Journal of Experimental Botany, 54(392): 2403-2417.
Brun, E., David, P., Sudul, M. and Brunot, G., 1992. A numerical model to simulate snow cover stratigraphy for operational avalanche forecasting. Journal of Glaciology, 38: 13-22.
CDF, 2009. State of California, Department of Finance, California County Population Estimates and Components of Change by Year, July 1, 2000-2009, Sacramento, California.
CDFA, 2009. California Agriculture Statistical Review. In: C.D.o.F.a. Agriculture (Editor), California Agricultural Resource Directory, pp. 17-31.
Chen, J.M., Blanken, P.D., Black, T.A., Guilbeault, M. and Chen, S., 1997. Radiation regime and canopy architecture in a boreal aspen forest. Agricultural and Forest Meteorology, 86(1–2): 107-125.
Claussen, M., 1991. Estimation of areally-averaged surface fluxes. Boundary-Layer Meteorology, 54(4): 387-410.
Côté, J.-F., Widlowski, J.-L., Fournier, R.A. and Verstraete, M.M., 2009. The structural and radiative consistency of three-dimensional tree reconstructions from terrestrial lidar. Remote Sensing of Environment, 113(5): 1067-1081.
Daly, C., Neilson, R.P. and Phillips, D.L., 1994. A statistical-topographic model for mapping climatological precipitation over mountainous terrain. Journal of Applied Meteorology, 33(2): 140-158.
Danson, F.M., Hetherington, D., Morsdorf, F., Koetz, B. and Allgower, B., 2007. Forest Canopy Gap Fraction From Terrestrial Laser Scanning. Geoscience and Remote Sensing Letters, IEEE, 4(1): 157-160.
Davis, R.E. et al., 1997. Variation of snow cover ablation in the boreal forest: A sensitivity study on the effects of conifer canopy. J. Geophys. Res., 102(D24): 29389-29395.
Dickinson, R.E., 1983. Land Surface Processes and Climate—Surface Albedos and Energy Balance. In: S. Barry (Editor), Advances in Geophysics. Elsevier, pp. 305-353.
Durand, M., Molotch, N.P. and Margulis, S.A., 2008a. A Bayesian approach to snow water equivalent reconstruction. J. Geophys. Res., 113(D20): D20117.
Durand, M., Molotch, N.P. and Margulis, S.A., 2008b. Merging complementary remote sensing datasets in the context of snow water equivalent reconstruction. Remote Sensing of Environment, 112(3): 1212-1225.

Elliot, R.D. and Shaffer, R.W., 1962. The development of quantitative relationships between orographic precipitation and air-mass parameters for use in forecasting and cloud seeding evaluation. Journal of Applied Meteorology, 1: 218-228.
Ellis, C.R. and Pomeroy, J.W., 2007. Estimating sub-canopy shortwave irradiance to melting snow on forested slopes. Hydrological Processes, 21(19): 2581-2593.
Ellis, C.R., Pomeroy, J.W., Brown, T. and MacDonald, J., 2010. Simulation of snow accumulation and melt in needleleaf forest environments. Hydrol. Earth Syst. Sci., 14: 925-940.
Essery, R., 1998. Snow modelling in the Hadley Centre GCM. Physics and Chemistry of The Earth, 23(5,Äì6): 655-659.
Essery, R. et al., 2008a. Radiative transfer modeling of a coniferous canopy characterized by airborne remote sensing. Journal of Hydrometeorology, 9: 228-241.
Essery, R. and Etchevers, P., 2004. Parameter sensitivity in simulations of snowmelt. J. Geophys. Res., 109(D20): D20111.
Essery, R., Pomeroy, J., Ellis, C. and Link, T., 2008b. Modelling longwave radiation to snow beneath forest canopies using hemispherical photography or linear regression. Hydrological Processes, 22(15): 2788-2800.
Essery, R. et al., 2009. An Evaluation of Forest Snow Process Simulations. Bulletin of the American Meteorological Society, 90(8): 1120-+.
Essery, R.L., Pomeroy, J.W., Parvianen, J. and Storck, P., 2003. Sublimation of snow from coniferous forests in a climate model. J. Climate, 16: 1855–1864.
Faria, D.A., Pomeroy, J.W. and Essery, R.L.H., 2000. Effect of covariance between ablation and snow water equivalent on depletion of snow-covered area in a forest. Hydrological Processes, 14(15): 2683-2695.
Frazer, G.W., Canham, C.D. and Lertzman, K.P., 1999. Gap Light Analyser (GLA). Version 2.0: Imaging Software to Extract Canopy Structure and Gap Light Transmission Indices From True-Colour Fisheye Photographs. Users Manual and Program Documentation. Simon Fraser University, Burnaby, B.C. and the Institute of Ecosystem Studies, Millbrook , New York .
Frazer, G.W., Trofymow, J.A. and Lertzman, K.P., 2000. Canopy openness and leaf area in chronosequences of coastal temperate rainforests. Can. J. For. Res., 30(2): 239-256.
Golding, D.L. and Swanson, R.H., 1978. Snow accumulation and melt in small forest openings in Alberta. Canadian Journal of Forest Research, 8(4): 380-388.
Golding, D.L. and Swanson, R.H., 1986. Snow distribution patterns in clearings and adjacent forest. Water Resour. Res., 22(13): 1931-1940.
Groisman, P.Y. and Easterling, D.R., 1994. Variability and trends of total precipitation and snowfall over the United States and Canada. Journal Name: Journal of Climate; (United States); Journal Volume: 7:1: Medium: X; Size: Pages: 184-205.
Groot Zwaaftink, C.D., Lˆwe, H., Mott, R., Bavay, M. and Lehning, M., 2011. Drifting snow sublimation: A high-resolution 3-D model with temperature and moisture feedbacks. J. Geophys. Res., 116(D16): D16107.
Gryning, S.E., Batchvarova, E. and DeBruin, H.A.R., 2001. Energy balance of a sparse coniferous high-latitude forest under winter conditions. Boundary-Layer Meteorology, 99: 465-488.

Hagstrom, S. and Messinger, D., 2011. Line-of-sight analysis using voxelized discrete lidar. In: M.D. Turner and G.W. Kamerman (Editors). SPIE, Orlando, Florida, USA, pp. 80370B-11.
Hagstrom, S., Messinger, D. and Brown, S., 2010. Feature extraction using voxel aggregation of focused discrete lidar data. In: M.D. Turner and G.W. Kamerman (Editors). SPIE, Orlando, Florida, USA, pp. 76840X-11.
Hall, D.K., Foster, J.L., Verbyla, D.L., Klein, A.G. and Benson, C.S., 1998. Assessment of Snow-Cover Mapping Accuracy in a Variety of Vegetation-Cover Densities in Central Alaska. Remote Sensing of Environment, 66(2): 129-137.
Hamlet, A.F., Mote, P.W., Clark, M.P. and Lettenmaier, D., 2005. Effects of Temperature and Precipitation Variability on Snowpack Trends in the Western United States. Journal of Climate, 18(21): 4545-4561.
Hardy, J.P. et al., 2004. Solar radiation transmission through conifer canopies. Agricultural and Forest Meteorology, 126(3-4): 257-270.
Hedstrom, N.R. and Pomeroy, J.W., 1998. Measurements and modelling of snow interception in the boreal forest. Hydrological Processes, 12(10-11): 1611-1625.
Helbig, N., L√∂we, H. and Lehning, M., 2009. Radiosity Approach for the Shortwave Surface Radiation Balance in Complex Terrain. Journal of the Atmospheric Sciences, 66(9): 2900-2912.
Hock, R., 2003. Temperature index melt modeling in mountain areas. Journal of Hydrology, 282: 104-115.
Högström, U., 1996. Review of some basic characteristics of the atmospheric surface layer. Boundary-Layer Meteorology, 78: 215-246.
Homer, C., Huang, C., Yang, C., Wylie, B. and Coan, M., 2004. Development of a 2001 National Landcover Database for the United States. Photogrammetric Engineering and Remote Sensing, 70: 829-840.
Hopkinson, C. and Chasmer, L., 2009. Testing LiDAR models of fractional cover across multiple forest ecozones. Remote Sensing of Environment, 113(1): 275-288.
Huss, M., Farinotti, D., Bauder, A. and Funk, M., 2008. Modelling runoff from highly glacierized alpine drainage basins in a changing climate. Hydrological Processes, 22(19): 3888-3902.
Jordan, R., 1991. A one-dimensional temperature model for a snow cover: Technical documentation for SNTHERM.89, USA Cold Regions Research and Engineering Laboratory, Hanover, New Hampshire.
Jost, G., Dan Moore, R., Weiler, M., Gluns, D.R. and Alila, Y., 2009. Use of distributed snow measurements to test and improve a snowmelt model for predicting the effect of forest clear-cutting. Journal of Hydrology, 376(1-2): 94-106.
Jost, G., Weiler, M., Gluns, D.R. and Alila, Y., 2007. The influence of forest and topography on snow accumulation and melt at the watershed-scale. Journal of Hydrology, 347(1-2): 101-115.
Klein, A.G., Hall, D.K. and Riggs, G.A., 1998. Improving snow cover mapping in forests through the use of a canopy reflectance model. Hydrological Processes, 12(10-11): 1723-1744.
Kobayashi, H. and Iwabuchi, H., 2008. A coupled 1-D atmosphere and 3-D canopy radiative

transfer model for canopy reflectance, light environment, and photosynthesis simulation in a heterogeneous landscape. Remote Sensing of Environment, 112(1): 173-185.
Kobierska, F. et al., 2011. Climate change effects on snow melt and discharge of a partly glacierized watershed in Central Switzerland (SoilTrec Critical Zone Observatory). Applied Geochemistry, 26, Supplement(0): S60-S62.
Koivusalo, H. and Kokkonen, T., 2002. Snow processes in a forest clearing and in a coniferous forest. Journal of Hydrology, 262(1-4): 145-164.
Kurz, W.A. et al., 2008. Mountain pine beetle and forest carbon feedback to climate change. Nature, 452(7190): 987-990.
Kuye, A. and Jagtap, S.S., 1992. Analysis of solar radiation data for Port Harcourt, Nigeria. Solar Energy, 49(2): 139-145.
LADWP, 2012. Water, Los Angeles Aqueduct. In: L.A.D.o.W.a. Power.
Larsen, D.R. and Kershaw, J.A., 1996. Influence of canopy structure assumptions on predictions from Beer's law. A comparison of deterministic and stochastic simulations. Agricultural and Forest Meteorology, 81(1-2): 61-77.
Lehning, M., Bartelt, P. and Brown, B., 1998. Operational use of a snowpack model for the avalanche warning service in Switzerland: model development and first experiences, NGI Anniversary Conference, Norwegian Geotechnical Institute, pp. 169-174.
Lehning, M., Bartelt, P., Brown, B. and Fierz, C., 2002a. A physical SNOWPACK model for the Swiss avalanche warning: Part III: meteorological forcing, thin layer formation and evaluation. Cold Regions Science and Technology, 35(3): 169-184.
Lehning, M., Bartelt, P., Brown, B., Fierz, C. and Satyawali, P., 2002b. A physical SNOWPACK model for the Swiss avalanche warning: Part II. Snow microstructure. Cold Regions Science and Technology, 35(3): 147-167.
Lehning, M. et al., 1999. SNOWPACK model calculations for avalanche warning based upon a new network of weather and snow stations. Cold Regions Science and Technology, 30(1-3): 145-157.
Lehning, M. et al., 2006. ALPINE3D: a detailed model of mountain surface processes and its application to snow hydrology. Hydrological Processes, 20(10): 2111-2128.
Li, X., Strahler, A.H. and Woodcock, C.E., 1995. A hybrid geometric optical-radiative transfer approach for modeling albedo and directional reflectance of discontinuous canopies. Geoscience and Remote Sensing, IEEE Transactions on, 33(2): 466-480.
Link, T.E. and Marks, D., 1999. Point simulation of seasonal snow cover dynamics beneath boreal forest canopies. J. Geophys. Res., 104(D22): 27841-27857.
Liston, G.E., 1995. Local Advection of Momentum, Heat, and Moisture during the Melt of Patchy Snow Covers. Journal of Applied Meteorology, 34(7): 1705-1715.
Liston, G.E. and Elder, K., 2006a. A Distributed Snow-Evolution Modeling System (SnowModel). Journal of Hydrometeorology, 7(6): 1259-1276.
Liston, G.E. and Elder, K., 2006b. A Meteorological Distribution System for High-Resolution Terrestrial Modeling (MicroMet). Journal of Hydrometeorology, 7(2): 217-234.
Liu, J., Melloh, R.A., Woodcock, C.E., Davis, R.E. and Ochs, E.S., 2004. The effect of viewing geometry and topography on viewable gap fractions through forest canopies. Hydrological Processes, 18(18): 3595-3607.
Liu, Y.H. and Jordan, R.C., 1960. The Interrelationship and Characteristic Distribution of Direct,

Diffuse and Total Solar Radiation. Solar Energy, 4: 3.
Livneh, B., Xia, Y., Mitchell, K.E., Ek, M.B. and Lettenmaier, D.P., 2010. Noah LSM Snow Model Diagnostics and Enhancements. Journal of Hydrometeorology, 11(3): 721-738.
López-Moreno, J.I. and Latron, J., 2008. Influence of canopy density on snow distribution in a temperate mountain range. Hydrological Processes, 22(1): 117-126.
López-Moreno, J.I. and Stähli, M., 2008. Statistical analysis of the snow cover variability in a subalpine watershed: Assessing the role of topography and forest interactions. Journal of Hydrology, 348(3-4): 379-394.
Luce, C.H., Tarboton, D.G. and Cooley, K.R., 1999. Sub-grid parameterization of snow distribution for an energy and mass balance snow cover model. Hydrological Processes, 13(12-13): 1921-1933.
Lundberg, A., Calder, I. and Harding, R., 1998. Evaporation of intercepted snow: measurement and modelling. Journal of Hydrology, 206(3-4): 151-163.
Magnusson, J., Farinotti, D., Jonas, T. and Bavay, M., 2011. Quantitative evaluation of different hydrological modelling approaches in a partly glacierized Swiss watershed. Hydrological Processes, 25(13): 2071-2084.
Marks, D., Dozier, J. and Davis, R.E., 1992. Climate and energy exchange at the snow surface in the Alpine Region of the Sierra Nevada: 1. Meteorological measurements and monitoring. Water Resour. Res., 28(11): 3029-3042.
Marks, D., Flerchinger, G.N. and Seyfried, M.S., 2003. Influence of sub-grid variability on snow deposition and ablation in North American Mountain Environments: Implications for Upscaling to Meso-scale Representations, First Interagency Conference on Research in the Watersheds (USDA), pp. 437-443.
Marks, D., Link, T., Winstral, A. and Garen, D., 2001. Simulating snowmelt processes during rain-on-snow over a semi-arid mountain basin. Annals of Glaciology, 32: 195-202.
Mätzler, C. and Wiesmann, A., 1999. Extension of the Microwave Emission Model of Layered Snowpacks to Coarse-Grained Snow. Remote Sensing of Environment, 70(3): 317-325.
Meiman, J.R., 1968. Snow Accumulation Related to Elevation, Aspect and Forest Canopy, Canadian National Committee for I.H.D., pp. 35-47.
Meng, X., Currit, N. and Zhao, K., 2010. Ground Filtering Algorithms for Airborne LiDAR Data: A Review of Critical Issues. Remote Sensing, 2(3): 833-860.
Meromy, L., Molotch, N.P., Link, T.E., Fassnacht, S.R. and Rice, R., 2012. Subgrid variability of snow water equivalent at operational snow stations in the western USA. Hydrological Processes: n/a-n/a.
Merriam, M., 1960. A note on the interception loss equation. Journal of Geophysical Research, 65: 3850-3851.
Michlmayr, G. et al., 2008. Application of the Alpine 3D model for glacier mass balance and glacier runoff studies at Goldbergkees, Austria. Hydrological Processes, 22(19): 3941-3949.
Minder, J.R., 2010. The Sensitivity of Mountain Snowpack Accumulation to Climate Warming. Journal of Climate, 23(10): 2634-2650.
Molotch, N.P., 2009. Reconstructing snow water equivalent in the Rio Grande headwaters using remotely sensed snow cover data and a spatially distributed snowmelt model. Hydrological Processes, 23(7): 1076-1089.

Molotch, N.P., Blanken, P.D. and Link, T.E., 2011. Snow: Hydrological and Ecological Feedbacks in Forests. In: D.F. Levia, D. Carlyle-Moses and T. Tanaka (Editors), Forest Hydrology and Biogeochemistry. Ecological Studies. Springer Netherlands, pp. 541-555.
Molotch, N.P. et al., 2009. Ecohydrological controls on snowmelt partitioning in mixed-conifer sub-alpine forests. Ecohydrology, 2(2): 129-142.
Molotch, N.P. and Margulis, S.A., 2008. Estimating the distribution of snow water equivalent using remotely sensed snow cover data and a spatially distributed snowmelt model: A multi-resolution, multi-sensor comparison. Advances in Water Resources, 31(11): 1503-1514.
Monsi, M. and Saeki, T., 1953. Über den Lichtfaktor in den Pflanzengesellschaften und seine Bedeutung für die Stoffproduktion. Japanese Journal of Botany, 14: 22-52.
Mote, P.W., 2006. Climate-Driven Variability and Trends in Mountain Snowpack in Western North America*. Journal of Climate, 19(23): 6209-6220.
Mott, R. et al., 2008. Simulation of seasonal snow cover distribution for glacierized sites (Sonnblick, Austria) with the Alpine3D model. Annals of Glaciology, 49(1): 155-160.
Mott, R. and Lehning, M., 2010. Meteorological Modeling of Very High-Resolution Wind Fields and Snow Deposition for Mountains. Journal of Hydrometeorology, 11(4): 934-949.
Musselman, K.N., Molotch, N.P. and Brooks, P.D., 2008. Effects of vegetation on snow accumulation and ablation in a mid-latitude sub-alpine forest. Hydrological Processes, 22(15): 2767-2776.
Musselman, K.N., Molotch, N.P., Margulis, S.A., Kirchner, P. and Bales, R.C., 2012. Influence of canopy structure and direct beam solar irradiance on snowmelt rates in a mixed conifer forest. Agricultural and Forest Meteorology, 161C: 46-56.
Ni, W., Li, X., Woodcock, C.E., Roujean, J.-L. and Davis, R.E., 1997. Transmission of solar radiation in boreal conifer forests: Measurements and models. J. Geophys. Res., 102(D24): 29555-29566.
Nijssen, B. and Lettenmaier, D.P., 1999. A simplified approach for predicting shortwave radiation transfer through boreal forest canopies. J. Geophys. Res., 104(D22): 27859-27868.
Niu, G.-Y. et al., 2011. The community Noah land surface model with multiparameterization options (Noah-MP): 1. Model description and evaluation with local-scale measurements. J. Geophys. Res., 116(D12): D12109.
NOAA, 1985. National Oceanic and Atmospheric Administration, Narrative Summaries, Tables and Maps for Each State with Overview of State Climatologist Programs. Gale Research Company.
Norman, J.M. and Campbell, G.S., 1989. Plant Physiological Ecology Field Methods and Instrumentation. In: P.e. al. (Editor), Canopy structure. Chapman and Hall, London, pp. 301-325.
Norman, J.M. and Jarvis, P.G., 1974. Photosynthesis in Sitka spruce (Picea sitchensis (Bong.) Carr.). III. Measurements of canopy structure and interception of radiation. Journal of Applied Ecology, 11: 375-398.
NPS, 2012. Sequoia and Kings Canyon National Park, Weather and Climate.
NRCS, 2012a. SNOTEL Data Collection Network Fact Sheet. In: N.R.C. Service (Editor). United States Department of Agriculture

NRCS, 2012b. Snow surveys and water supply forecasting. In: N.R.C. Service (Editor), Agriculture Information Bulletin 536. United States Department of Agriculture
Ohmura, A., 2001. Physical basis for the temperature-based melt-index method. Journal of Applied Meteorology, 40: 753-761.
Oke, T.R., 1988. Boundary Layer Climates. Routledge (formerly Methuen), New York, NY (USA).
Okogbue, E.C., Adedokun, J.A. and Holmgren, B., 2009. Hourly and daily clearness index and diffuse fraction at a tropical station, Ile-Ife, Nigeria. International Journal of Climatology, 29(8): 1035-1047.
Ovington, J.D. and Madgwick, H.A.I., 1955. A Comparison of Light in Difference Woodlands. Forestry, 28(2): 141-146.
Pearcy, R.W., 1990. SUNFLECKS AND PHOTOSYNTHESIS IN PLANT CANOPIES. Annual Review of Plant Physiology and Plant Molecular Biology, 41: 421-453.
Pierce, D.W. et al., 2008. Attribution of Declining Western U.S. Snowpack to Human Effects. Journal of Climate, 21(23): 6425-6444.
Pomeroy, J., Fang, X. and Ellis, C., 2012. Sensitivity of snowmelt hydrology in Marmot Creek, Alberta to forest cover disturbance. Hydrological Processes: n/a-n/a.
Pomeroy, J.W. and Dion, K., 1996. Winter radiation extinction and reflection in a boreal pine canopy: Measurements and modelling. Hydrological Processes, 10(12): 1591-1608.
Pomeroy, J.W. et al., 2007. The cold regions hydrological model: a platform for basing process representation and model structure on physical evidence. Hydrological Processes, 21(19): 2650-2667.
Pomeroy, J.W., Gray, D.M., Hedstrom, N.R. and Janowicz, J.R., 2002. Prediction of seasonal snow accumulation in cold climate forests. Hydrological Processes, 16(18): 3543-3558.
Pomeroy, J.W. et al., 1998a. An evaluation of snow accumulation and ablation processes for land surface modelling. Hydrological Processes, 12(15): 2339-2367.
Pomeroy, J.W., Hanson, S. and Faria, D., 2001. Small-scale variation in snowmelt energy in a boreal forest: an additional factor controlling depletion of snow cover?, 58th Eastern Snow Conference, Ottawa, Ontario, Canada.
Pomeroy, J.W. et al., 2009. The impact of coniferous forest temperature on incoming longwave radiation to melting snow. Hydrological Processes, 23(17): 2513-2525.
Pomeroy, J.W., Parviainen, J., Hedstrom, N. and Gray, D.M., 1998b. Coupled modelling of forest snow interception and sublimation. Hydrological Processes, 12(15): 2317-2337.
Price, A.G. and Dunne, T., 1976. Energy balance computations of snowmelt in a subarctic area. Water Resour. Res., 12(4): 686-694.
Reda, I. and Andreas, A., 2004. Solar position algorithm for solar radiation applications. Solar Energy, 76(5): 577-589.
Reifsnyder, W.E., Furnival, G.M. and Horowitz, J.L., 1971. Spatial and temporal distribution of solar radiation beneath forest canopies. Agricultural Meteorology, 9(0): 21-37.
Rutter, N. et al., 2009. Evaluation of forest snow processes models (SnowMIP2). Journal of Geophysical Research-Atmospheres, 114: -.
Satterlund, D.R., 1979. An improved equation for estimating long-wave radiation from the atmosphere. Water Resour. Res., 15(6): 1649-1650.
Schleppi, P., 2011. Forested Water Catchments in a Changing Environment. In: M. Bredemeier

et al. (Editors), Forest Management and the Water Cycle. Ecological Studies. Springer Netherlands, pp. 89-110.
Schleppi, P., Conedera, M., Sedivy, I. and Thimonier, A., 2007. Correcting non-linearity and slope effects in the estimation of the leaf area index of forests from hemispherical photographs. Agricultural and Forest Meteorology, 144(3-4): 236-242.
Schlosser, C.A., Robock, A., Vinnikov, K.Y., Speranskaya, N.A. and Xue, Y., 1997. 18-Year Land-Surface Hydrology Model Simulations for a Midlatitude Grassland Catchment in Valdai, Russia. Monthly Weather Review, 125(12): 3279-3296.
Schmidt, R.A., 1982. Properties of blowing snow. Rev. Geophys., 20(1): 39-44.
Schmidt, R.A. and Gluns, D.R., 1991. Snowfall interception on branches of three conifer species. Canadian Journal of Forest Research, 21(8): 1262-1269.
Schmugge, T.J., Kustas, W.P., Ritchie, J.C., Jackson, T.J. and Rango, A., 2002. Remote sensing in hydrology. Advances in Water Resources, 25(8,Äì12): 1367-1385.
Seyfried, M.S. and Wilcox, B.P., 1995. Scale and the Nature of Spatial Variability: Field Examples Having Implications for Hydrologic Modeling. Water Resour. Res., 31(1): 173-184.
Shamir, M.S. and Georgakakos, K.P., 2005. Distributed snow accumulation and ablation modeling in the American River basin. Advances in Water Resources, 29: 558-570.
Shugart, H.H., 1984. A theory of forest dynamics. Springer-Verlag, New York.
Sicart, J.E. et al., 2004. A Sensitivity Study of Daytime Net Radiation during Snowmelt to Forest Canopy and Atmospheric Conditions. Journal of Hydrometeorology, 5(5): 774-784.
Spanner, M.A., Pierce, L.L., Peterson, D.L. and Running, S.W., 1990. Remote sensing of temperate coniferous forest leaf area index. The influence of canopy closure, understory vegetation and background reflectance. International Journal of Remote Sensing, 11(1): 95-111.
Stähli, M., Jonas, T. and Gustafsson, D., 2009. The role of snow interception in winter-time radiation processes of a coniferous sub-alpine forest. Hydrological Processes, 23(17): 2498-2512.
Stephenson, N., 1988. Climate and water balance in Sequoia National Park, California. Sequoia National Park Headquarters, Three Rivers, CA.
Storck, P., Lettenmaier, D.P. and Bolton, S.M., 2002. Measurement of snow interception and canopy effects on snow accumulation and melt in a mountainous maritime climate, Oregon, United States. Water Resour. Res., 38(11): 1223.
Sun, S. and Xue, Y., 2001. Implementing a new snow scheme in Simplified Simple Biosphere Model. Advances in Atmospheric Sciences, 18(3): 335-354.
Taconet, O., Bernard, R. and Vidal-Madjar, D., 1986. Evapotranspiration over an agricultural region using a surface flux/temperature model based on NOAA-AVHRR data. American Meteorological Society, 25(3): 284-307.
Tague, C., Seaby, L. and Hope, A., 2009. Modeling the eco-hydrologic response of a Mediterranean type ecosystem to the combined impacts of projected climate change and altered fire frequencies. Climatic Change, 93(1): 137-155.
Talbot, J. et al., 2006. Relating snow dynamics and balsam fir stand characteristics, Montmorency Forest, Quebec. Hydrological Processes, 20(5): 1187-1199.
Tarboton, D.G., Blöschl, G., Cooley, K.R., Kirnbauer, R. and Luce, C., 2000. Spatial snow cover

processes at Kühtai and Reynolds Creek. In: R.G.a.G. Blöschl (Editor), Spatial Patterns in Catchment Hydrology: Observations and Modelling. Cambridge Univ. Press, New York, pp. 158-186.
Thornton, P.E., Running, S.W. and White, M.A., 1997. Generating surfaces of daily meteorological variables over large regions of complex terrain. Journal of Hydrology, 190(3-4): 214-251.
Tonnessen, K.A., 1991. The Emerald Lake watershed study: introduction and site description. Water Resour. Res., 27(7): 1537-1539.
Tribbeck, M.J., Gurney, R.J., Morris, E.M. and Pearson, D.W.C., 2004. A new Snow-SVAT to simulate the accumulation and ablation of seasonal snow cover beneath a forest canopy. Journal of Glaciology, 50(169): 171-182.
Trujillo, E., Ramirez, J.A. and Elder, K., 2007. Topographic, meteorologic, and canopy controls on the scaling characteristics of the spatial distribution of snow depth fields. Water Resour. Res., 43.
USGS, 2012. Feature Detail Report for Lake Kaweah, Geographic Names Information System.
van Leeuwen, M. and Nieuwenhuis, M., 2010. Retrieval of forest structural parameters using LiDAR remote sensing. European Journal of Forest Research, 129(4): 749-770.
Varhola, A. et al., 2010a. The influence of ground- and lidar-derived forest structure metrics on snow accumulation and ablation in disturbed forests. Canadian Journal of Forest Research, 40: 812-821.
Varhola, A., Coops, N.C., Weiler, M. and Moore, R.D., 2010b. Forest canopy effects on snow accumulation and ablation: An integrative review of empirical results. Journal of Hydrology, 392(3-4): 219-233.
Veatch, W., Brooks, P.D., Gustafson, J.R. and Molotch, N.P., 2009. Quantifying the effects of forest canopy cover on net snow accumulation at a continental, mid-latitude site. Ecohydrology, 2(2): 115-128.
Vivoni, E.R. et al., 2008. Vegetation controls on soil moisture distribution in the Valles Caldera, New Mexico, during the North American monsoon. Ecohydrology, 1(3): 225-238.
Walter, T.M. et al., 2005. Process-based snowmelt modeling: does it require more input data than temperature-index modeling? Journal of Hydrology, 300(1,Äì4): 65-75.
Wiesmann, A. and Mätzler, C., 1999. Microwave Emission Model of Layered Snowpacks. Remote Sensing of Environment, 70(3): 307-316.
Wigmosta, M.S., Vail, L.W. and Lettenmaier, D.P., 1994. A distributed hydrology-vegetation model for complex terrain. Water Resour. Res., 30(6): 1665.
Yang, R., Friedl, M.A. and Ni, W., 2001. Parameterization of shortwave radiation fluxes for nonuniform vegetation canopies in land surface models. J. Geophys. Res., 106(D13): 14275-14286.